Aerodynamic Drag of a Two-Dimensional External Compression Inlet at Supersonic Speed

J C Esterhuyse

DECLARATION

The contents of this dissertation represent my own work and the opinions contained herein are my own and not necessarily those of the Technikon.

Signature : _____ Date : 3 March 1997

A thesis submitted in fulfilment of the requirements for the DOCTORES TECHNOLOGIAE (Engineering Mechanical) in the School of Mechanical and Process Engineering at the Cape Technikon.

Cape Town, South Africa March 1997

ACKNOWLEDGEMENTS

I would like to express my sincere gratitude to the following :

- My supervisors, Drs Rob Hurlin and Les Rencontre for their advice and guidance
- Mr Frans Joubert for his support and motivation
- Gavin Ratner for his invaluable assistance during wind-tunnel testing and designing of test equipment
- Mauro Morelli for believing in the project and making wind-tunnel testing possible
- Aneen Koch for typing and editing the manuscript
- The Cape Technikon for giving me time off to complete this project
- My parents for their keen interest
- My wife, Barbara, for her encouragement and moral support.

I would also like to thank the Council for Scientific and Industrial Research for the use of their facilities as well as the Foundation for Research Development for their financial support.

I am grateful to the Lord, without Whom, nothing could have been accomplished.

SYNOPSIS

This study forms the basis from which the aerodynamic drag of a practical supersonic inlet can be predicted. In air-breathing propulsion systems, as used in high performance flight vehicles, the fuel is carried onboard and the oxygen required for combustion is ingested from the ambient atmosphere. The main function of the inlet is to compress the air from supersonic to subsonic conditions with as little flow distortion as possible.

When the velocity of the vehicle approaches or exceeds sonic velocity (M = 1,0) a number of considerations apply to the induction system. The reason for this is that the velocity of the ingested air has to be reduced to appreciably less than sonic velocity, typically to M = 0,3. Failure to do so will cause the propulsion system to be inoperative and cause damage.

In the process of compressing the air from supersonic to subsonic conditions a drag penalty is paid. The drag characteristics are a function of the external geometry and internal flow control system of the inlet. The problem which was investigated dealt with drag of a specific type of inlet, namely a two-dimensional external compression inlet.

This study is directed at formulating definitive relationships which can be used to design functional inlet systems. To this effect the project was carried out over three phases, a theoretical investigation where a fluid-flow analysis was done of the factors influencing drag. The second phase covered a comprehensive experimental study where intensive wind-tunnel tests were conducted for flight Mach numbers of M = 1,8; M = 2,0; M = 2,2; M = 2,3 and M = 2,4. During the third phase a comparison, between the theoretical values and experimental data was done, for validating the predicted aerodynamic drag figures. The following findings are worth recording:

- the increase in total drag below the full flow conditions is more severe than predicted due to the contribution of spillage drag;
- the range for subcritical mode of operation is smaller than expected due to boundary layer effects.

The study has shown that reasonably good correlation could be achieved between the theoretical analysis and empirical test at low subcritical modes of operation. This suggests that the study has achieved its primary objective.

TABLE OF CONTENTS

LIST OF TABLES

LIST OF FIGURES

NOMENCLATURE

$_a$	Denotes conditions for supersonic spillage at maximum flow
a	Speed of sound
A	Cross-sectional area
$A_{B\infty}$	Free streamtube area captured by the bleed duct
A_c	Capture area
A_{en}	Bleed entry area normal to the flow
A_{ex}	Bleed duct exit area
A_m	Cross-sectional area at maximum section of cowl
A_1	Area enclosed by the maximum-flow streamtube at its intersection with the second oblique shock
A_∞	Streamtube area
A_∞	New or actual streamtube area
C_d	Drag coefficient
C_{ddiv}	Drag coefficient for diverter
C_{dinl}	Drag coefficient for inlet, excluding diverter drag component
C_{dt}	Total drag coefficient for inlet and diverter
C_f	Skin friction coefficient
Cd_1	Drag coefficient for element $d\ell_1$
Cd_2	Drag coefficient for element $d\ell_2$
dh_1	Height of first element perpendicular to free stream flow
dh_2	Height of second element perpendicular to free stream flow
d_m	Maximum model diameter
D	Dimension based on diameter
D_{div}	Diverter drag, including wave pressure and friction drag
D_f	Friction drag
D_{int}	Internal drag caused by bleeding off boundary layer air
D_{lip}	Cowl drag, including wave pressure and friction drag
D_p	Wave pressure drag on cowl section
D_{pre}	Pre-entry drag

D_{spill}	Spillage drag
D_t	Total drag force
D_1	Cowl drag on element $d\ell_1$
D_2	Cowl drag on element $d\ell_2$
ex	Denotes conditions at bleed duct exit
F_A	Axial force
F_d	External drag forces
F_n	Nett thrust due to momentum change between free stream conditions and engine exit
F_p	Nett propulsive thrust
F_T	Stream thrust
h	Diverter height
h_c	Height of inlet opening
h_m	Height of lip at maximum section
h_1	Height of first lip section perpendicular to free stream flow
h_∞	Height of captured streamtube
L_N and ℓ_n	Horizontal dimensions
m_B	Bleed mass flow rate
m_R	Air mass flow ratio
$\dot{m}_c$	Actual mass flow or mass flow entering inlet
$\dot{m}_\infty$	Maximum possible mass flow or mass flow at free stream conditions
$\dot{m}$	Mass flow
$\dot{m}_{spill}$	Spill mass flow
M	Mach number
M'	Normal velocity component
M_{des}	Design Mach number
n	Velocity profile parameter
P	Static pressure

P_{atm}	Atmospheric pressure
P_{bc}	Bleed chamber static pressure
P_{OB}	Stagnation pressure at exit plane inside the bleed chamber
P_{of}	Stagnation pressure at engine face
$P_{o\infty}$	Stagnation pressure in free steam
P_R	Total or Stagnation pressure recovery
P_s	Static pressure in tunnel test section
P_0	Stagnation pressure
P_1	Static pressure behind first oblique shock
P_2	Static pressure behind second oblique shock
P_3	Static pressure behind normal shock
P_i	Static pressure behind first oblique shock of lip
P_{ii}	Static pressure behind expansion wave of lip
P_∞	Free stream static pressure
q	Dynamic pressure
R	Gas constant
Re	Reynolds number
R_t	Reynolds number based on a body length dimension
S	Distance of diverter leading edge behind ramp leading edge
S_f	Projected frontal area
SD	Standard deviation
S_{wet}	Wetted area
T	Static temperature
T_{amb}	Ambient temperature
T_o	Stagnation temperature
U	Streamwise velocity in boundary layer at a distance *y* from the surface
U_t	Streamwise velocity at the edge of the boundary layer
V	Air velocity
V_c	Control volume
w	Width of inlet opening or lip section
Z	Percentage data points which fall within two standard deviations on either side of mean value

β	Yaw angle
δ	Wedge angle or flow deflection angle
δ^1	Boundary layer thickness
δ_w	Wedge angle
δ_s	Sweep back angle of ramp leading edge
ϵ	Shock wave angle
ϵ_D	Shock wave angle between lip and horizontal plane of wedge at design point
η_o	External angle of cowl lip at first section
η_I	External angle of cowl lip at second section
ρ	Air density
Φ/Φ_t	Boundary layer momentum ratio
ν	Prandtl - Meyer angle
$\propto$	Pitch angle or angle of attack
∞	Denotes free stream conditions
γ	Specific heat ratio
*	Denotes critical flow properties where the flow is sonic, M = 1,0

CHAPTER 1

INTRODUCTION

Some advanced aircraft and flight vehicles, such as the Concorde supersonic aircraft and Advanced Medium Range Air to Air Missile (AMRAAM), make use of air-breathing propulsion systems. One of the primary components of this propulsion system is the air inlet which compresses air from supersonic to subsonic conditions. It supplies atmospheric air to the combustion chamber and when fuel and heat are added, the combustion process takes place.

The integration of the air inlet with the total propulsion system results in certain penalties such as in increase in aerodynamic drag. The problem associated with the drag of a specific type of inlet namely, a two-dimensional external compression inlet was investigated. It is of the greatest importance to evaluate and quantify this drag penalty to ensure that each and every component of the inlet system is designed for good flow properties with as little drag as possible.

The need for this study arose because no useful figures are available to determine the aerodynamic drag of a two-dimensional external compression inlet with fixed geometry. The originality of this work is based on the independent critical discernment of known facts where information and equations are combined in a unique manner for determining drag figures.

The project was carried out in three phases, namely a theoretical investigation, where a flow analysis of the multiple factors influencing aerodynamic drag, was done. A full-scale inlet model, with the correct geometry and of flight-weight construction, was evaluated during an intensive wind-tunnel test program. In the last phase, a comparison between the theoretical values and experimental data, was done for validating the predicted aerodynamic drag figures.

The main objective of the research carried out, is to establish over which range of mass flow ratios the theoretical equations can be used to calculate the drag of a two-dimensional external compression inlet, with confidence. A major cost saving can be obtained when expensive wind-tunnel and field tests are scaled down due to the availability of information from which drag values can be calculated.

This study should make a significant contribution to technology since theoretical equations have been compiled into techniques which were extensively evaluated during wind-tunnel tests.

CHAPTER 2

LITERATURE SURVEY

2.1 INTRODUCTION

The physical layout of an air inlet consists of the complete ducting system upstream of the combustion chamber as shown in Figure 2.1. The purpose and requirements of an air inlet are as follows (Jet Engines 1980:1) :

- To compress supersonic air flow to subsonic flow and diffuse it to conditions which are acceptable for combustion to take place;
- to allow the required amount of air to enter the engine;
- to ensure a stable flow;
- to keep the loss in total pressure to a minimum;
- to provide air to the engine face with a uniform velocity across the duct;
- the inlet must have as little sensitivity as possible to angle of attack and yaw;
- the inlet must satisfy the system requirement over a range of flight speeds and engine demands;
- all inlet drag components must be kept to a minimum.

In supersonic applications inlets are often called inlet diffusers. For a better understanding of terminology it is worth mentioning that the term "Intake" is used in the United States of America while the term "Inlet" is used by the British (Seddon 1988).

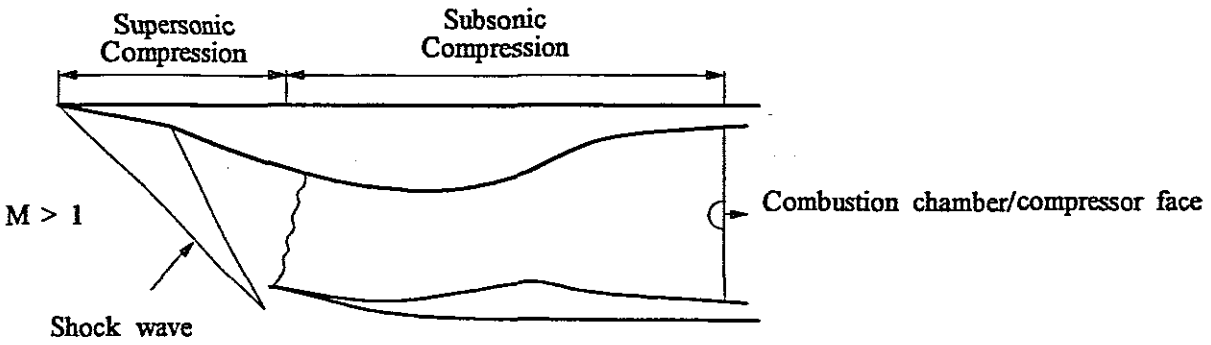

(a) Layout of Supersonic Inlet Duct

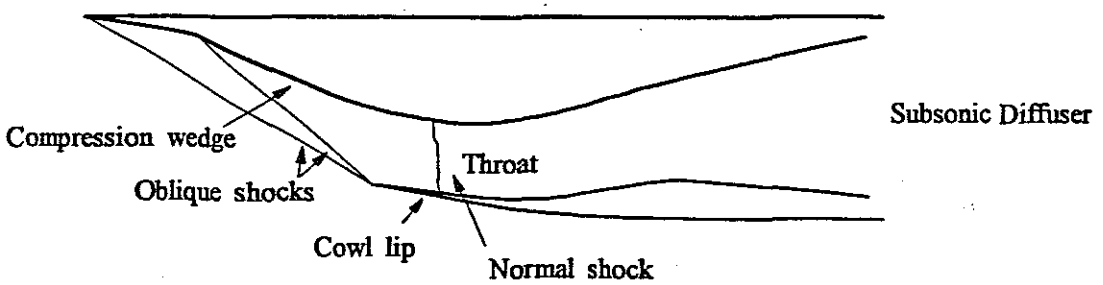

(b) Shock distribution

FIGURE 2.1 : Supersonic Inlet Duct

The main features of the inlet system are depicted in Figure 2.2. The primary function of each of these components is described by Gregoriou (1985:3). The incoming flow is divided by the cowl lip into an external and internal flow stream. The cowl forms the external surface of the inlet and its purpose is to turn the incoming flow into the entry opening. The cowl profile has a significant influence on the drag of the inlet. The compression surfaces for a supersonic inlet are usually situated upstream of the cowl lip. The purpose of the compression surfaces or wedges is to generate a shockwave system resulting in the compression of the incoming air-flow. The inlet shown in Figure 2.2 has sidewalls to enclose the two-dimensional entry flow. The subsonic diffuser, as shown in Figure 2.1, decelerates the subsonic flow to the required condition (Mach number) at the engine face or combustion chamber entry. The function of the boundary layer diverter (shown in Figure 2.2) is to prevent low energy boundary layer air from entering into the inlet. The inlet afterbody streamlines the inlet duct and forms a fairing

between the inlet and the fuselage. The main purpose of this fairing is to prevent base drag caused by the rear blunt end of the inlet duct.

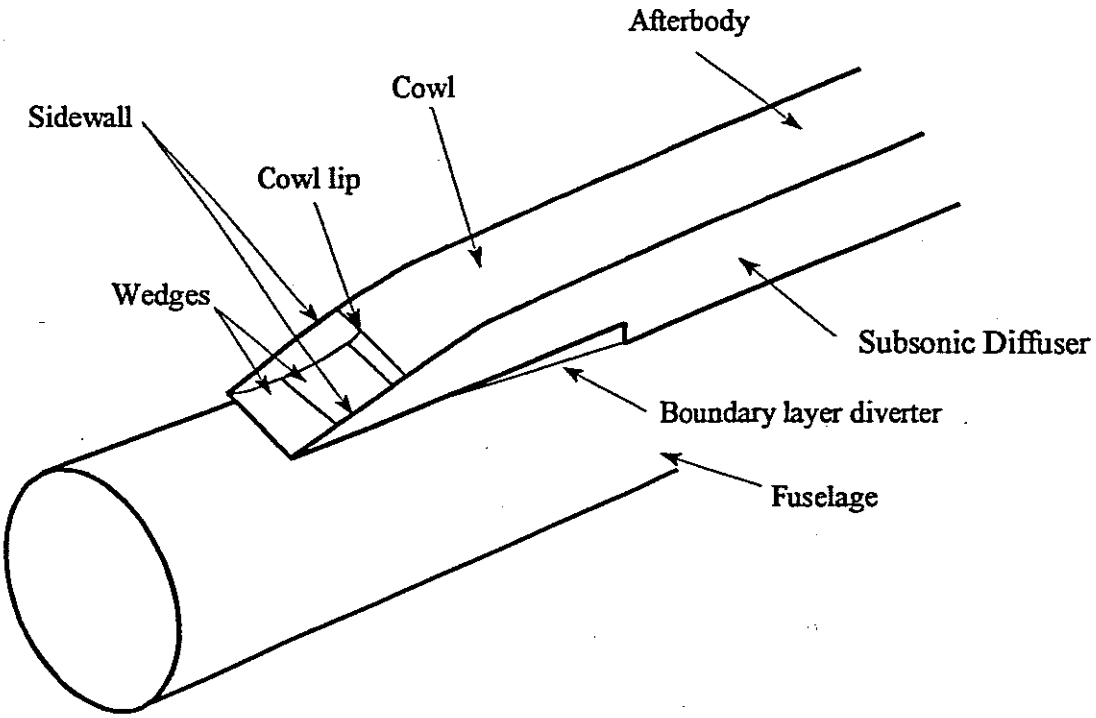

FIGURE 2.2 : Main Features of Inlet System

The inlet type is defined by the shape of the entry section. Part of the incoming flow is compressed in front of the inlet entry and part of the flow is further compressed within the inlet duct in the diffuser section.

2.2 TYPES OF INLETS

The performance of the inlet (Laruelle 1987) plays a very important role in the manoeuverability and performance characteristics (Pressure Recovery, Mass Flow Ratio, Drag) of a missile. For tactical missile applications, primarily three inlet configurations, as shown in Figure 2.3, are being used (Bendot et al. 1984) :

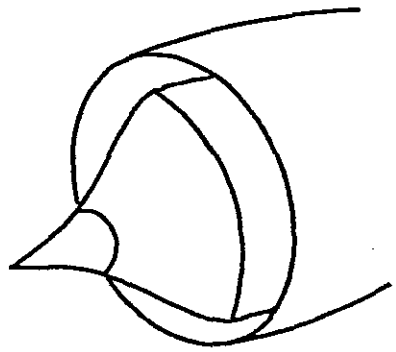

(a) Axisymmetric Inlet

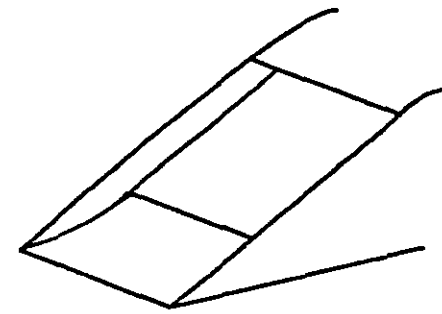

(b) Two-dimensional Inlet

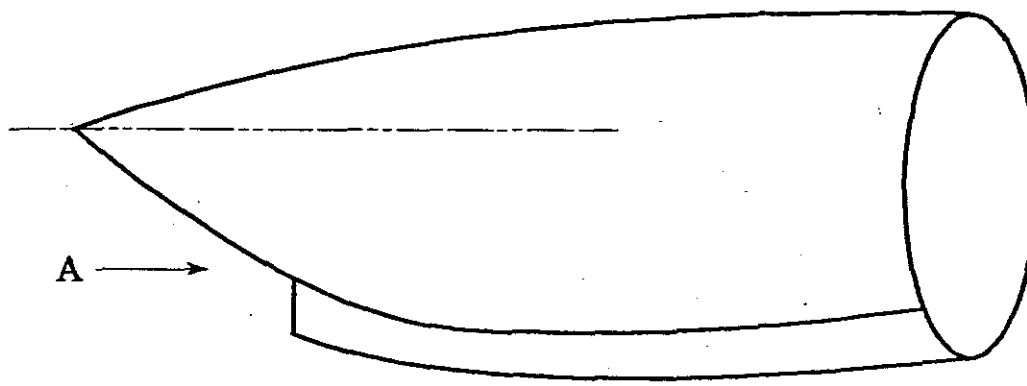

(c) Chin Inlet

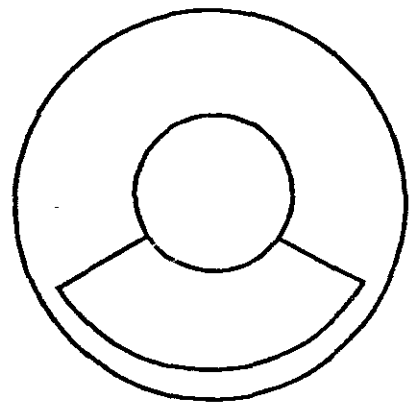

View A (Chin Inlet)

FIGURE 2.3 : General Configurations for Supersonic Inlets

The three inlet configurations have the following names :

- Axisymmetric
- Two-dimensional/rectangular
- Chin.

According to Bendot et al. (1984) the performance of an axisymmetric inlet deteriorates rapidly with an increase in angles of attack. For two-dimensional and chin inlet configurations an improvement in performance with increasing positive (nose-up) angles of attack is encountered.

Two-dimensional and chin inlets are being incorporated in the design of modern high performance missiles which use air-breathing (ramjet) propulsion systems.

The performance modes of the following types of supersonic inlets, as shown in Figure 2.4, will be discussed in more detail :

- Pitot inlet
- External compression inlet
- Internal compression inlet
- Mixed compression inlet.

2.2.1 Pitot Inlet

This is the most simple type of inlet where the air-flow is retarded through a single normal shock to subsonic conditions. This inlet is normally used up to a flight Mach number of $M_\infty = 1{,}8$ (Surber & Numbers 1988). The stagnation pressure recovery of this inlet rapidly deteriorates with higher Mach numbers and is consequently not suitable for modern high speed, high performance missile applications.

2.2.2 External Compression Inlet

This type of inlet makes use of a number of oblique shocks to retard the air-flow before the

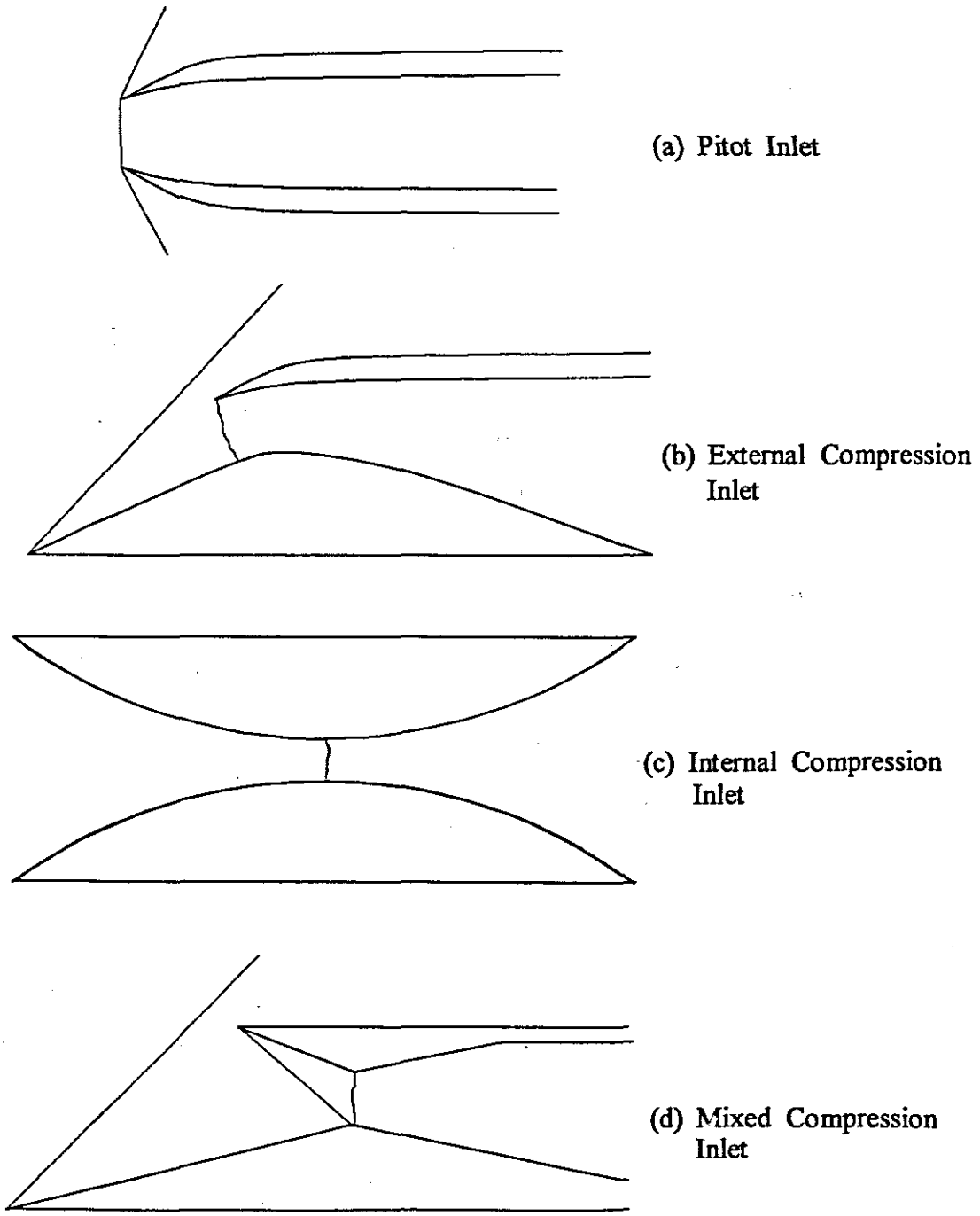

FIGURE 2.4 : Types of Supersonic Inlets with Normal Shock at Throat

terminal or normal shock is encountered as shown in Figure 2.4 (b). The oblique shock(s) are generated with the aid of wedge shaped surface(s) situated in front of the cowl lip. Although a better stagnation pressure recovery can be achieved by increasing the number of oblique shocks, it was found (Jet Engines 1980) that it is not practical to use more than two external wedge surfaces due to complications in the flow. The stagnation pressure recovery of this two-wedge inlet is less satisfactory than an isentropic compression inlet. The concept of "isentropic" compression is explained by Seddon (1988:9) where the air-flow is compressed by a multi-shock system on a smoothly contoured compression surface (Oswatitsch 1947). This produces an infinitely large number of weak oblique shocks which compress the supersonic air-stream with theoretically no loss in stagnation pressure. With an isentropic compression inlet very high drag is encountered due to the big angle through which the flow is turned on the curved compression surface before it enters the inlet opening. The advantage of high stagnation pressure recovery achieved with this inlet is to a great extent cancelled out by the much higher drag encountered on the steeply curved cowl lip (Conners & Lovell 1957).

An advantage of a two-wedge external compression inlet is that the construction is relatively simple and the optimum configuration is normally determined experimentally in a wind-tunnel.

2.2.3 Internal Compression Inlet

After the supersonic air-stream has entered the inlet, it is retarded by an internal contraction in the inlet duct as shown in Figure 2.4 (c). This type of inlet has a low drag value because external deflection and disturbance of the entering flow are prevented. A disadvantage of this type of inlet is that a stable shock system with normal shock swallowed (inlet started) is not easily established because of the instability of a normal shock in a converging channel (Jet Engines 1980). It is furthermore difficult to start this inlet and a complex variable geometry inlet is required to achieve this.

A method to start this type of inlet is to raise the air-speed to a value higher than the design condition (Jet Engines 1980). Once a stable shock system is established the air-speed is lowered to the design condition. This is however a very uneconomical method to start the inlet and a real danger exists that the inlet can become unstarted during flight as a result of an

and a real danger exists that the inlet can become unstarted during flight as a result of an increase in back pressure from the combustion chamber.

2.2.4 Mixed Compression Inlet

Of all the inlets discussed, this inlet as shown in Figure 2.4(d), delivers the best results with reference to stagnation pressure recovery (Jet Engines 1980). The advantage of a better stagnation pressure recovery is cancelled out to a great extent by the need to control flow separation in the inlet duct. The flow separation is caused by the interaction of the internal shock systems (oblique and normal shocks) with the boundary layer. This instability in flow conditions can result in the normal shock moving upstream, jumping out of the inlet opening and causing the inlet to become unstarted.

It is of significant importance to understand how the performance of an inlet system influences the drag.

2.3 PERFORMANCE CHARACTERISTICS

The performance of an inlet is characterized by three important parameters, namely pressure recovery, mass flow ratio and boundary layer bleed. Each one of the above-mentioned has an effect on the overall or total drag figure of an inlet.

2.3.1 Pressure Recovery

The inlet total pressure recovery is defined by Seddon (1988:5) as the ratio of the mean total pressure at the engine face to the total pressure available in the free stream, infinitely far upstream of the inlet.

$$P_R = \frac{P_{of}}{P_{0\infty}}$$

Where:

P_{of} = Stagnation pressure at engine face

$P_{0\infty}$ = Stagnation pressure in free stream

The total pressure recovery is an indication of the maximum pressure available in the combustion chamber and resultant thrust that can be developed.

With an increase in free stream (flight) Mach numbers, high shock losses and shock wave boundary layer interactions cause a decrease in total pressure recovery. Methods to remedy these high shock losses, eg. variable compression surface where oblique shocks are prevented from entering into the inlet, can result in an increase in drag. This is as a result of the greater angle through which the flow is turned before it enters the inlet opening.

2.3.2 Mass Flow Ratio

The mass flow ratio is defined by Gregoriou (1985:7) as the ratio of air mass flow at inlet entry to air mass flow at free stream conditions.

$$m_R = \frac{\dot{m}_c}{\dot{m}_\infty} = \frac{Actual\ mass\ flow}{Maximum\ possible\ mass\ flow}$$

Where :

$\dot{m}_c$ = *mass flow entering inlet*

$\dot{m}_\infty$ = *mass flow at free stream conditions.*

This mass flow ratio, m_R, can also be expressed as an area ratio since the equation for mass flow (Hall 1977:12) can be written as follows:

$$\dot{m} = \rho A V$$

Where:

ρ = air density

A = cross-sectional area

V = air velocity

With reference to free stream conditions, the values for P_∞ and V_∞ can be readily calculated from steady one-dimensional isentropic equations (Zucrow & Hoffman 1976) for a perfect gas. The area, $A_\infty = (h_\infty . w)$, defines the area of the stream tube entering the inlet. See geometrical layout in Figure 2.5. For the purpose of obtaining the properties of the air the control volume is defined in Figure 2.5. Therefore the equation becomes $\dot{m}_c = \rho_\infty A_\infty V_\infty$.

Similarly the maximum mass flow that can enter the inlet opening with a height, h_c, as shown in Figure 2.5, can now be calculated

$$\dot{m}_\infty = \rho_\infty V_\infty (h_c . w)$$

$$= \rho_\infty V_\infty A_c$$

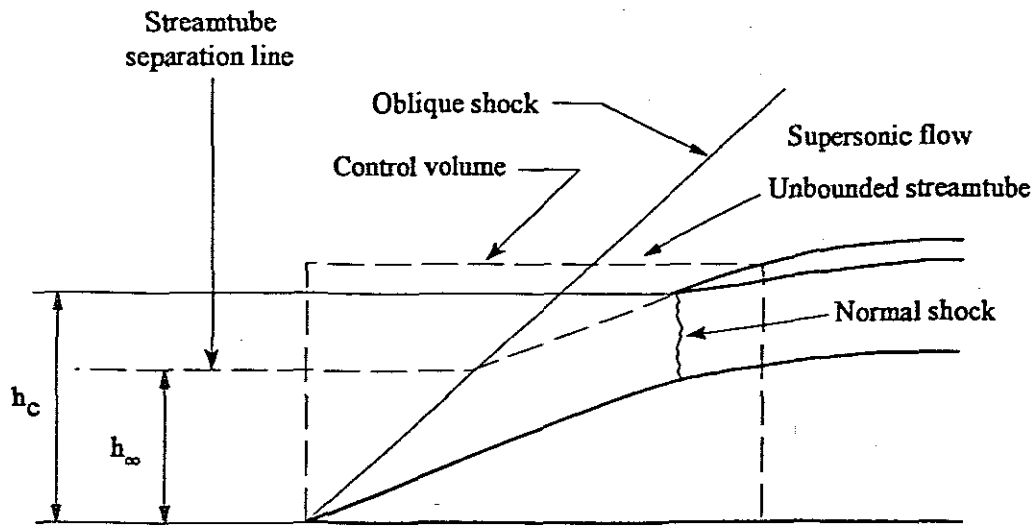

w = width of inlet opening
h_c = height of inlet opening
h_∞ = height of captured streamtube

FIGURE 2.5 : Geometrical Shape of Inlet Opening with Control Volume Defined

Therefore the ratio of actual mass flow to maximum possible mass flow can now be expressed in area ratio format as follows :

$$m_R = \frac{\dot{m}_c}{\dot{m}_\infty} = \frac{A_\infty}{A_c}$$

The inlet performance is represented by a typical characteristic curve which shows the relationship between mass flow ratio and stagnation pressure recovery at a specific flight Mach number. This curve is depicted in Figure 2.6. From this curve it can be seen that the inlet can function at different operating conditions, i.e. subcritical, critical and supercritical. These conditions, as discussed in section 2.4, play a significant role in the overall drag figure of the inlet.

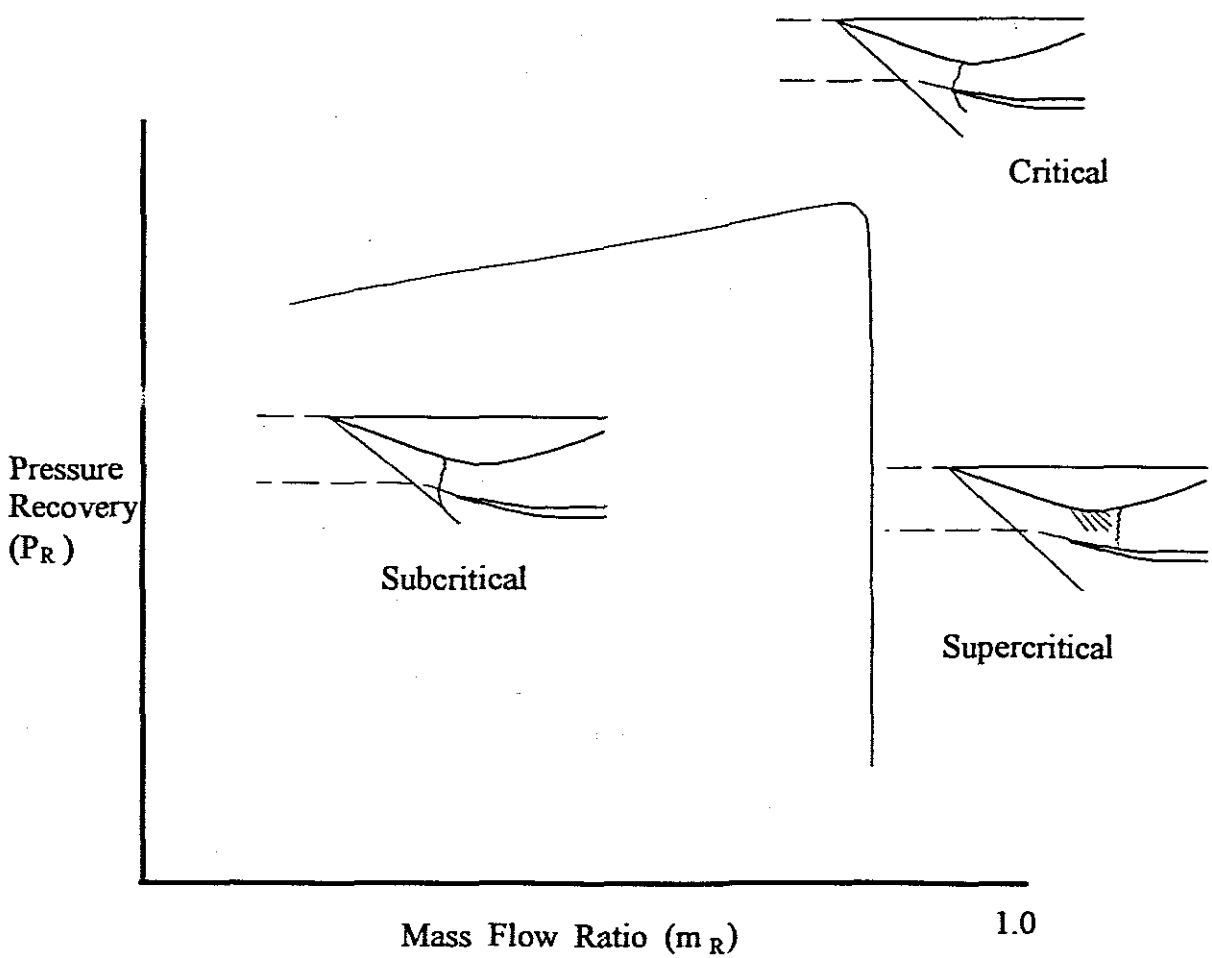

FIGURE 2.6 : Typical Performance Characteristic Curve for External Compression Inlet

2.3.3 Boundary Layer Bleed

The formation of a boundary layer on the compression surfaces of the inlet and the interaction of shocks with the boundary layer cause detrimental pressure gradients and the flow separates from the diffuser walls (Seddon 1988). It will result in an unsteady non-uniform distribution of flow at the engine face, a loss in stagnation pressure recovery, increased internal drag and too high Mach numbers due to the reduced flow area at the separation region. This is one of the most difficult problems to solve when designing supersonic air-inlet systems.

One of the more elegant designs for solving this problem is the Concorde-type slot bleed system as described by Leynaert (1988). A schematic layout of this design is shown in Figure 2.7 where a wide internal bleed slot is used. The flow from the internal cowl surface

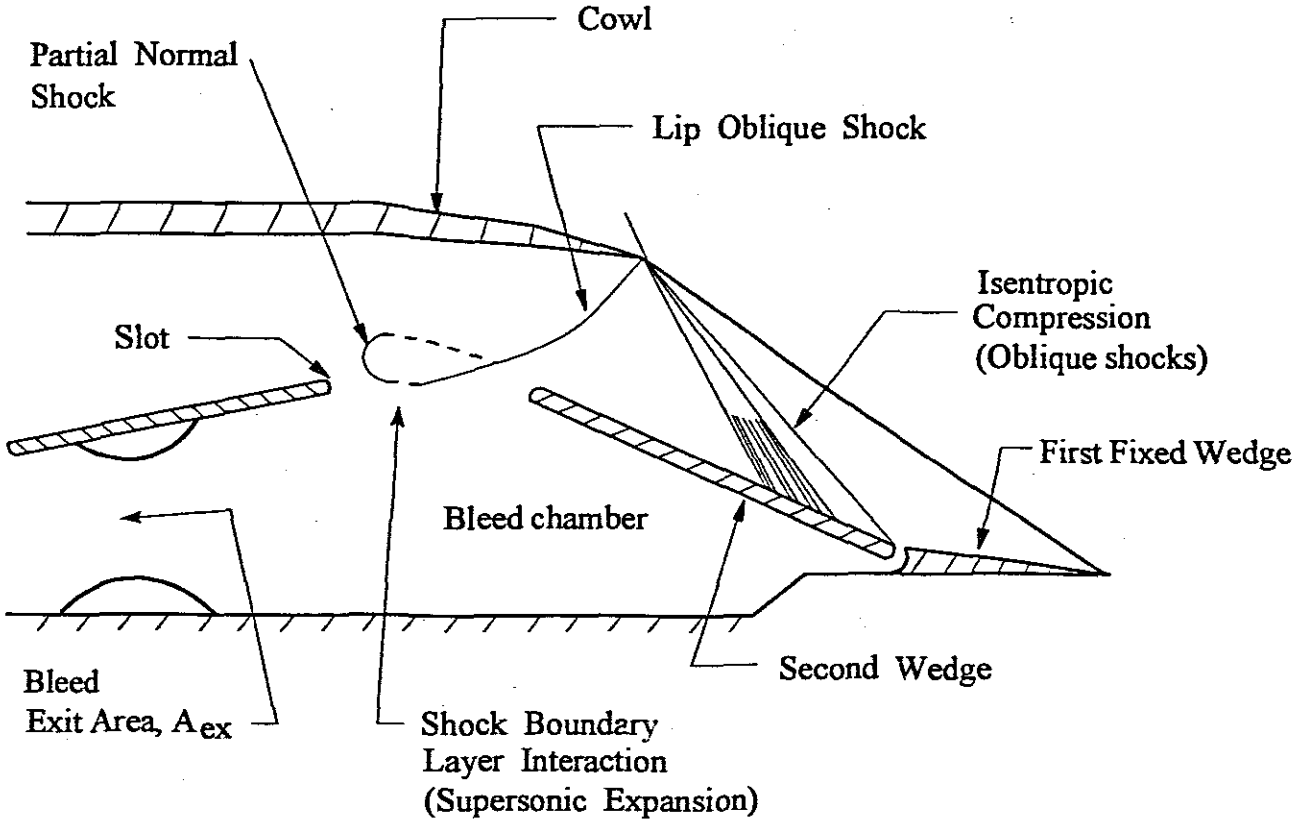

FIGURE 2.7 : Concorde-type Slot Bleed (Leynaert 1988)

is deflected internally through an oblique shock towards the throat slot where it is deflected onto the boundary layer which is initiated on the compression surfaces. This interaction causes a limited supersonic expansion which is terminated in a partial normal shock at the foot of the lip oblique shock. The pressure rise behind the normal shock causes the flow to turn into the bleed slot from where it is channelled to the atmosphere (for flight conditions) or tunnel test section (for experimental purposes). Typical bleed ratios used during inlet testing are, according to Seddon and Goldsmith (1985), between 4% and 12% of the captured mass flow.

2.4 MODES OF OPERATION

The three different modes of operation are characterized by the position of the normal shock in the inlet diffuser. Each one of these modes can occur at both design and off-design Mach numbers and is primarily a function of engine demand. Design and off-design Mach numbers can be explained as follows :

- At the design Mach number the oblique shock falls on the cowl lip;
- below the design Mach number the oblique shock falls in front of the cowl lip;
- above the design Mach number the oblique shock falls inside the cowl lip and this is a condition that is avoided because serious flow instabilities will occur.

The different modes of operation, as depicted in Figure 2.8, have an important influence on the performance and drag characteristics of the inlet. An inlet should ideally be operated at the critical condition, with normal shock at the cowl lip, (Figure 2.8(a)) where the inlet and the engine is matched. This means that the captured mass flow provides the exact amount of air required by the engine. At this operating point the stagnation pressure recovery is a maximum at a constant capture area ratio (Pearce 1959). This condition is also clearly depicted in Figure 2.6.

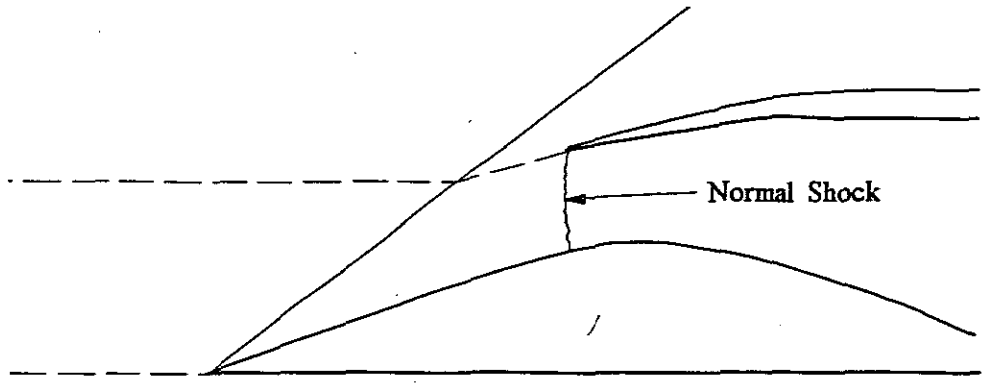

(a) Critical

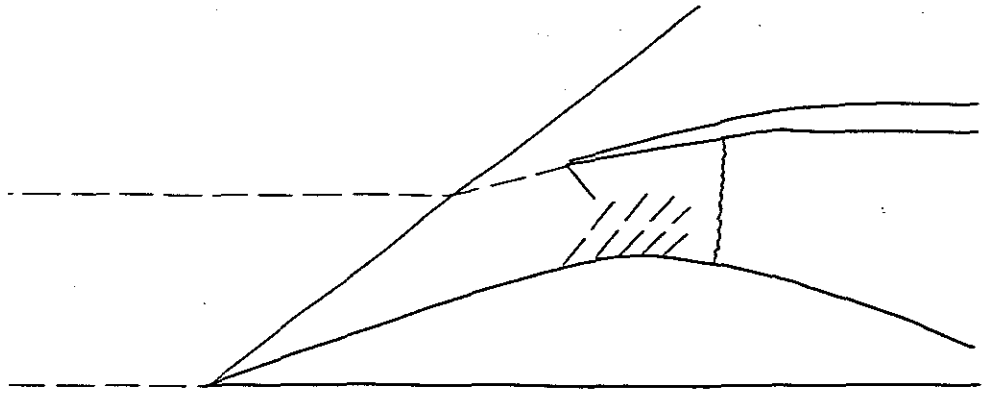

(b) Supercritical

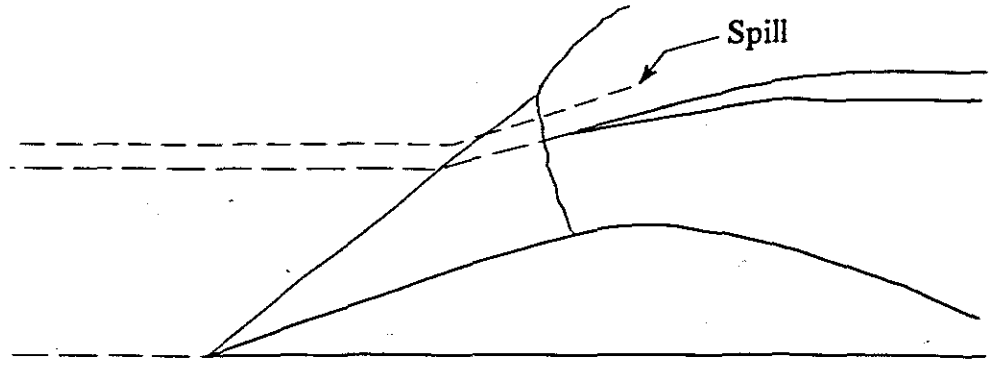

(c) Subcritical

FIGURE 2.8 : Modes of Operation for Supersonic Inlets

The supercritical operating condition (Figure 2.8(b)) occurs when the engine demands more air than the inlet can deliver. To compensate the normal shock moves downstream of the throat into the diverging section of the diffuser. The Mach number behind the normal shock increases and a resultant loss in stagnation pressure recovery is encountered at the engine face. At this condition the capture area ratio is the same as for the critical condition since the external shock system is unchanged.

When the engine mass flow demand is reduced below the critical requirement the excess air cannot enter the combustion chamber and the normal shock is pushed upstream out of the inlet opening. The normal shock is now situated in front of the cowl lip, as shown in Figure 2.8(c), and the excess air is spilled around the cowl lip. An unstable condition, known as "buzz", (Jet Engines 1980) occurs which is a very undesirable condition. This pulsating air-flow can set up large vibrations in the inlet structure and cause mechanical failure. Some inlets are however designed to operate in the subcritical mode with a margin of stable operation. Stagnation pressure recovery is normally equal to or less than the value for critical operation. The capture area ratio is less than one, since air is expelled from the inlet opening, with a resulting increase in drag due to the subsonic air-stream passing over the cowl lip.

It is of significant importance to consider the influence of drag on the performance of a "flying engine" (vehicle in flight) when discussing the design parameters.

2.5 DESIGN PARAMETERS

In designing inlet systems it is noted by Surber and Numbers (1988) that a compromise must be reached between performance and stability versus complexity and weight, keeping overall mission requirements in mind. Maximum pressure recovery, minimum drag, uniform and steady flow are the most significant design considerations mentioned for an inlet system.

2.5.1 Inlet Geometry

An inlet generally consists of the following main components as depicted in Figure 2.9:

- Compression surface
- Throat
- Cowl
- Subsonic diffusor.

The specific geometric shape of each component depends primarily on the application (missile or aircraft) and the mission requirements, i.e. maximum flight Mach number, angle of incidence and yaw angle.

For this study an external compression inlet was selected because of its stable operation and the fact (Surber & Numbers 1988) that it is customarily used in aircraft with supersonic flight capabilities of Mach number 2,5+.

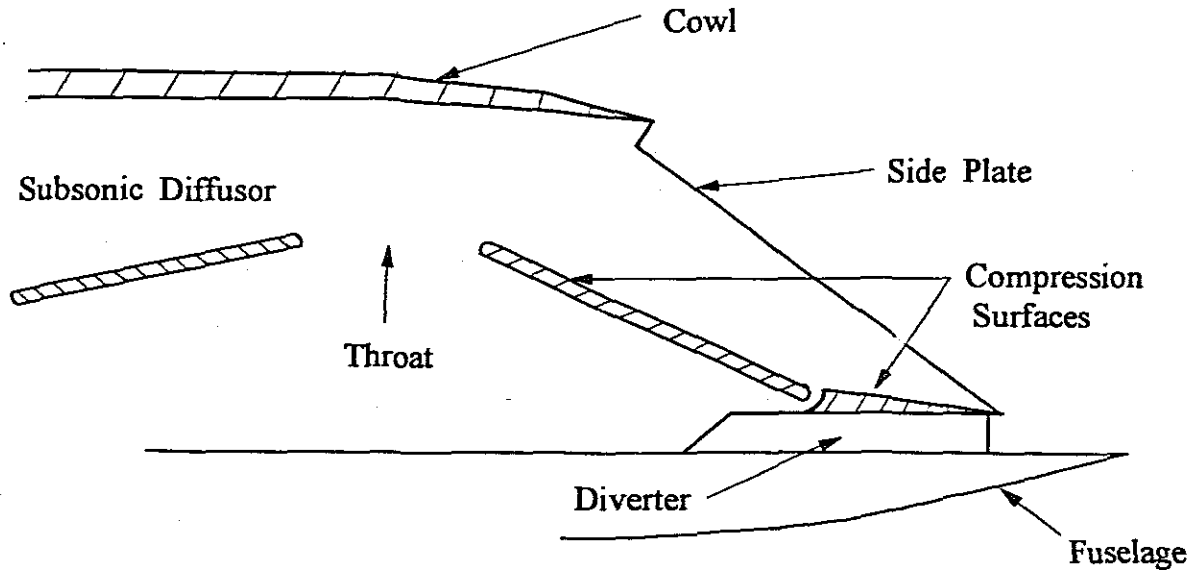

FIGURE 2.9 : Inlet Geometrical Layout

Although an isentropic compression inlet, as discussed in section 2.2.2, theoretically renders the most efficient stagnation pressure recovery, it has been found (Jet Engines 1980:3) that it is not feasible to use a compression surface with more than two oblique shocks because of greater flow complications.

2.5.2 Design Mach Number

At the design Mach number the oblique shocks, generated by the external compression surface, are focused on the cowl lip and at this operating point (critical and supercritical operation) there is no external interference of air-flow around the cowl lip. With the oblique shock on the cowl lip there is no unbounded streamtube because all the air-flow is captured by the inlet. Pre-entry drag, (section 3.2), is zero at the shock-on-lip operating condition. If the inlet is operating at below design Mach number the oblique shock is focused in front of the cowl lip with the supersonic flow of the unbounded streamtube around the cowl lip as shown in Figure 2.5. The pre-entry or additive drag is a function of the pressure force of the unbounded streamtube acting on the cowl external surface (Hawkins et al.1976).

2.5.3 Diverter Height

A method to prevent the boundary layer from the fuselage entering the inlet and cause flow instabilities, is to make use of a diverter. This is a device which is mounted between the fuselage or missile body and the inlet as is shown in Figure 2.9. The purpose of the diverter is to scoop off the low energy boundary layer air. A significant increase in stagnation pressure recovery and flow stability is achieved with a diverter height which is just greater than the thickness of the boundary layer (Bendot et al.1984).

It is indicated by Laruelle (1988) that a big improvement in the stagnation pressure recovery of a rectangular (two-dimensional) inlet, at different angels of attack, can be achieved by increasing the height of the diverter to 10% of the missile diameter. Although the increase in the diverter height causes an increase in the total drag of the missile, the gain in stagnation pressure recovery achieved is of great importance to the performance of the inlet.

2.5.4 Subsonic Diffuser

The stability of the air-flow in the subsonic diffuser has a great influence on the overall performance of the inlet. Flow separation, depicted in Figure 2.10, as a result of drastic changes in the contour of the diffuser wall should be avoided at all times. Loss in momentum due to flow separation and turbulence has a negative effect on drag caused by the internal flow of the inlet.

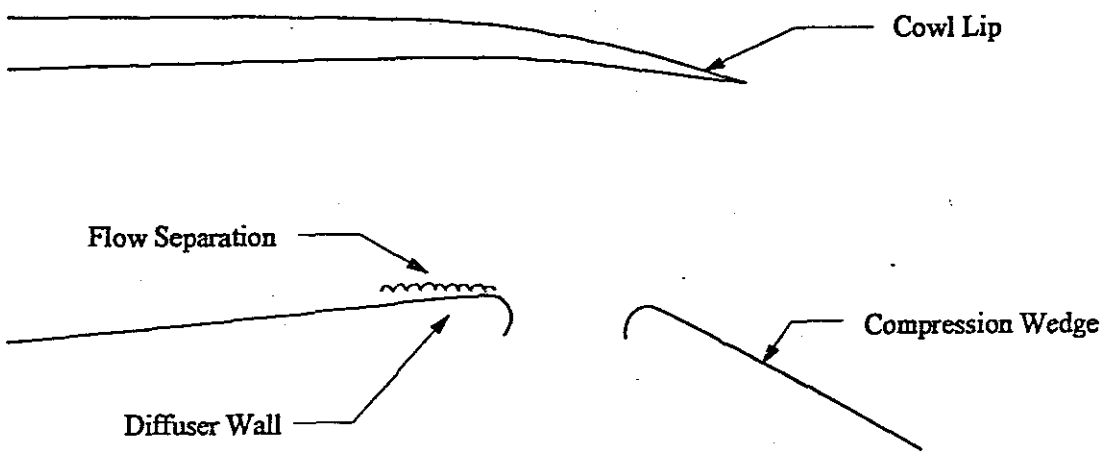

FIGURE 2.10 : Flow Separation on Diffuser Wall

Experimental work done by Tindell (1987) indicates that longer diffuser ducts with small expansion (diverging) angles render better limits for flow attachment. This means that higher flow limits are achieved before flow will separate from the diffuser walls and cause boundary layer blockage. For safe operation without any flow separation, diffuser expansion angles of 2° to 9° are generally recommended for area ratios of 1,7 to 2,9 (Surber & Numbers 1988).

Surber (1975) found that the length of the diffuser duct has very little influence on the stagnation pressure recovery of a realistic two-dimensional inlet. It is indicated by Lee and Boedicker (1985) that a subsonic diffuser with a gradual curvature and rapid expansion at the diffuser entrance is favourable for high stagnation pressure recovery and low boundary layer disturbances.

2.5.5 Cowl lip

At an external compression inlet the flow is turned away from the inlet centre line by the wedge surfaces. It is therefore necessary to turn the flow back to the axial direction at the inlet entry to allow the flow to enter the inlet. For efficient compression, relatively large angles for the cowl lip are required to turn the flow back into the inlet opening. Care must be taken to ensure that the external cowl lip angle does not exceed the maximum value specified for the flow turning angle (Zucrow & Hoffman 1976:744) where shock attachment will take place for a specific Mach number. It is important to note that a smaller value for the external cowl angle will result in a lower drag value for the cowl because the flow is turned through a smaller angle. It is therefore essential to find a compromise between stagnation pressure recovery and drag. The optimum cowl lip dimensions for the highest possible stagnation pressure recovery and lowest possible drag are generally determined through wind-tunnel tests.

2.5.6 Side Plates

Side plates, with cut-outs as shown in Figure 2.9, are used for rectangular inlets to improve performance at different angles of yaw (Laruelle 1988). Although an improvement in the stagnation pressure recovery is achieved with cut-outs in the side plates a loss in captured mass flow is experienced. This loss in mass flow has a negative effect on the performance of a "flying engine" which makes use of the air-breathing propulsion system. It is recommended that modifications, such as cut-outs on the side plates, should only be introduced if final adjustments to the inlet geometry are required for the improvement of stagnation pressure recovery. It is stated by Hall (1977) that the introduction of side plates may increase or decrease the pre-entry or additive drag of the inlet. Their effect is in all cases small when

compared to the force of the upper surface of the streamtube acting across the inlet opening on an area given by $(h_c - h_\infty)w$, as depicted in Figure 2.5.

2.6 REVIEW OF DRAG CONTRIBUTING COMPONENTS

The designers of air-breathing propulsion systems need tools to predict the behaviour and performance of a "flying engine" very accurately. The drag caused by the inlet has a significant influence on the amount of nett thrust available to fulfil the flight requirements. The total drag of the inlet consists of different drag contributing components characterised by a specific geometric shape and flight requirements. It is stated by Krieger and Vukelich (1986:414) that an in-depth survey of experimental data bases renders figures that are fragmented and incomplete for establishing the aerodynamic effects of inlet systems on the external aerodynamics of air-breathing missiles. It is therefore of crucial importance to establish an accurate figure for the drag of the inlet under discussion, namely a two-dimensional external compression inlet.

2.6.1 Pre-entry drag

The terminology for this major drag contributing component is described by Seddon (1988:13) where it is called pre-entry drag in the United Kingdom and additive drag in the United States of America. Hall (1977:18) considers the change in momentum between free stream conditions and the inlet entrance to cause an additional drag force, called pre-entry or additive drag. It is best represented by the following equation:

$$F_p = F_n - F_d - D_{pre}$$

Where:

F_p = Nett propulsive thrust

F_n = Nett trust due to momentum change between free stream conditions and engine exit

F_d = External drag forces

D_{pre} = Pre-entry drag

Pre-entry drag is encountered during the following two situations:

(i) Inlet is operating critically or supercritically below the design Mach number as shown in Figure 2.8.

(ii) Inlet is operating critically or supercritically at the design Mach number.

In the first case the inlet is operating with the oblique shock in front of the cowl lip with the unbounded streamtube acting over the entrance of the inlet. The static pressures behind the oblique shock act across an area defined by $(h_c - h_-)w$, as depicted in Figure 2.5.

In the second case the inlet is operating with the oblique shock at the cowl lip. The flow is supersonic up to the cowl lip, undisturbed with no loss in momentum. At this operating condition the pre-entry drag is zero.

The calculation of pre-entry drag (supersonic spillage) is fully described in sections 3.2.1. and 3.3.1.

2.6.2 Spillage drag

With the inlet operating at or below the design Mach number, a condition may occur where the normal shock is pushed out in front of the inlet with subsonic flow behind the normal shock. This form of pre-entry drag at subcritical operation is called subsonic spillage. The drag force is based on pressures behind the various shocks and the calculations are fully described in sections 3.2.1 and 3.3.2.

2.6.3 Cowl drag

The cowl forms the external surface of the inlet duct as depicted in Figure 2.2. The cowl lip turns the oncoming flow into the inlet opening and divides the flow into an internal and

external component. The external shock system causes a pressure force on the outer cowl surface and lip. The shape of the cowl profile and static pressures behind the various shocks determine the magnitude of the cowl drag force. This drag force is based on the wave pressure (shock - expansion method) and skin friction drag as discussed in sections 3.2.2 and 3.3.3.

The inlet cowl is a component with a significant contribution (Gregoriou 1985) to the total drag of the inlet. It is therefore important to make use of cowls with slender profiles (small external angles) for application in "flight vehicles" with supersonic capabilities to reduce wave pressure drag.

2.6.4 Bleed drag

It is noted by Gregoriou (1985) that neither vortices from the forebody of the fuselage, nor the boundary layer from the compression surface, should enter the inlet. This low energy air will have an adverse effect on stagnation pressure recovery with a resultant loss in performance. The low energy air (boundary layer) is removed by means of a boundary layer trap or slot at the throat section, as depicted in Figure 2.7, and dumped overboard to atmospheric conditions. The bleed mass flow loses momentum, when turned away from the main captured mass flow into a bleed chamber, with the resultant drag penalty. The bleed drag is not a major drag contributing component and the increase in stagnation pressure recovery achieved outweighs the drag penalty (Surber & Numbers 1988).

The theoretical determination of this drag component is fully described in sections 3.2.3 and 3.3.4.

2.6.5 Diverter drag

The diverter, as shown in Figure 2.9, can be defined as a scoop situated between the inlet and the fuselage with the purpose of preventing lower energy or turbulent air from entering the inlet. The drag associated with this component is caused by wave pressure (static pressures

behind shock waves) and skin friction. Although this is not a major drag contributing component, the shape and the height of the diverter should be optimised to find a trade-off between good stagnation pressure recovery and drag (Hall 1977).

2.7 SUMMARY

From the literature it is clear that no usable drag coefficient, characterising the overall drag of a standard two-dimensional external compression inlet, could be found. In combining the general information, found from the work of the previous authors, equations are presented in a manner unique to this specific type of inlet. Theoretical drag figures, based on these equations, are fully described for actual flight conditions in section 3.3 of the next chapter.

CHAPTER 3

THEORETICAL CONSIDERATIONS

3.1 INTRODUCTION

This subject is not discussed in sufficient detail in the literature and an attempt is made to describe the different types of drag forces acting on the inlet system. The terminology used by different authors does not always correlate properly and therefore care is taken to give descriptions of the different types of drag using common terminology.

For an inlet with a specific geometric shape and location on the airframe, the drag as defined in section 3.2, is caused by skin friction and flow conditions through the inlet system. The two flow conditions which contribute to this drag are firstly, when the inlet is operating at maximum mass flow conditions without any spilling of external air around the cowl; secondly, when the entry airflow is reduced from the maximum value, resulting in excessive air-spillage around the cowl lip.

According to Leyland (1988) spillage drag is the main contributing factor when assessing drag. The methods given for estimating inlet drag are only adequate for initial system design purposes and accurate results can only be obtained through experimental force measurements.

Thrust is required to overcome total drag and to maintain or accelerate a body in flight. It is therefore important to look at the definition given by Seddon and Goldsmith (1985), where the thrust of a ramjet is defined as the resultant force in the direction of flight produced on the aerodynamic duct system by the internal flow.

The main design objective is to produce an inlet system with good pressure recovery and

qualities because these factors have an effect on the combustion process and resulting engine thrust.

3.2 DRAG COMPONENTS

The inlet drag is defined as the resultant force, opposing the direction of flight, produced on the aerodynamic duct system by external and internal flow (Seddon & Goldsmith 1985), i.e. the total additional drag on the missile as caused by the inlet.

The external drag is consists mainly of spillage drag (dumping excessive air overboard), pre-entry drag (with oblique shock in front of the cowl lip at a Mach number below design value), cowl drag (wave pressure drag), friction drag and boundary layer diverter drag. Internal drag is primarily caused by bleeding off the boundary layer through ramp and throat bleeding systems. The significance of bleed drag is much less than the drag caused by the external flow conditions mentioned above. It is therefore important to consider each drag contributing component separately.

3.2.1 Spillage Drag

The drag caused by a reduction in the entry flow from a maximum value, defined by the inlet capture area A_c, is called the spillage drag. Great consideration is given to this drag component because it makes a significant contribution to the total inlet drag. In general the calculations for spillage drag are based on the pre-entry streamtube force caused by a mass flow ratio less than unity.

Procedures for determining spillage drag also depend on the inlet geometry such as the shape of sidewalls and whether the inlet uses external compression or not.

For the purpose of this report only two-dimensional inlets with external compression at supersonic speeds are dealt with. Two types of spillage drag are mentioned in the literature (Seddon & Goldsmith 1985) namely:

i). Supersonic spillage where the flow remains supersonic up to the inlet opening, which means that the normal shock falls on or inside the cowl lip. In this case the spillage drag is equivalent to the pre-entry drag where the inlet is operating critically or super-critically below the design Mach number. When the inlet is operating at or above the design Mach number with the normal shock at or inside the cowl lip, the additive or pre-entry drag is zero (Hall 1977).

ii). When the mass flow is reduced to a point where the inlet is operating subcritically, i.e. with the normal shock in front of the inlet entry, the oblique shock is pushed away from the cowl lip causing the excess flow to spill around the lip. The mass flow ratio is reduced below the maximum value with subsonic flow behind the normal shock in front of the inlet entry. This condition is called subsonic spillage and the drag component consists of pre-entry as well as spillage drag.

These two conditions are illustrated in Figure 3.1.

3.2.1.1 Pre-entry Drag at Supersonic Spillage

In the case where only supersonic spillage is encountered, the pre-entry drag for a single-wedge external compression surface can be derived from the following equation taken from Seddon and Goldsmith (1985) :

Where:

Pre-entry drag = Pressure differential × projected area as shown in Figure 3.2.

$$(D_{pre})_a = (P_1 - P_\infty)\left[A_c - (A_\infty)_{max}\right] \quad (1)$$

Where:

a = Conditions for supersonic spillage at maximum flow.

P_∞ = Free stream static pressure

P_1 = Static pressure behind oblique shock

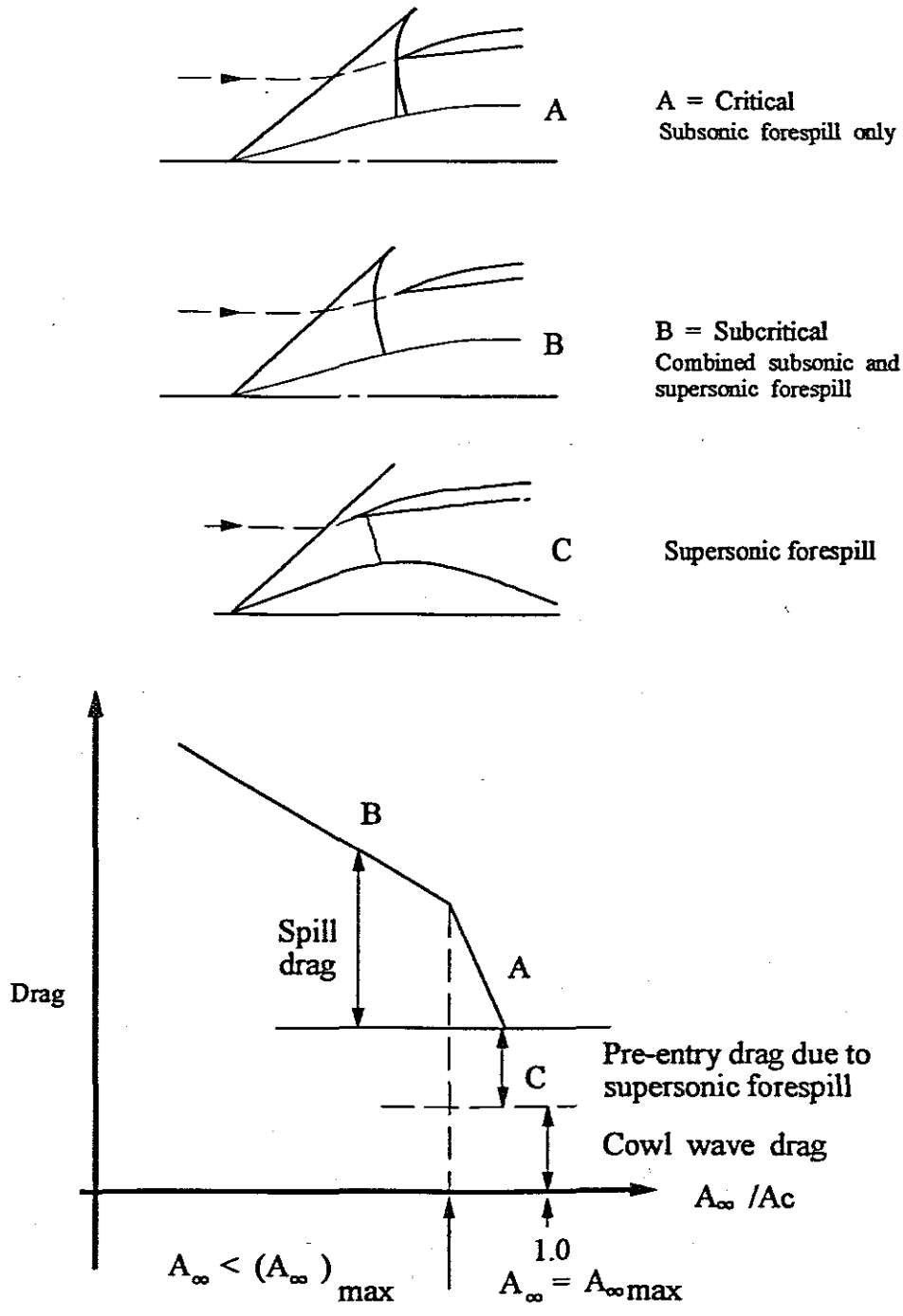

FIGURE 3.1 : Cowl Wave Drag and Spillage Drag Components for an External Compression Inlet (Leyland 1988:20)

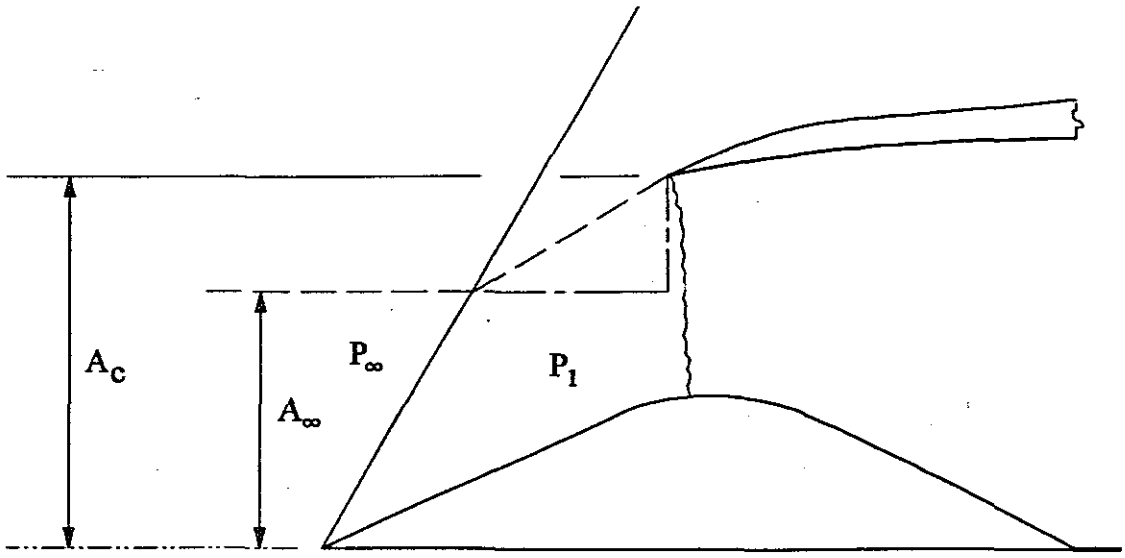

Projected Area = $A_c - A_\infty$

Pressure Differential = $P_1 - P_\infty$

Where : $\left(\frac{A_\infty}{A_c} \right)_{max} < 1.0$

FIGURE 3.2 : Supersonic Spillage for a Single-wedge External Compression Surface

A_c = Capture area

A_∞ = Streamtube area

Maximum flow ratio can be defined as the condition where the oblique shock lies in front of the cowl lip with the normal shock at or inside the lip (critical or supercritical operation). The mass flow ratio A_∞ / A_c is less than one because there is a deflection in the flow through the oblique shock where the flow is turned parallel to the compression surface.

With:

$(A_\infty/A_c)_{max} = 1,0$ Full flow with oblique shock on lip.

And

$(A_\infty/A_c)_{max} < 1,0$ with oblique shock in front of lip.

Equation 1 can now be written in coefficient form:

$$(C_{d_{pre}})_a = \frac{Drag}{q_\infty A_c}$$

$$(C_{d_{pre}})_a = \frac{P_\infty}{q_\infty}\left(\frac{P_1}{P_\infty} - 1\right)\left[1 - \left(\frac{A_\infty}{A_c}\right)_{max}\right] \qquad (2)$$

Where:

q_∞ = Free stream dynamic pressure.

The value for the maximum flow ratio which is equivalent to the area ratio, A_∞/A_c, as discussed in section 2.3.2 for a single-wedge compression surface with the oblique shock in front of the lip, can be derived from the following equation taken from Seddon and Goldsmith (1985) :

$$\frac{A_\infty}{A_c} = \frac{(L_N - \ell_n)\tan \epsilon}{L_N \tan \epsilon_D} \tag{3}$$

Where all the relevant dimensions are shown in Figure 3.3.

L_N and ℓ_n = Horizontal dimensions

δ = Wedge angle

ϵ = Shock wave angle

ϵ_D = Shock wave angle between lip and horizontal plane of wedge at design point.

For an inlet with a double-wedge compression surface the pre-entry drag at maximum flow conditions can be determined from the equation obtained from Seddon and Goldsmith (1985):

$$(D_{pre})_a = (P_1 - P_\infty)\left[A_1 - (A_\infty)_{max}\right] + (P_2 - P_\infty)(A_c - A_1) \tag{4}$$

Where: P_2 = Static pressure behind second oblique shock

A_1 = Area enclosed by the maximum-flow streamtube at its intersection with the second oblique shock.

The stream-tube areas are shown in Figure 3.4.

In coefficient form equation 4 is reduced to the following equation:

$$(C_{D_{pre}})_a = \frac{P_\infty}{q_\infty}\left(\frac{P_1}{P_\infty} - 1\right)\left[\frac{A_1}{A_c} - \left(\frac{A_\infty}{A_c}\right)_{max}\right] + \frac{P_\infty}{q_\infty}\left(\frac{P_2}{P_\infty} - 1\right)\left(1 - \frac{A_1}{A_c}\right) \tag{5}$$

3.2.1.2 Subsonic Spillage

Subsonic spillage is encountered when the normal shock is pushed out in front of the inlet

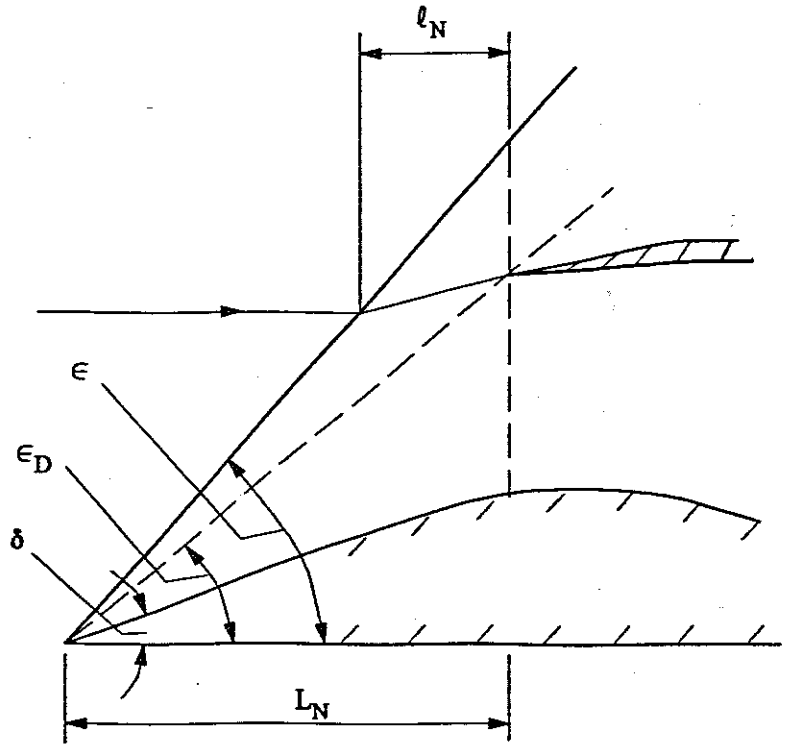

FIGURE 3.3 : Maximum Flow Ratio with Oblique Shock in Front of Lip

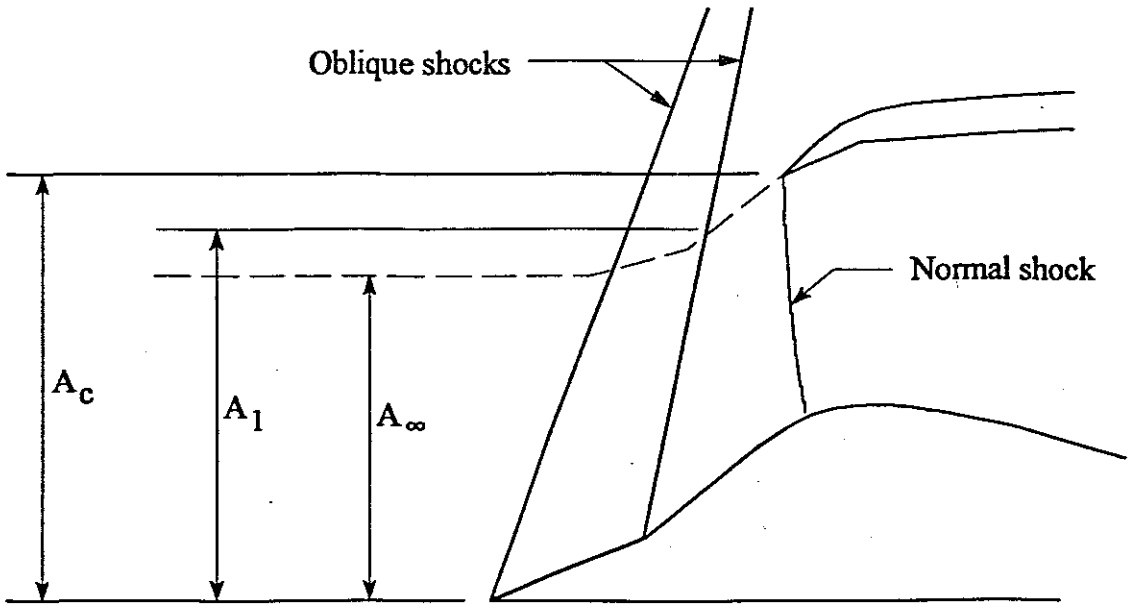

FIGURE 3.4 : Streamtube Areas for a Double-wedge Compression Surface with Supersonic Spill

entry causing the flow behind the normal shock to be subsonic. The flow is now reduced from its maximum value. At this condition the total spillage drag consists of two components namely: (a) pre-entry drag due to the oblique shock in front of the cowl lip and (b) spillage drag due to the dumping of excess air through the normal shock in front of the cowl lip as depicted in Figure 3.1 condition B.

A method for determining the subsonic forespill drag is given by Seddon and Goldsmith (1985) where the Fraenkel method for pitot intakes is used to determine the spillage drag for different positions of the compression surface with respect to the cowl lip. This method is adjusted to give the spillage drag for a bluff solid body with a bow shock wave where the external geometry is the same as that of the inlet.

The projected area, A_b, at point b in Figure 3.5 is determined by the linear movement of the normal shock from L = 0 to L = L_{max} where L_{max} is the distance in front of the lip for a bow shock on a solid bluff-body with the same external geometry as that of the inlet. When L = 0 the normal shock is located at or inside the cowl lip and $A_\infty = (A_\infty)_{max}$, but with L = L_{max} the normal shock is far upstream of the entry and the inlet becomes unstarted with a bow shock in front of the inlet, resulting in $A_\infty = 0$.

At some stage the normal shock intersects with the dividing streamline of the streamtube as shown at point b in Figure 3.5. At this point the inlet is operating subcritically and for other reduced flow ratios the spill drag can be determined (Seddon & Goldsmith 1985) for case B in Figure 3.5 for which $\epsilon > \epsilon_D$, and

$$D_{spill} = (P_3 - P_\infty)(A_c - A_\infty) - (D_{pre})_a \qquad (6)$$

Where:

P_3 = Static pressure behind normal shock

$(D_{pre})_a$ = Pre-entry drag at maximum flow conditions

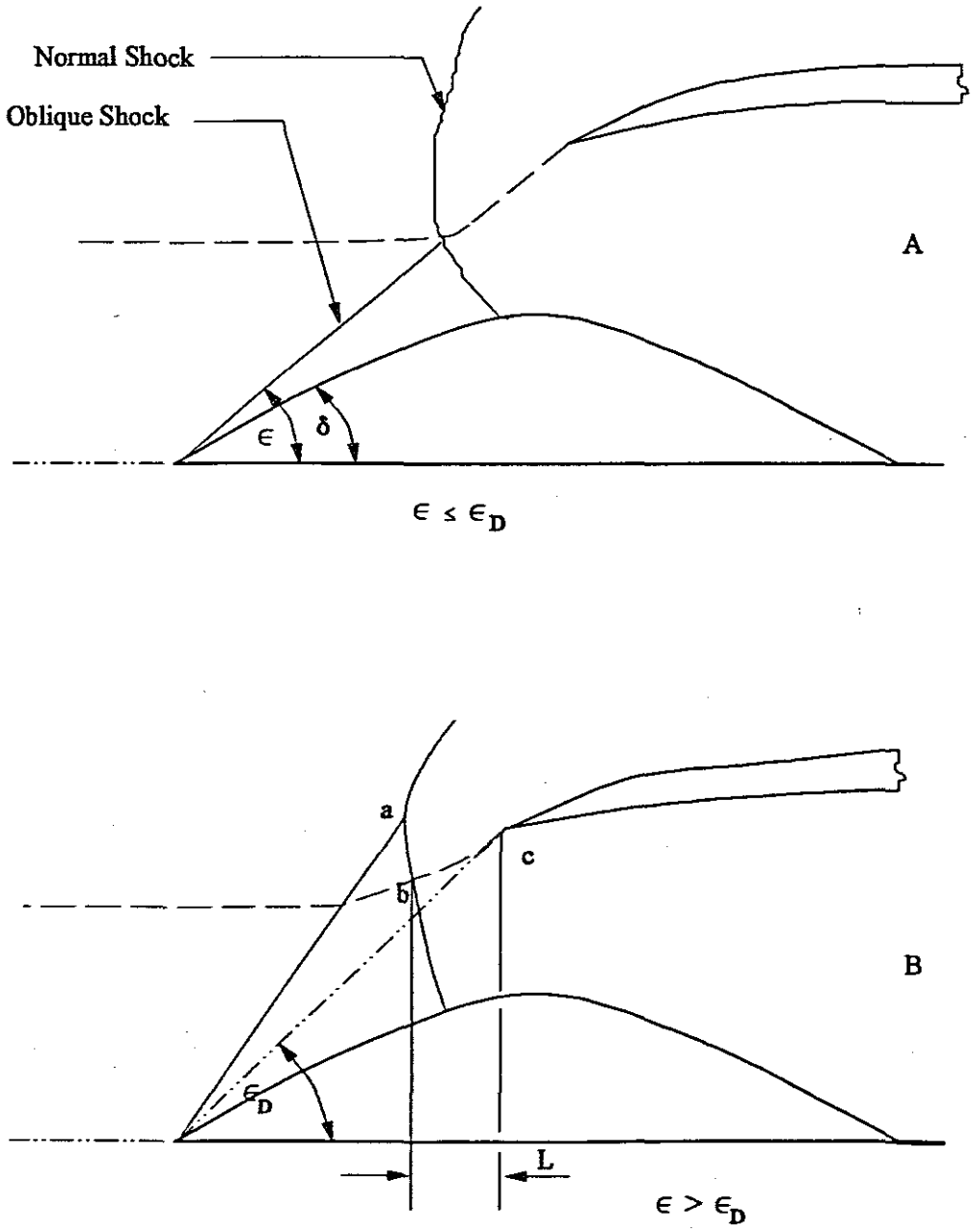

FIGURE 3.5: Subsonic Spill at Different Oblique Shock Positions

When the inlet is operating with $\epsilon \leq \epsilon_D$, as shown in case A of Figure 3.5, the pre-entry drag, $(D_{pre})_a$, becomes zero resulting in a spillage drag for this case:

$$D_{spill} = (P_3 - P_\infty)(A_c - A_\infty) \tag{7}$$

For the purpose of theoretical calculations the values of P_∞ and P_3 can be determined from the isentropic relations and shock tables (Zucrow & Hoffman 1976) for given free stream Mach numbers and inlet geometries. Values for A_∞/A_c are obtained from mass flow measurements during wind-tunnel tests with the inlet operating at different flow conditions.

3.2.2 Cowl Drag

One of the main components of inlet drag is the cowl-pressure drag. For the purpose of this report only two-dimensional inlets with sharp-lipped cowls are considered.

The prediction of cowl-pressure drag is achieved by means of the shock-expansion method as discussed by Seddon and Goldsmith (1985).

The drag of the first element with length, $d\ell_1$, taken from the first inclined section at an angle η_o to the free stream flow, as shown in Figure 3.6, can be expressed in the form:

$$\begin{aligned} D_1 &= (P_i - P_\infty)\, d\ell_1 \sin \eta_o \\ &= (P_i - P_\infty)\, dh_1 \end{aligned} \tag{8}$$

Where:

$$\sin \eta_o = \frac{dh_1}{d\ell_1}$$

P_i = Static pressure behind first oblique shock of lip.

dh_1 = Height of first element perpendicular to free stream flow.

η_o = External angle of cowl lip at first section.

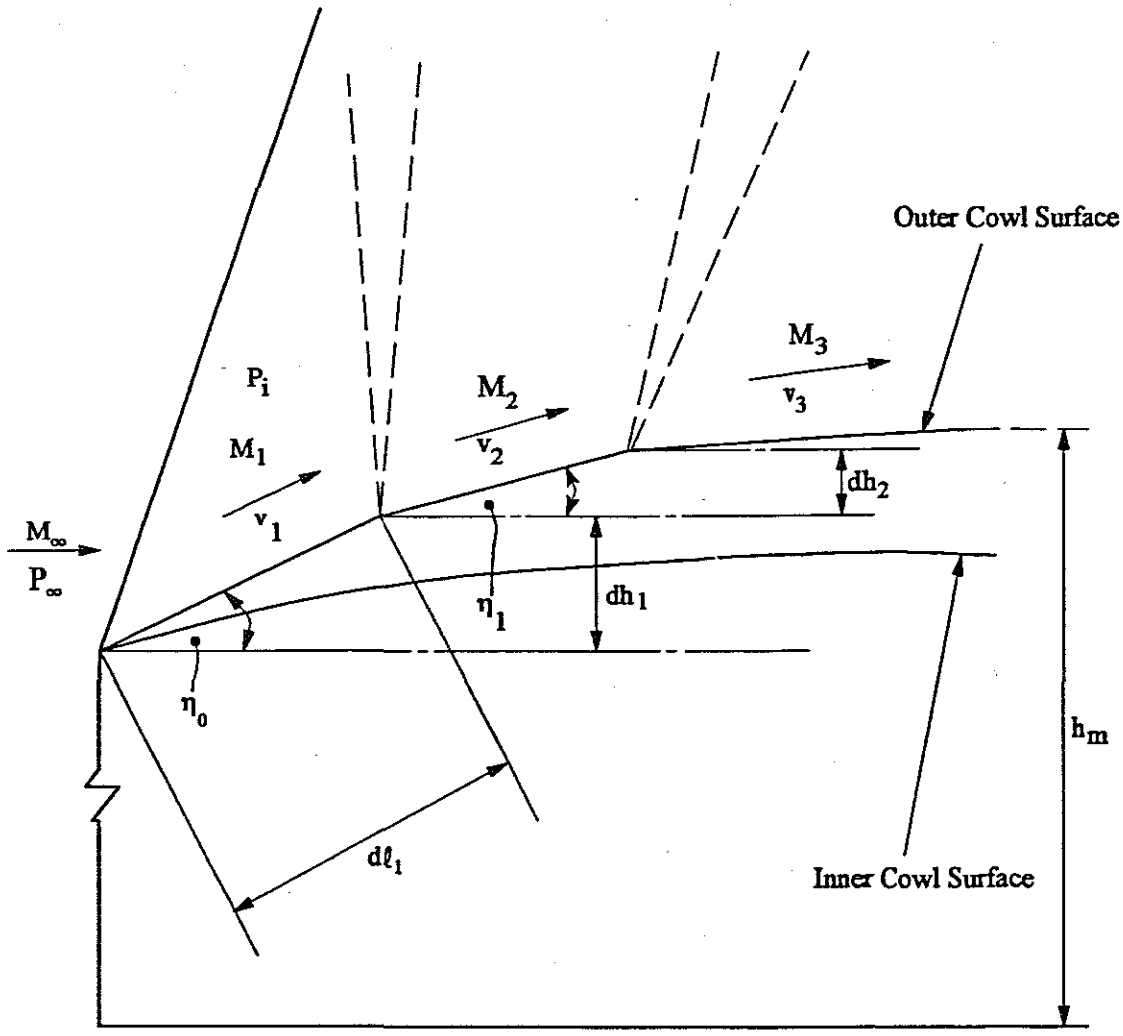

ℓ = Cowl length from lip to section where height is a maximum

$\ell = \ell_1 + \ell_2 + \ell_3$

h_m = Height of lip at maximum section

w = Width of lip section

FIGURE 3.6 : Cowl Pressure Distribution by Shock-Expansion Method (Seddon & Goldsmith 1985:257)

The drag on this element with a height, dh_1, can be expressed as a coefficient based on a vertical dimension, h_m, to obtain the non-dimensional form:

$$C_{dl} = \frac{D_1}{q_\infty h_m} \tag{9}$$

Where:

h_m = Height of element at maximum lip section.

It follows that the drag coefficient for the first element can be derived from equations 8 and 9:

$$C_{dl} = \frac{P_\infty}{q_\infty}\left(\frac{P_i}{P_\infty} - 1\right)\frac{dh_1}{h_m} \tag{10}$$

The drag coefficient for the first inclined section of the cowl lip based on a projected area can be expressed in the form:

$$C_{dl} = \frac{(P_i - P_\infty)h_1 w}{q_\infty A_m} \tag{11}$$

Where:

A_m = h_m x w = Cross-sectional area at maximum section of cowl.

w = Width of lip section.

h_1 = Height of first section perpendicular to free stream flow.

Using this equation the different inclined sections of the cowl lip must be approximated by flat surfaces in order to allow for real physical dimensions to be used.

The process can be repeated to determine the coefficient of drag for the second element with a length, $d\ell_2$, and an angle, η_1, taken from the second inclined surface as shown in Figure 3.6 resulting in:

$$D_2 = (P_{ii} - P_\infty)\, d\ell_2 \sin \eta_1$$
$$= (P_{ii} - P_\infty)\, dh_2 \qquad (12)$$

Where:

$$\sin \eta_1 = \frac{dh_2}{d\ell_2}$$

In coefficient form equation 12 can be expressed as:

$$C_{d2} = \frac{(P_{ii} - P_\infty)\, dh_2}{q_\infty\, h_m}$$

$$= \frac{P_\infty}{q_\infty}\left(\frac{P_{ii}}{P_i}\frac{P_i}{P_\infty} - 1\right)\frac{dh_2}{h_m} \qquad (13)$$

Where:

P_{ii} = Static pressure behind expansion wave.

A cowl with a curved profile can be divided up into straight line segments where drag calculations are performed for each individual segment. The total cowl wave pressure drag is then derived by adding up the drag values of all the individual segments.

An inlet, where only external compression of the air is required, has a cowl with an internal angle corresponding to the angle required for turning the flow into the axial direction of the inlet entry without internal compression. The external angle of the cowl is limited by the minimum thickness of material required for machining the profile.

It is clear that the first inclined section of the cowl external surface is the main contributor to the wave pressure drag because it has the largest angle opposing the flow. The choice of a small external angle for the first segment will result in a lower wave pressure drag, but the machinability and practical design considerations where a lip that is too long and thin for a given maximum height of the cowl section will restrict the design parameters. It is recommended by Seddon and Goldsmith (1985) that a minimum angle of 3° should be used

between the internal and external angles for machining purposes. In practice it is found that this results in a very sharp lip which is quite difficult to machine. Angles of 4° to 5,5° are found to be more realistic in terms of manufacturing specifications. It is recommended that the length, ℓ_1, of the first lip section be kept as short as possible in order to eliminate a very thick projected area, $w(\ell_1 \sin \eta_0)$, which is a term contributing to drag. The remaining lip external angles are chosen according to structural considerations where sufficient material thickness is required between the internal and external surfaces of the cowl duct.

The wave pressure drag associated with side plates will depend on the size and shape of these plates. The size and shape will usually be established experimentally according to the inlet performance for given sideslip (yaw) angles. The forward facing edges of the side plates must be chamfered on the outside to form leading edges which are as sharp as possible for the lowest possible drag.

3.2.3 Bleed Drag

The main objective in bleeding off internal air is to remove the low-energy boundary layer air before it is ingested into the inlet diffuser where it can cause separation and flow instability. The bleed air undergoes a loss in momentum when it is removed from the main stream and the resulting internal drag associated with this process is called bleed drag. This bleed drag is a function of the flow conditions inside the bleed duct where the flow is influenced by the internal shape of the duct, the area of the exit opening and the flow conditions (static pressure) outside the duct exit.

The most common method of taking bleed flow overboard is to take the mass flow through a duct system and dump it to atmosphere (during flight conditions) or to the tunnel test section (during wind-tunnel tests). The duct exit opening is chosen to allow the full flow entering through the entrance plane to pass through the bleed duct at a specific flight condition.

At subsonic free stream conditions the mass flow rate through the bleed duct is governed by the static pressure of the external flow at the duct exit. In this case it is not possible to

choke the exit due to an inadequate pressure ratio. A ratio of $P_o/P \geq 1{,}893$ is required for choking of the exit.

At supersonic flight speeds the exit will be choked with sufficient stagnation pressure recovery of the bleed air to achieve the required pressure ratio mentioned above.

The calculation of inlet bleed drag is based on the application of the momentum equation as discussed by Seddon and Goldsmith (1985). This is a general equation for different flow conditions through the bleed duct. The change in momentum between the entrance and exit stations of the bleed duct is expressed in momentum theorem form refering to Figure 3.7:

Momentum flux at entry = Momentum flux at exit + momentum loss due to internal flow distortions (drag component).

$$A_{B_\infty}\, \rho_\infty\, V_\infty^2 = \left[(P_{ex} - P_\infty)\, A_{ex} + A_{ex}\, \rho_{ex}\, V_{ex}^2\right] + D_{int} \tag{14}$$

But $$V^2 = \frac{2q}{\rho} \tag{15}$$

Substitution of equation 15 into equation 14 results in:

$$2q_\infty\, A_{B_\infty} = \left[(P_{ex} - P_\infty)\, A_{ex} + 2q_{ex}\, A_{ex}\right] + D_{int}$$

$$D_{int} = 2q_\infty\, A_{B_\infty} - \left[(P_{ex} - P_\infty) + 2q_{ex})\right]A_{ex} \tag{16}$$

Where:

A_{ex} = Bleed duct exit area

$A_{B\infty}$ = Free streamtube area captured by the bleed duct as shown in Figure 3.7

q = Dynamic pressure

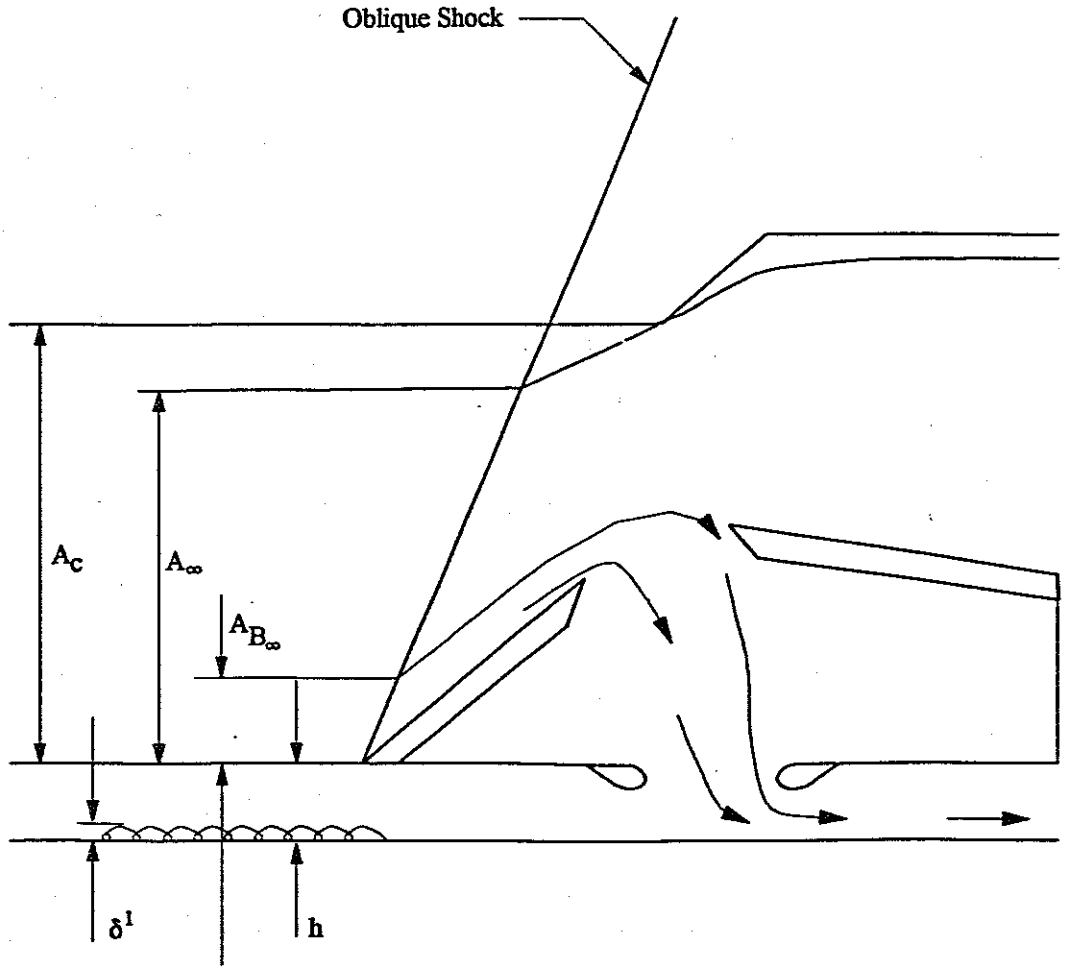

FIGURE 3.7 : Bleed Flow Terminology

P = Static pressure

∞ = Denotes free stream conditions

ρ = Air density

ex = Denotes conditions at duct exit

The above equation takes account of the pressure losses as well as the change in momentum caused by friction on the internal "wetted" surfaces of the duct.

From a system point of view it is more practical to define the bleed drag in terms of local conditions at the bleed entry plane resulting in the following expression:

$$D_{int} = \left[(P_\ell - P_\infty) + 2q_\ell \frac{\phi}{\phi_\ell}\right]A_{en} - \left[(P_{ex} - P_\infty) + 2q_{ex}\right]A_{ex} \qquad (17)$$

Where:

ℓ = Local conditions at the bleed entry

A_{en} = The bleed entry area normal to the flow

Φ/Φ_ℓ = Boundary layer momentum ratio

Different values of Φ/Φ_ℓ for a boundary layer with a standard velocity profile parameter n = 7 are obtained from Figure 3.8.

Where:

M_ℓ = Local Mach number at bleed entry

h/δ^1 = Inlet height ratio = $\frac{\text{Inlet diverter height}}{\text{Boundary layer thickness}}$

The velocity profile parameter, n, can be obtained from a power-law velocity distribution through the boundary layer from equation 4.1 (Seddon & Goldsmith 1985) :

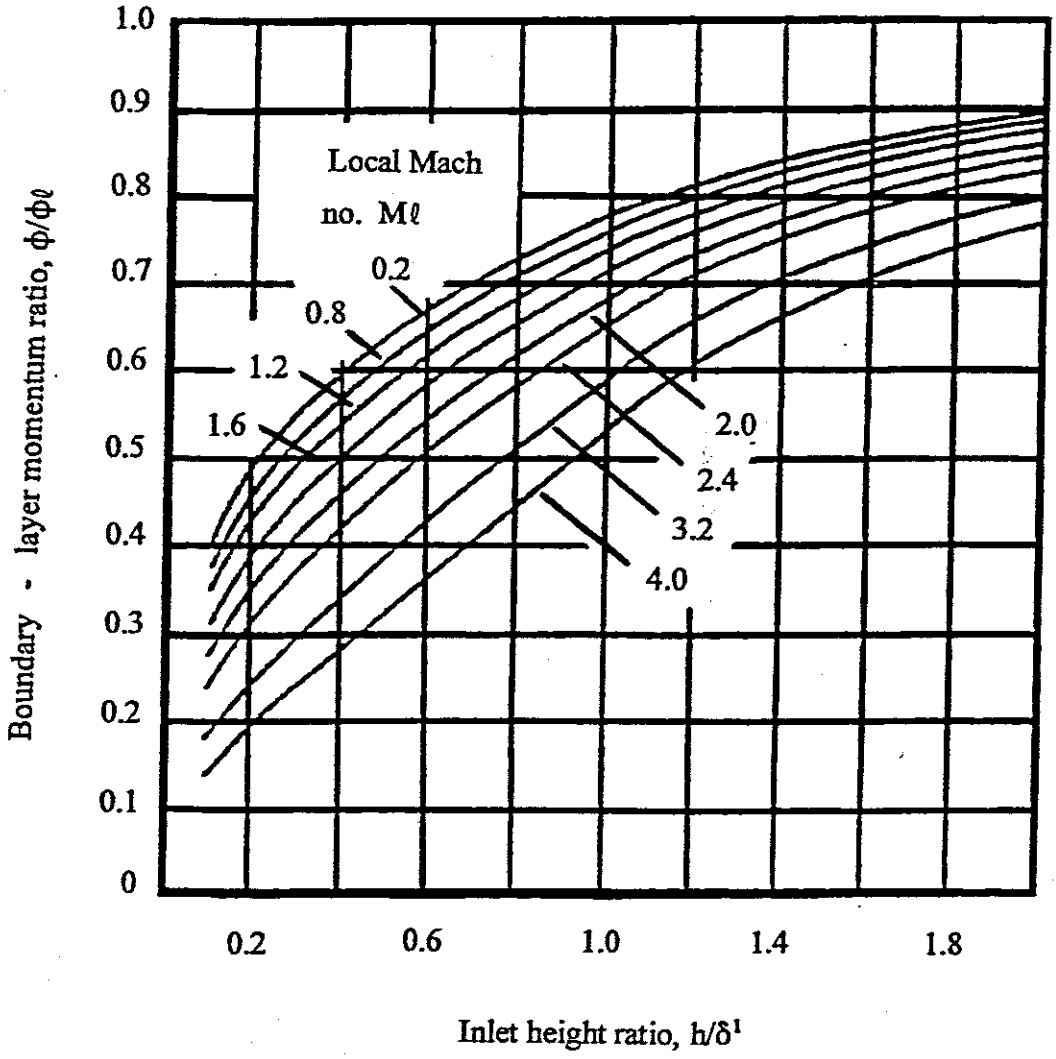

FIGURE 3.8 : Boundary Layer Momentum Ratios (Seddon & Goldsmith 1985:210) (Velocity Profile Parameter n = 7)

$$\frac{U}{U_t} = \left(\frac{y}{\delta}\right)^n \tag{18}$$

Where:

U = Streamwise velocity in boundary layer at a distance y from the surface.

U_t = Streamwise velocity at the edge of the boundary layer

δ^1 = Boundary layer thickness

Aerodynamic drag is normally expressed in coefficient form by dividing the drag force by the free stream dynamic pressure and a reference frontal area. From equation 16 it follows that:

$$C_d = \frac{D_{int}}{q_\infty A_c} = \left(\frac{2A_{B_\infty}}{A_c}\right) - \left[\left(\frac{P_{ex}}{P_\infty} - 1\right)\frac{P_\infty}{q_\infty} + \frac{2q_{ex}}{P_{ex}} \cdot \frac{P_{ex}}{P_\infty} \cdot \frac{P_\infty}{q_\infty}\right]\frac{A_{ex}}{A_c} \tag{19}$$

Where:

A_C = Main inlet capture area.

It should be noted that for a value of h/δ^1 greater than one, some of the flow outside the boundary layer is diverted into the bleed duct. This is uneconomical with a resulting increase in bleed drag without any improvement in the quality of flow entering the inlet.

3.2.4 Diverter Drag

A diverter can be described as an intermediate section between the inlet and the missile airframe allowing the inlet to stand off from a specific surface. The boundary layer approaching the inlet is diverted sideways and backwards into a channel away from the inlet opening. Wedge-shaped channel diverters, as shown in Figure 3.9, are commonly used on supersonic inlets for this purpose.

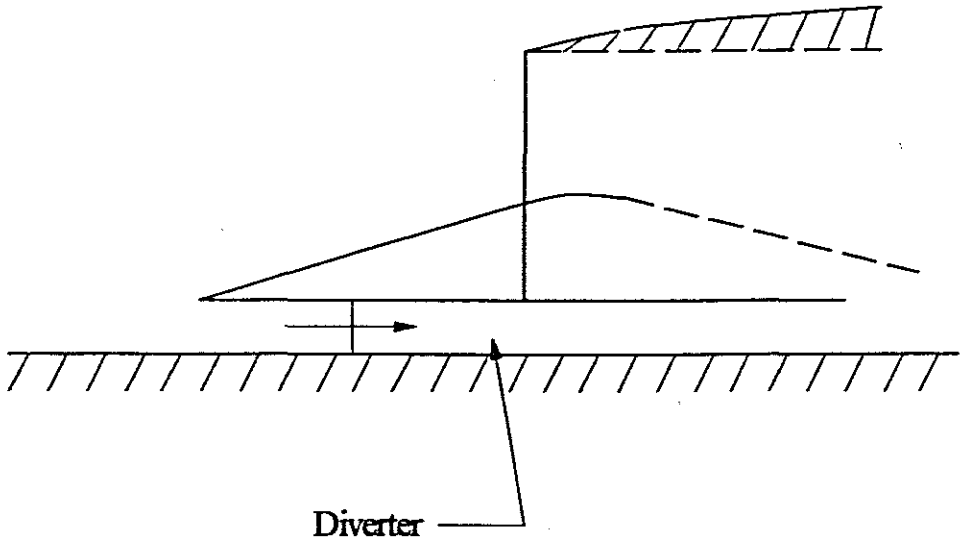

FIGURE 3.9 : Channel Diverter for Supersonic Inlet

Boundary layer problems generally increase with higher flight speeds. At supersonic speeds shock waves are encountered which drastically increase the boundary layer problem where it interacts with the flow on the surface of the missile airframe up-stream of the inlet entry. It is therefore recommended that provision must be made for a diverter under these flight conditions.

Careful consideration must be given to the desirability of installing a diverter, which is an additional piece of hardware on the missile airframe, to achieve a gain in pressure recovery. This gain, due to the scooping off of boundary layer air, is associated with a drag and mass penalty.

According to Jell and Ballinger (Seddon & Goldsmith 1985) the friction drag of a channel diverter can be derived from the flat plate skin friction for compressible flow based on the total wetted area inside the diverter channel.

The skin friction drag is derived by Hoerner (1965) and is based on the momentum loss of the boundary layer per unit time. The skin friction drag coefficient is found to be:

$$C_f = \frac{D_f}{q\, S_{wet}} \tag{20}$$

Where:

D_f = Friction drag

q = Dynamic pressure = $1/2\ \rho\ V^2$

S_{wet} = Wetted area of surface under consideration

Values for the skin friction drag coefficient as a function of Mach number are shown in Figure 3.10 for a laminar boundary layer in compressible fluid flow (Hoerner 1965:17-3). Skin friction is a function of viscosity due to the change in temperature within the boundary layer. This is a result of different streamwise velocities from the body surface to the edge of the boundary layer. The skin friction coefficient in Figure 3.10 is therefore expressed in terms of Reynolds number, R_t, based on a body length dimension. The coefficient, C_f,

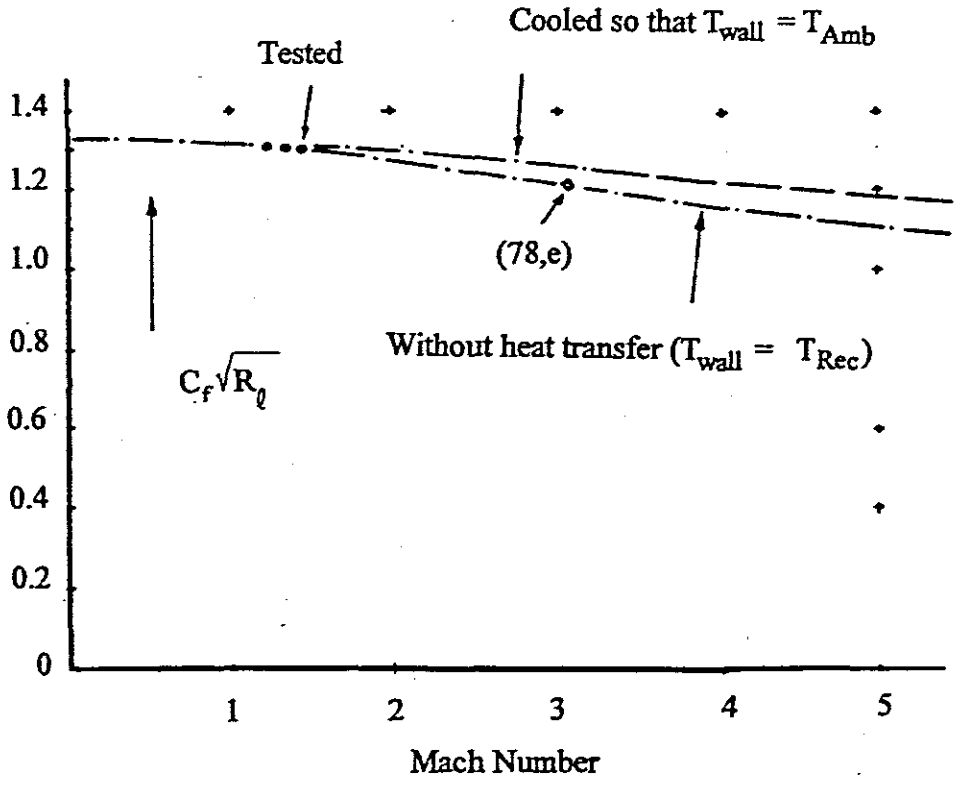

R_ℓ = Reynolds number based on a body length dimension

FIGURE 3.10 : Mean-total Laminar Skin Friction Parameters in Terms of Reynolds Number (Hoerner 1965:17-3)

can now be calculated for a known Mach number and corresponding Reynolds number.

In a practical case, whether the boundary layer is laminar or not, depends on the conditions upstream of the diverter. In a missile application, where the inlet/diverter is normally situated a few diameters aft of the missile nose and where shock waves are encountered when flying at supersonic speeds, it is most likely to have turbulent flow approaching the diverter. This will cause a much higher friction drag than laminar flow because in the case of turbulent flow, fluctuating velocity components transversely and parallel to the main stream are encountered, causing a change in momentum with a resulting increase in friction drag.

Tests carried out by Schultz-Grunow (Hoerner 1965) on velocity distributions on a flat wall resulted in the following equation for turbulent skin friction drag coefficient in compressible flow:

$$C_f = 0{,}427 / (\log R_t - 0{,}407)^{2{,}64} \qquad (21)$$

Tests on smooth plates in wind-tunnels and towed water tanks show that the above theoretical equation renders adequate values for the drag coefficient, C_f, over a wide range of Reynolds numbers, $R_t = 10^5$ to 10^9, which comes close to Schoenherr's line as shown by Hoerner (1965:2-5). Since the Reynolds number Re, is a function of the Mach number the effect of Mach number is explained by the Sutherland formula (Hattingh 1977) :

$$Re = 47772\ [P\ M\ D / T^2]\ (T + 114)$$

$$P = P_0 / \left(1 + \frac{\gamma - 1}{2} M^2\right)^{\frac{\gamma + 1}{2(\gamma - 1)}}$$

$$T = T_0 / \left(1 + \frac{\gamma - 1}{2} M^2\right)$$

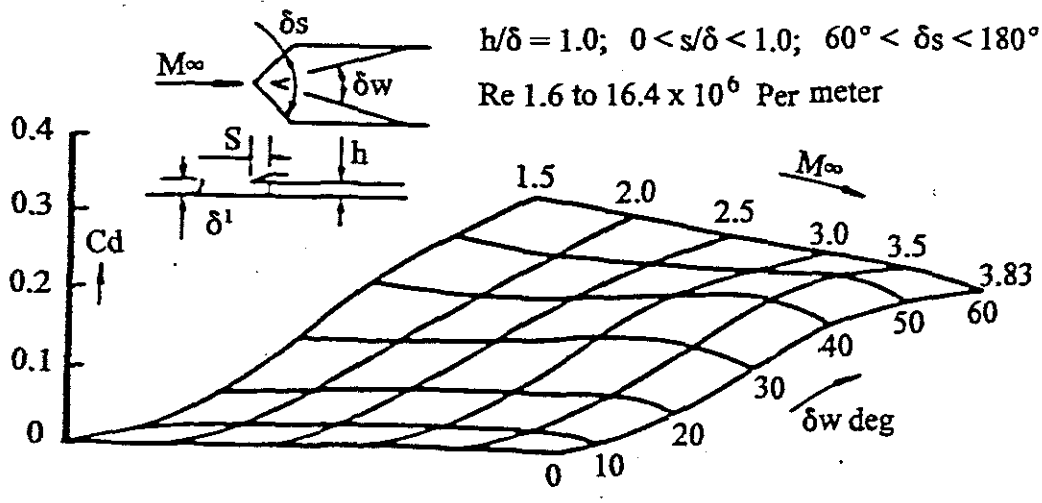

FIGURE 3.11 : Wave Drag of a Wedge Diverter (Seddon & Goldsmith 1985:215)

The wave drag for a diverter with a specific geometrical shape and drag coefficient corresponding to a selected Mach number from Figure 3.11 can now be calculated.

During the integration of the inlet with the "flight vehicle" it is very important to establish the boundary layer thickness of the flow on the vehicle airframe at the inlet entry plane very accurately.

The diverter height must be set to a value which is fractionally more than that required to remove only the low energy boundary layer flow. Bendot, Heins and Piercy (1984) state that a significant improvement in stagnation pressure recovery and flow stability can be achieved with a diverter height which is just greater than the boundary layer thickness.

Scooping off too much of the high energy free stream flow will result in a drag penalty without improvement in the stagnation pressure recovery. It is therefore generally accepted that the optimum height for a specific diverter has to be experimentally determined in a wind-tunnel and not only taken as described above by Bendot, Heins and Piercy (1984) because inlet location, yaw and side slip angles have a significant influence on the boundary layer thickness.

3.3 DETERMINATION OF COEFFICIENT

A better understanding of the inlet drag phenomenon is obtained when calculations are performed for actual flight conditions. The drag of each inlet component, including the boundary layer diverter, is calculated separately and added up to give the total drag experienced by the inlet in flight.

A two-dimensional supersonic inlet with two external compression wedges, on a missile flying at M = 2,0 at sea level, is used as an example in the calculations. The aim of this study is to obtain an overall drag coefficient for this specific inlet based on frontal projected area (61,02 mm x 56,4 mm) and free stream dynamic pressure. The coefficient of drag for the diverter is also given as a separate figure because it is seen as an intermediate section between the inlet

diverter is also given as a separate figure because it is seen as an intermediate section between the inlet and airframe and can vary in size and shape for a particular inlet with a specific geometric shape.

The geometrical shape of the full-scale porous inlet is shown in Figure 3.12. Drag calculations based on control volume, V_C, are conducted as follows for each individual component.

3.3.1 Pre-entry or Additive Drag

It is assumed that the inlet operates at a Mach number of M = 2,0 which is below the design point where M_{des} = 2,2. At this condition the inlet is operating with the oblique shock in front of the cowl lip and pre-entry drag is encountered. For maximum flow conditions, as defined in section 3.2.1.1, the pre-entry drag for a double-wedge compression surface can be determined from equation 4:

$$(D_{pre})_a = (P_1 - P_\infty)\left[A_1 - (A_\infty)_{max}\right] + (P_2 - P_\infty)(A_c - A_1) \qquad (23)$$

Where:

P_1 = Static pressure behind first oblique shock

P_2 = Static pressure behind second oblique shock

P_∞ = Free stream static pressure

A_∞ = Streamtube area

A_c = Capture area

A_1 = Area enclosed by the *maximum-flow streamtube* at its intersection with the second oblique shock.

The values of P_∞ = 101,33 kPa (static pressure at sea level), P_1 = 164,88 kPa and P_2 = 244,91 kPa are obtained from Table 3.1 for M = 2,0.

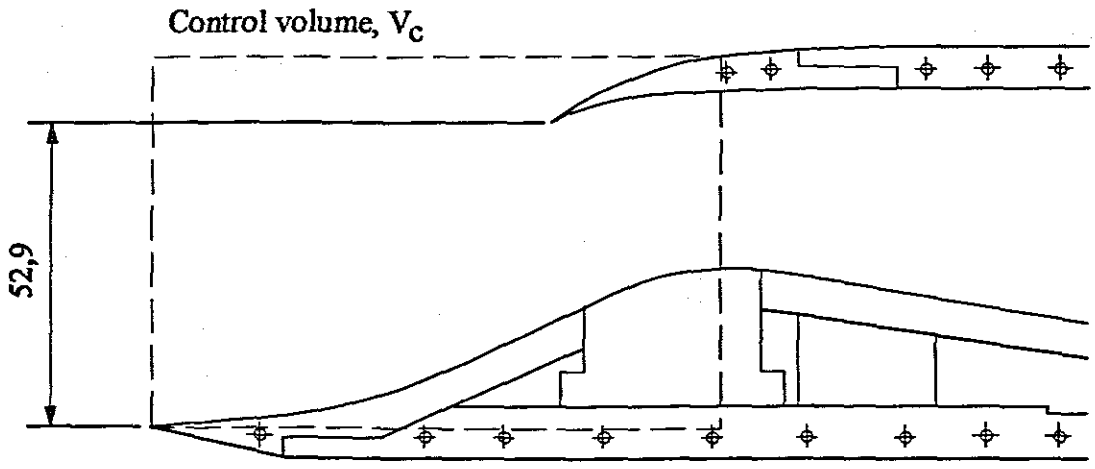

Sectional View

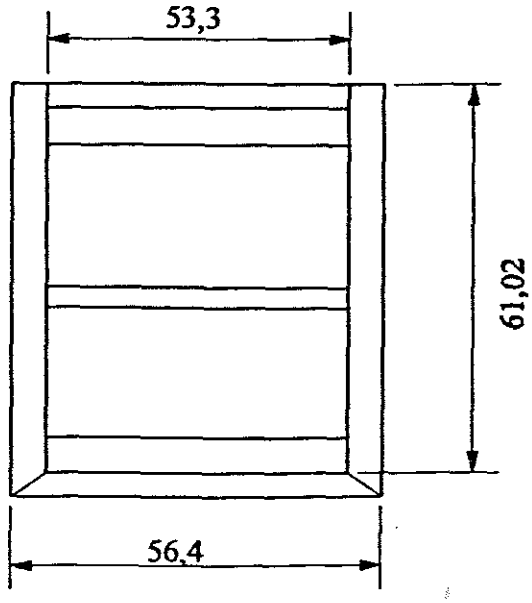

Frontal View

FIGURE 3.12 : Geometric Shape of Full-scale Porous Inlet

A graphical display of the streamtube areas is shown in Figure 3.13. The values of A_1 = 48,36 mm, A_c = 52,9 mm and A_∞ = 47,36 mm are found from Table 3.1 and the width of the capture opening = 53,3 mm from Figure 3.12.

Substituting all the relevant information into equation 23 yields the value of the pre-entry drag:

$$(D_{pre})_a = (164,88 - 101,33)10^3\,[(48,36 - 47,36)53,3]\,10^{-6} + (244,91 - 101,33)10^3\,[(52,9 - 48,36)53,3]\,10^{-6} = 38,13\ N$$

The pre-entry drag for flight Mach numbers = 1,8; 2,2; 2,3 and 2,4 are calculated in a similar manner and the results are depicted in Table 3.2. For a better understanding of these values, a graph depicting the results are shown in Figure 3.14, where a decrease in drag with an increase in Mach number is clearly evident. This is caused by the fact that a decrease in pre-entry drag is encountered with the oblique shocks focussing closer and closer to the cowl lip as the Mach number increases to a point where the shocks fall at or inside the cowl lip.

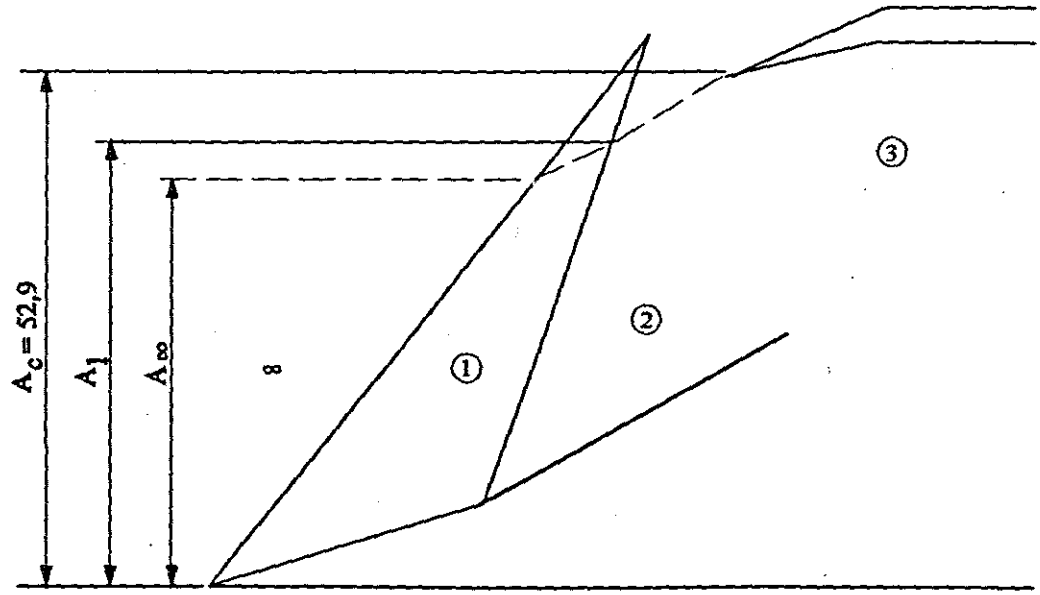

Full-scale Porous Model

FIGURE 3.13 : Streamtube Areas at below Design Mach Number

TABLE 3.1: Air Flow Properties at Different Free Stream Mach Numbers for Atmospheric Conditions at Sea Level (Ref. Appendix A)

	M = 1,8	M = 2,0	M = 2,2	M = 2,3	M = 2,4
Number of wedges = 2 Wedge angles : δ_1 = 9° δ_2 = 8°					
P_∞	101,33 kPa	101,33 kPa	101,33 kPa	101,33 kPa	101,33 kPa
$P_{0\infty}$	582,22 kPa	792,85 kPa	1083,49 kPa	1267,06 kPa	1481,45 kPa
q_∞	229,82 kPa	283,72 kPa	343,31 kPa	375,22 kPa	408,56 kPa
Full mass flow, $\dot{m}_\infty$	2,12 kg/s	2,35 kg/s	2,59 kg/s	2,70 kg/s	2,82 kg/s
A_c	52,9 mm	52,9 mm	52,9 mm	52,9 mm	52,9 mm
R_e	42 x 10^6/m	46 x 10^6/m	51 x 10^6/m	53 x 10^6/m	56 x 10^6/m
Wedge No.1 δ_1 = 9°					
M_1	1,49	1,67	1,85	1,94	2,03
P_1	159,07 kPa	164,88 kPa	170,79 kPa	173,78 kPa	176,80 kPa
P_{01}	575,56 kPa	777,93 kPa	1059,54 kPa	1238,78 kPa	1449,51 kPa
Wedge No.2 δ_2 = 8°					
M_2	1,20	1,39	1,57	1,65	1,76
P_2	236,28 kPa	244,91 kPa	258,46 kPa	267,86 kPa	267,55 kPa
P_{02}	572,97 kPa	768,49 kPa	1050,95 kPa	1226,49 kPa	1446,31 kPa
Mass flow captured, $\dot{m}_c$	1,74 kg/s	2,08 kg/s	2,46 kg/s	2,66 kg/s (2)	(1) 2,84 kg/s
A_∞	43,97 mm	47,36 mm	50,11 mm	52,6 mm	-
A_1	45,49 mm	48,36 mm	50,89 mm	52,7 mm	-
After Normal Shock					
M_3	0,84	0,74	0,68	0,65	0,63
P_3	357,56 kPa	511,23 kPa	700,17 kPa	806,15 kPa	922,31 kPa
P_{03}	567,56 kPa	735,51 kPa	945,22 kPa	1070,83 kPa	1205,00 kPa

NOTE 1 : $\dot{m}_c > \dot{m}_\infty$ because oblique shocks fall inside cowl lip.

NOTE 2 : $\dot{m}_c \approx \dot{m}_\infty$ because oblique shocks fall on cowl lip.

TABLE 3.2 Predicted Pre-entry Drag at Different Flight Mach Numbers

Mach No.	m_R	D_{pre} (Newton)	Operating Modes
1,8	0,82	57,98	Below design Mach No.
2,0	0,89	38,13	Below design Mach No.
2,2	0,95	19,72	At design Mach No. with oblique shocks focussing just in front of cowl lip
2,3	0,99	2,16	At Mach No. where oblique shocks focus on cowl lip (S.O.L.)
2,4	1,0	0	Above design Mach No. with oblique shocks focussing inside cowl lip

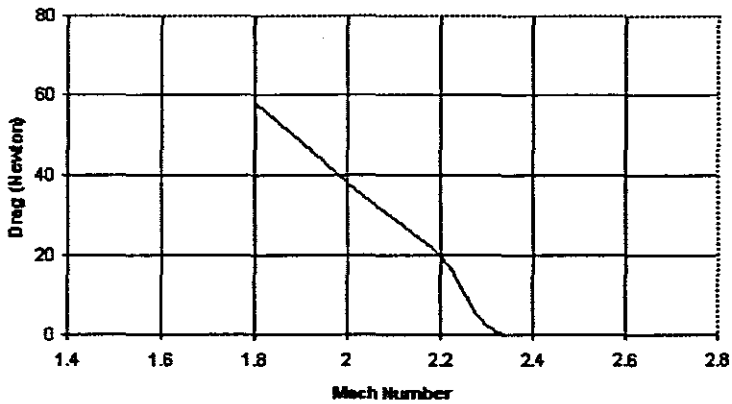

FIGURE 3.14 : Predicted Pre-entry Drag for Full-scale Porous Model

3.3.2 Spillage Drag

The spillage drag for an inlet operating subcritically is determined from equation 6:

$$D_{spill} = (P_3 - P_\infty)\ (A_c - A_\infty) - (D_{pre})_a$$

Where:

P_3 = Static pressure behind normal shock as shown in Figure 3.15.

Due to a lack of tunnel test data at subcritical flow conditions, the data required is taken from the theoretical flow dynamic calculations given in Table 3.1.

For M = 2,0 the following data is obtained from this table:

$\dot{m}_\infty$ = 2,35 kg/s = Mass flow based on capture area, A_c (i.e. full mass flow)

$\dot{m}_c$ = 2,08 kg/s = Mass flow based on streamtube area, A_∞ (i.e. actual mass flow captured)

P_∞ = 101,33 kPa

P_3 = 511,23 kPa

A_c = 52,9 mm

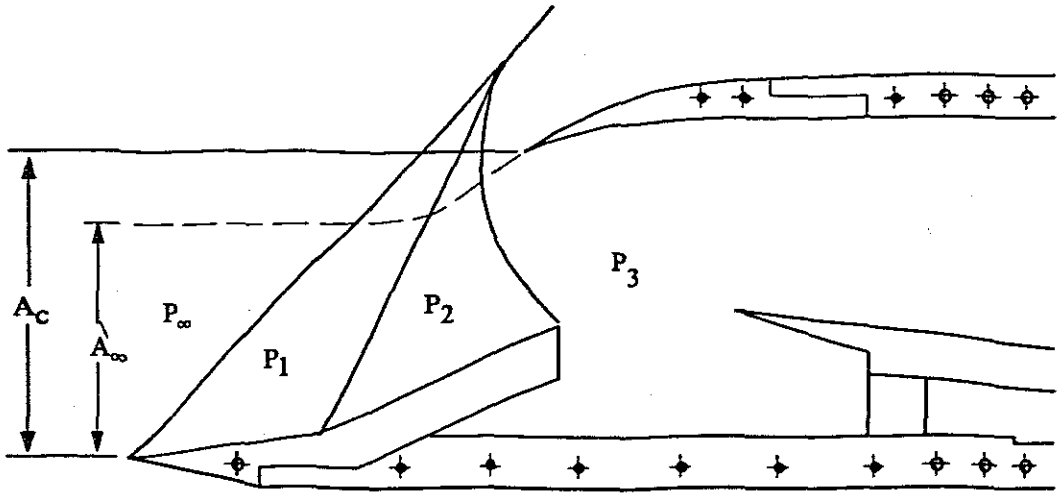

FIGURE 3.15: Inlet Operating Subcritically Below Design Mach Number

Spillage drag is based on mass flow entering the inlet before bleed mass flow is dumped. By closing the exit opening to obtain subcritical operation, the excess air is spilled around the cowl lip resulting in different percentages of spillage, eg. 5% , 10% , 20% , 30% , and 40%.

Assuming a 5 % spillage results in:

$\dot{m}_{spill}$ = 2,08 x 5/100 = 0,10 kg/s

and $\dot{m}_{\infty}$` = 2,08 - 0,10

= 1,98 = actual mass flow entering inlet duct with inlet spilling.

The new or actual streamtube area, as shown in Figure 3.15, becomes:

$$A_{\infty}` = 52,9 \; x \; \frac{1,98}{2,35}$$

= 44,57 mm per unit width

for $m_R = \frac{1,98}{2,35}$

= 0,84

Substituting all the relevant values into equation 6 results in the value of the spillage drag for a 5 % spillage:

$$D_{spill} = (511,23 - 101,33)\ 10^3\ [(52,9 - 44,57)\ 53,3]\ 10^{-6} - 38,13$$

= 143,86 N

The results of the spillage drag for other spillage ratios are calculated in a similar manner and depicted in Table 3.3.

TABLE 3.3 Predicted Spillage Drag at Different Operating Modes

% Spillage	M = 1,8		M = 2,0		M = 2,2		M = 2,3		M = 2,4	
	m_R	D_{spill}	m_R	D_{spill}	m_R	D_{spill}	m_R	D_{spill}	m_R	D_{spill}
5	0,78	102,22 N	0,84	143,86 N	0,90	143,38 N	0,94	122,94 N	0,95	114,21 N
10	0,74	129,39 N	0,80	197,82 N	0,85	227,97 N	0,89	225,87 N	0,91	213,54 N
20	0,66	190,85 N	0,71	301,16 N	0,76	384,36 N	0,79	417,46 N	0,80	451,58 N
30	0,58	248,76 N	0,62	399,48 N	0,66	547,47 N	0,69	616,19 N	0,71	681,32 N
40	0,49	310,08 N	0,53	502,82 N	0,57	703,86 N	0,59	807,41 N	0,60	919,36 N

The above-mentioned results are graphically displayed in Figure 3.16. An increase in spillage drag with an increase in spill rate as well as an increase in Mach number is clearly shown. A high Mach number before the normal shock causes a big drop in the value of the Mach number behind the normal shock with inlet spilling, resulting in a high static pressure acting across the projected area.

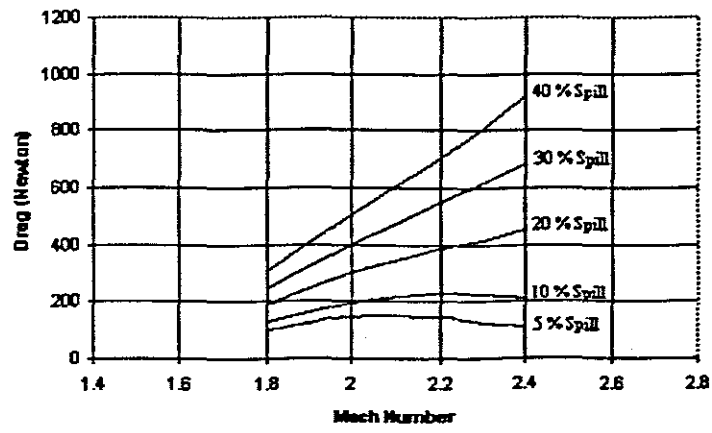

FIGURE 3.16 : Predicted Spillage Drag for Full-scale Porous Model

3.3.3 Cowl Drag

3.3.3.1 Wave Pressure Drag

The cowl lip is divided into two inclined flat surfaces or sections as shown in Figure 3.17. The drag for each section is calculated individually because the flow conditions differ from the one surface to the other.

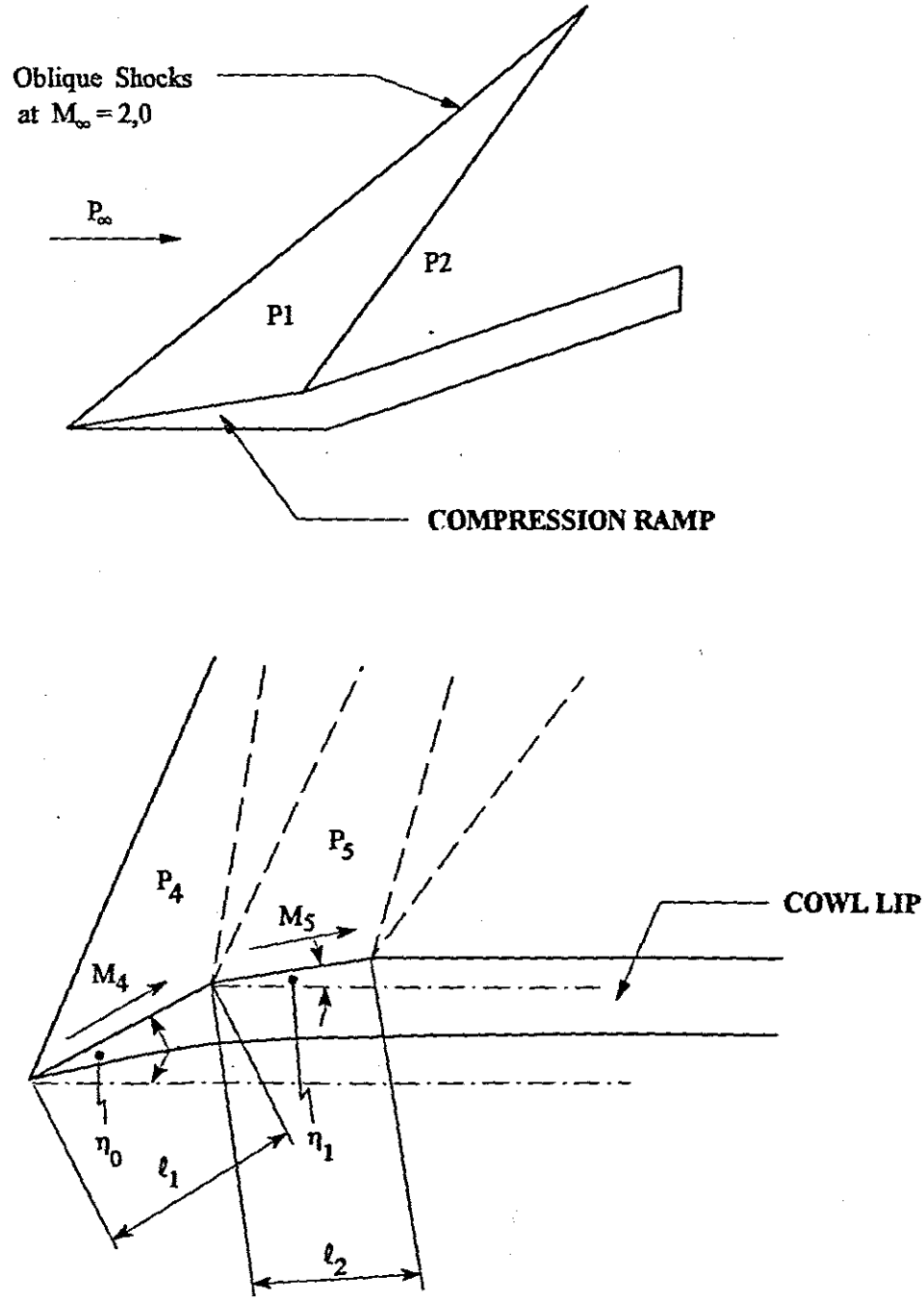

FIGURE 3.17 : Cowl Pressure Distribution

(i) Without Inlet Spilling

Equation 8 is used in calculating the wave pressure drag of the first section:

$$D_1 = (P_i - P_\infty)\, d\ell_1 \sin \eta_o$$

Where:

P_i = Refers to static pressure, P_4, behind first oblique shock of cowl lip as shown in Figure 3.17

$d\ell_1$ = Length of first element.

η_o = External angle of cowl lip at first section.

For a free stream Mach number of 2,0 the static pressure and Mach number behind the second oblique shock of the compression ramp is obtained from Table 3.1 where P_2 = 244,91 kPa and M_2 = 1,39 respectively.

An oblique shock wave is formed at the leading edge of the cowl lip and a Prandtl - Meyer expansion fan at the top corner as shown in Figure 3.18.

From Table C.12 (Zucrow & Hoffman 1976:744) for M_2 = 1,39, $\delta = 5°$ and γ = 1,4 the shock wave angle is found to be $\epsilon = 53{,}65°$. Equation 7.99 (Zucrow & Hoffman 1976:368) yields the value for:

$$M_2` = M_2 \sin\epsilon$$

Where $M_2`$ refers to the normal velocity component in front of the oblique shock wave.

$$M_2` = 1{,}39 \sin (53{,}65°)$$
$$= 1{,}12$$

From Table C.11 (Zucrow & Hoffman 1976:736) for $M_2` = 1{,}12$ and $\gamma$ = 1,4 the values of $M_4` = 0{,}89656$ and P_4/P_2 = 1,2968 are obtained resulting in:

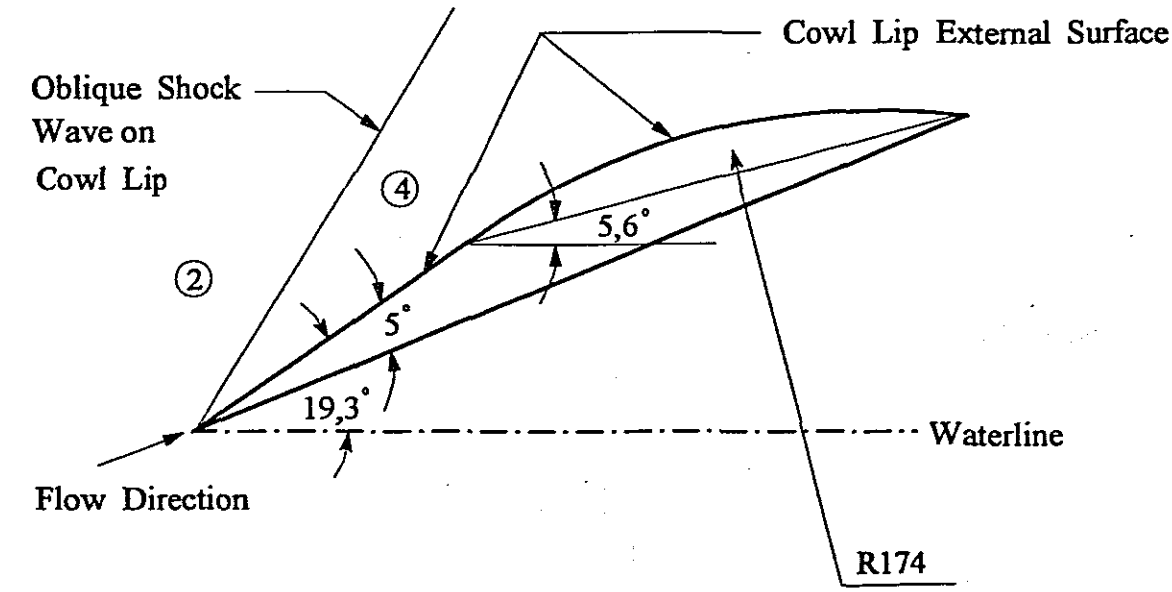

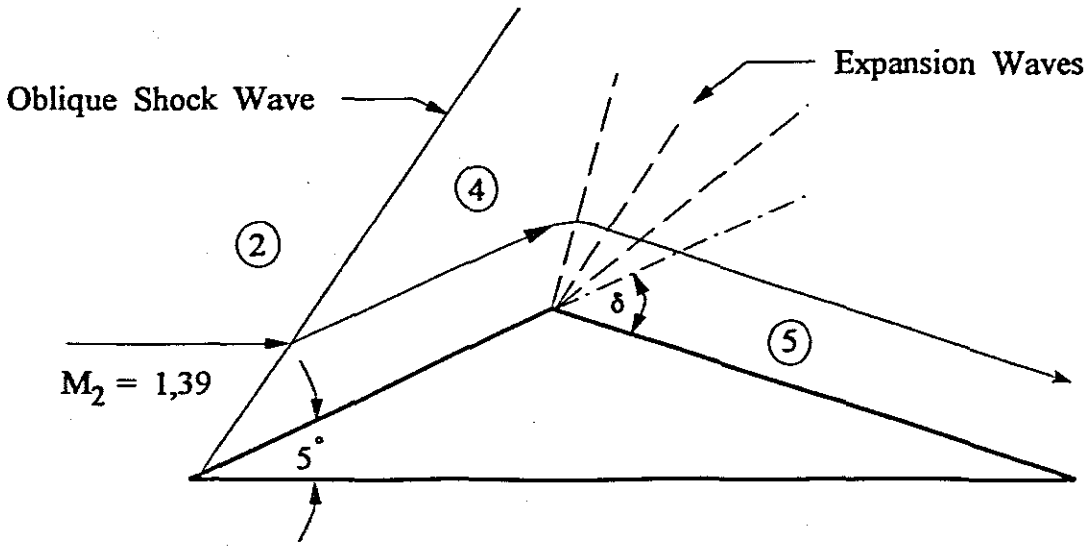

FIGURE 3.18 : Geometry of Cowl Lip External Surface for Full-scale Porous Model

$P_4 = 1,2968 \times 244,91$

$= 317,60$ kPa

Where $M_4`$ refers to the normal velocity component behind the oblique shock wave.

Equation 7.100 (Zucrow & Hoffman 1976:368) yields the value for:

$M_4 = M_4`/\sin(\epsilon - \delta)$

$= 0,89656/\sin(53,65° - 5°)$

$= 1,19$

The flow deflection angle, δ, for the Prandtl-Meyer expansion fan, as shown in Figure 3.18, is a 13,7° convex corner. From Table C.13 (Zucrow & Hoffman 1976:749) for $M_4 = 1,19$ and $\gamma = 1,4$ the Prandtl-Meyer angle $\nu_4 = 3,32°$.

Thus $\nu_5 = \nu_4 + \delta$

$= 3,32° + 13,7°$

$= 17,02°$

Table C.13 (Zucrow & Hoffman 1976:749) yields the value for the Mach number behind the expansion fan, $M_5 = 1,67$, for values of $\nu_5 = 17,02°$ and $\gamma = 1,4$.

From Table C.6 (Zucrow & Hoffman 1976:709) for $M_4 = 1,19$ and $M_5 = 1,67$ the corresponding values of $P_4/P_{04} = 0,41778$ and $P_5/P_{05} = 0,21195$ are found.

Where P_0 denotes stagnation pressure and P_5 = static pressure behind the expansion fan. Since the expansion is taken to be isentropic $P_{04} = P_{05}$ and :

$$P_5 = P_4 \left(\frac{P_5}{P_{05}}\right)\left(\frac{P_{04}}{P_4}\right)$$

$$= \frac{317,60\ (0,21195)}{0,41778}$$

$= 161,13\ kPa$

The flow properties of air for atmospheric conditions at sea level are shown in Table 3.4 for different Mach numbers. The drag on the first inclined section can now be calculated from equation 8 :

$$D_1 = (P_4 - P_\infty)\, d\ell_1 \sin \eta_0$$

TABLE 3.4 : Air Flow Properties in Front of Cowl Lip for Atmospheric Conditions at Sea Level

	M = 1,8	M = 2,0	M = 2,2	M = 2,3	M = 2,4
M_2	1,20	1,39	1,57	1,65	1,76
P_2	236,28 kPa	244,91 kPa	258,46 kPa	267,86 kPa	267,55 kPa
M_4	0,84 (1)	1,19	1,40	1,47	1,58
P_4	357,56 kPa	317,60 kPa	328,45 kPa	347,36 kPa	346,96 kPa
M_5	0,84	1,67	1,87	1,94	2,06
P_5	357,56 kPa(2)	161,13 kPa	163,38 kPa	171,30 kPa	166,66 kPa
R_e	42 x 10^6/m	46 x 10^6/m	51 x 10^6/m	53 x 10^6/m	56 x 10^6/m
C_f	0,0040	0,0039	0,0038	0,0038	0,0037

Note 1: For a flow deflection angle of $\delta = 5°$, the oblique shock wave becomes detached from the cowl lip and acts like a normal shock wave (Zucrow & Hoffmann 1976:364).

Note 2: The flow is subsonic behind the detached shock and is turned through a smooth convex corner without any losses or change in pressure.

Where:

P_4 = 317,60 kPa

P_∞ = 101,33 kPa

ℓ_1 = 14,9 mm (Ref. Table A.1 Appendix A)

η_0 = 19,3°

Substituting the relevant values in the above equation yields the value for wave pressure drag per unit width:

D_1 = (317,60 - 101,33) 14,9 sin 19,3°

= (216,27 kPa) 4,92 mm per unit width.

But width of lip section = 56,4 mm

$D_1 = (216,27 \times 10^3)(4,92 \times 56,4 \times 10^{-6})$

$= 60,01$ N

The drag on the second flat surface of the lip can be determined in a similar way where:

$D_2 = (P_5 - P_\infty)\, d\ell_2 \sin \eta_1$

and $P_5 = 161,13$ kPa

$\ell_2 = 32,8$ mm (Ref. Table A.1 Appendix A)

$\eta_1 = 5,6°$

Substituting the relevant values in the above equation yields :

$D_2 = (161,13 - 101,33)\, 32,8 \sin 5,6°$

(59,8 kPa) 3,20 mm per unit width

But width of lip section = 56,4 mm

$D_2 = (59,8 \times 10^3)(3,20 \times 56,4 \times 10^{-6})$

$= 10,79$ N

The total wave pressure drag acting on the cowl lip thus has a value of $D_p = 70,80$ N.

(ii) With Inlet Spilling

With the inlet spilling the normal shock is pushed out in front of the cowl lip and the static pressure acting on the lip section refers to the subsonic pressure values for P_3 in Table 3.1.

The pressure P_1 in equation 8 can be substituted by P_3, the pressure behind the normal shock, and the wave pressure drag per unit width is expressed as :

$D_{pw} = (P_3 - P_\infty)[d\ell_1 \sin \eta_0 + d\ell_2 \sin \eta_1]$

Substituting the relevant values for $\ell_1 = 14,9$ mm, $\ell_2 = 32,8$ mm, $\eta_0 = 19,3°$, $\eta_1 = 5,6°$

and P_3 = 511,23 kPa at a free stream Mach number = 2,0 yields:

D_{pw} = (511,23 - 101,33) 10^3 [14,9 sin 19,3° + 32,8 sin 5,6°]

= (409,90 kPa) 8,12 mm per unit width

Width of lip section = 56,4 mm

D_p = (409,90 x 10^3)(8,12 x 56,4)10^{-6}

= 187,72 N

In a similar manner the wave pressure drag can be calculated for different flight Mach numbers and the predicted results are shown in Table 3.5.

3.3.3.2 Skin Friction Drag

The Reynolds number for sea level conditions (height = 0) at M = 2,0 is found from Table 3.1 where Re = 46 x 10^6/m. The Reynolds number, based on a body length dimension, is determined for a cowl lip with a length of 0,047 m resulting in:

R_f = 0,047 (46,7 x 10^6)

= 2,16 x 10^6

Assuming compressible flow in the turbulent region, the skin friction drag coefficient can be determined from equation 21:

C_f = 0,427/(log R_f - 0,407)^{2,64}

= 0,427/(log 2,16 x 10^6 - 0,407)^{2,64}

= 0,0039

From the dimensions shown in Figure 3.19 the wetted area of the cowl lip can be calculated for a lip section with internal width = 53,3 mm and external width = 56,4 mm:

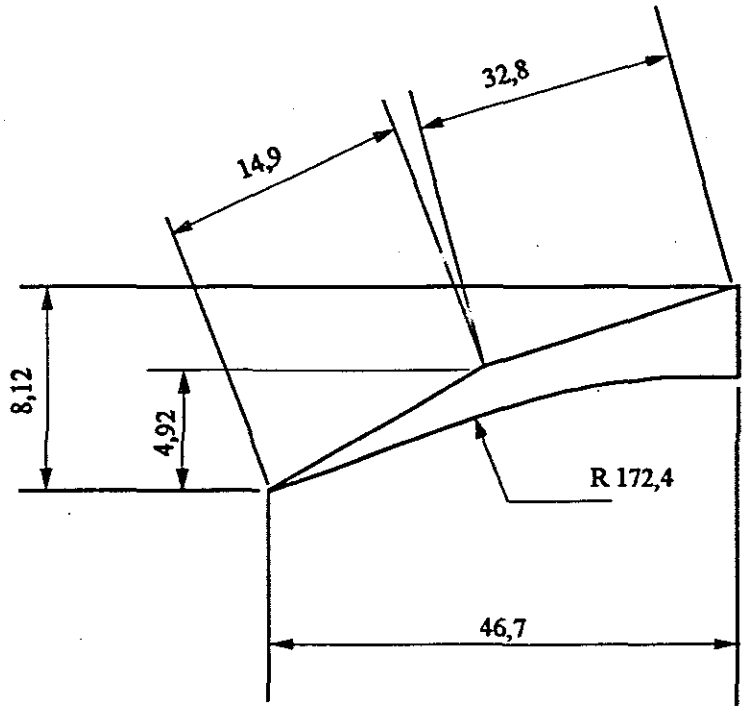

FIGURE 3.19 : Side View of Cowl Lip for Full-scale Porous Model

$S_{wet.in}$ = 53,3 x 46,7 x 10^{-6} m^2

= 2489 x 10^{-6} m^2

$S_{wet.ex}$ = 56,4 (14,9 + 32,8) 10^{-6}

= 2690 x 10^{-6} m^2

S_{wet} = (2489 + 2690) 10^{-6} m^2

= 5179 x 10^{-6} m^2

The skin friction drag, based on free stream dynamic pressure, can now be calculated from equation 20 where q_∞ = 283,72 kPa for M = 2,0 (Ref Table 3.1).

D_f = C_f S_{wet} q_∞

= 0,0039 x 5179 x 10^{-6} x 283,72 x 10^3

= 5,73 N

The value is not very significant when compared to a value of 70,80 N for the wave pressure drag. The predicted values for the different drag components acting on the cowl lip at different Mach numbers are depicted in Table 3.5 and Figure 3.20.

TABLE 3.5 Predicted Cowl Drag at Different Operating Modes

	WITHOUT SPILLAGE (CRITICAL)				
	M = 1,8	**M = 2,0**	**M = 2,2**	**M = 2,3**	**M = 2,4**
m_R	0,82	0,89	0,95	0,99	1,0
D_1	71,10 N	60,01 N	63,02 N	68,27 N	68,16 N
D_2	46,24 N	10,79 N	11,20 N	12,63 N	11,79 N
D_n	117,34 N*	70,80 N	74,22 N	80,90 N	79,95 N
D_f	4,76 N*	5,73 N	6,76 N	7,38 N	7,83 N
D_{lip}	122,10 N*	75,65 N	80,98 N	88,28 N	87,78 N
WITH SPILLAGE (Subcritical)					
m_R	0,49 to 0,78	0,53 to 0,84	0,57 to 0,90	0,59 to 0,94	0,60 to 0,95
D_n	117,34 N*	187,72 N	274,25 N	322,79 N	375,98 N
D_f	4,76 N*	5,73 N	6,76 N	7,38 N	7,83 N
D_{lip}	122,10 N*	193,45 N	281,01 N	330,17 N	383,81 N

* See note 2 below Table 3.4.

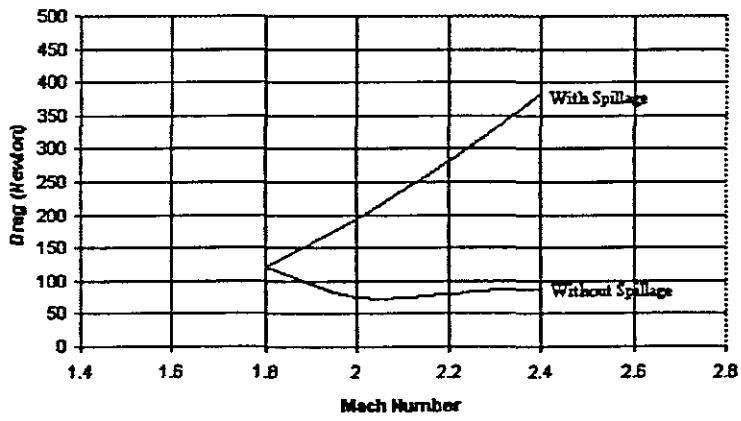

FIGURE 3.20 : Predicted Cowl Drag for Full-scale Porous Model

3.3.4 Bleed Drag

The method applied in this particular case is to bleed low energy boundary layer air from the compression surface through a throat bleeding system with the flow in the exit opening of the bleed duct choked.

The internal drag caused by bleeding off boundary layer air is represented by equation 16:

$$D_{int} = 2q_{\infty} A_{B\infty} - \left[(P_{ex} - P_{\infty}) + 2q_{ex}\right] A_{ex}$$

Where:

A_{ex} = Bleed duct exit area

$A_{B\infty}$ = Free streamtube area captured by the bleed duct per unit width

q_{∞} = Free stream dynamic pressure

q_{ex} = Dynamic pressure at bleed duct exit

P_{ex} = Static pressure at duct exit

Width of bleed entry opening = 90 mm

From wind-tunnel test results of an inlet model with similar geometry (Stockenström 1990), a bleed flow ratio of 8 % based on the mass flow entering through the streamtube area A_∞, was measured. The value for $A_{B\infty}$ can now be determined for a free stream.

Mach number = 2,0 where:

$$\% \; Bleed = \frac{A_{B\infty}}{P_\infty} \; x \; 100$$

and bleed mass flow is expressed as a percentage of captured mass flow.

A_∞ = 47,36 mm (Ref. Table 3.1), resulting in

$A_{B\infty}$ = A_∞ x 8/100

= 47,36 x 0,08

= 3,79 mm per unit width.

The bleed duct exit area is obtained from Table A.1 (Appendix A) where:

A_{ex} = 268 mm x 10^{-6} m^2 for the exit flow to be choked.

The stagnation pressure recovery measured at the bleed duct exit during wind-tunnel testing is typically 33 % (Stockenström 1990). From Table 3.1 for M = 2,0 the free stream stagnation pressure is obtained giving $P_{0\infty}$ = 792,85 kPa.

Taking the above-mentioned pressure recovery into account the stagnation pressure at the bleed duct exit is determined.

P_{oex} = 792,85 x 0,33

= 261,64 kPa

From the isentropic relations for $\gamma = 1,4$ the static pressure at the bleed duct exit can be determined (Zucrow & Hoffman 1976) where M = 1,0:

$$P_{ex} = P_{oex} \Big/ \left[1 + \frac{(\gamma - 1)}{2} M^2\right]^{\frac{\gamma}{\gamma - 1}}$$

$$= 261,64 \Big/ \left[1 + 0,2 \times 1^2\right]^{3,5}$$

$$= 138,22 \; kPa$$

The free stream dynamic pressure at M = 2,0 can be derived from equation 1:13 (Pope & Goin 1965) where:

$$q = \frac{\gamma}{2} PM^2$$

and P = static pressure

$$q_{\infty} = \frac{1,4}{2} \times 101,33 \times 2^2$$
$$= 283,72 \; kPa$$

In a similar way the dynamic pressure at the bleed duct exit is determined where M = 1,0:

$$q_{ex} = \frac{1,4}{2} \times 138,22 \times 1^2$$
$$= 96,75 \; kPa$$

Substituting all the relevant values into equation 16, where the width of the bleed streamtube area = 53,3 mm, yields:

$$D_{int} = 2 \times 283,72 \times 10^3 (3,79 \times 53,3 \times 10^{-6}) -$$
$$[(138,22 - 101,33)10^3 + 2 (96,75 \times 10^3)] 268 \times 10^{-6}$$
$$= 52,89 \text{ N}$$

The above equation, as derived from equation 14, takes account of the pressure losses as well as the change in momentum caused by the friction on the internal wetted surfaces of the boundary layer bleed duct.

The bleed drag for the inlet operating at Mach numbers 1,8 ; 2,0 ; 2,2 and 2,4 can be calculated in a similar manner and the results are depicted in Table 3.6 and Figure 3.21.

TABLE 3.6: Predicted Bleed Drag for a Bleed Ratio of 8% at Different Flight Mach Numbers

Mach No.	D_{int}
1,8	48,11 N
2,0	52,89 N
2,2	52,41 N
2,3	53,47 N
2,4	45,27 N

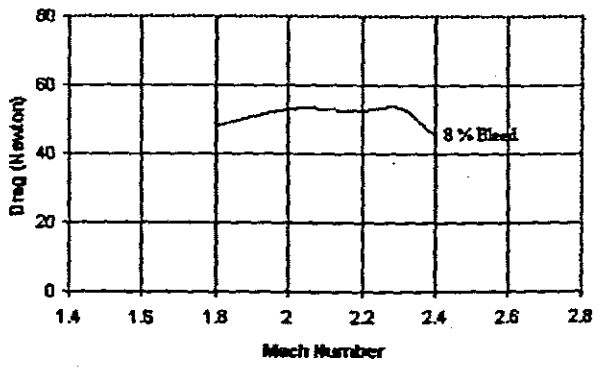

FIGURE 3.21 : Predicted Bleed Drag for Full-scale Porous Model

The bleed drag reaches a maximum value at M = 2,3 where the streamtube height is a maximum at the shock on lip condition. At M = 2,4 the oblique shocks focus inside the cowl lip with a loss in stagnation pressure recovery. The value of P_{ocx} is smaller resulting in the corresponding value of P_{ex} to be smaller. From equation 16 it can be seen that if the value of P_{ex} becomes smaller for a given value of P_{∞}, the value of D_{int} will also decrease.

3.3.5 Diverter Drag

3.3.5.1 Skin Friction Drag

The Reynolds number from Table 3.1 at M = 2,0 at sea level (height = 0) is found to be Re = 46 x 10^6/m. The Reynolds number based on a body length dimension is found for a diverter length 0,564 m resulting in :

$$R_t = 0,564\ (46 \times 10^6)$$
$$= 26 \times 10^6$$

Assuming turbulent compressible flow the skin friction drag coefficient can be determined from equation 21:

$$C_f = 0,427/\ (\log R_t - 0,407)^{2,64}$$
$$= 0,427/\ (\log 26 \times 10^6 - 0,407)^{2,64}$$
$$= 0,0025$$

The diverter height, h, is taken as:

$$h = 0,1 \times \text{missile diameter (Laruelle 1988)}$$
$$= 0,1 \times 180 \text{ mm (typical missile calibre = 180 mm)}$$
$$= 18 \text{ mm.}$$

From the plan view of the diverter, shown in Figure 3.22, the wetted area of the wedge can be calculated from:

$$S_{wet} = 2[(28,2/\sin 18,75°) \times 14,4]\ 10^{-6} + (481 \times 14,4)10^{-6}$$
$$= 9453 \times 10^{-6}\ m^2$$

The skin friction drag of the diverter wedge can now be determined from equation 20 where q_∞ = 283,72 kPa for M = 2,0:

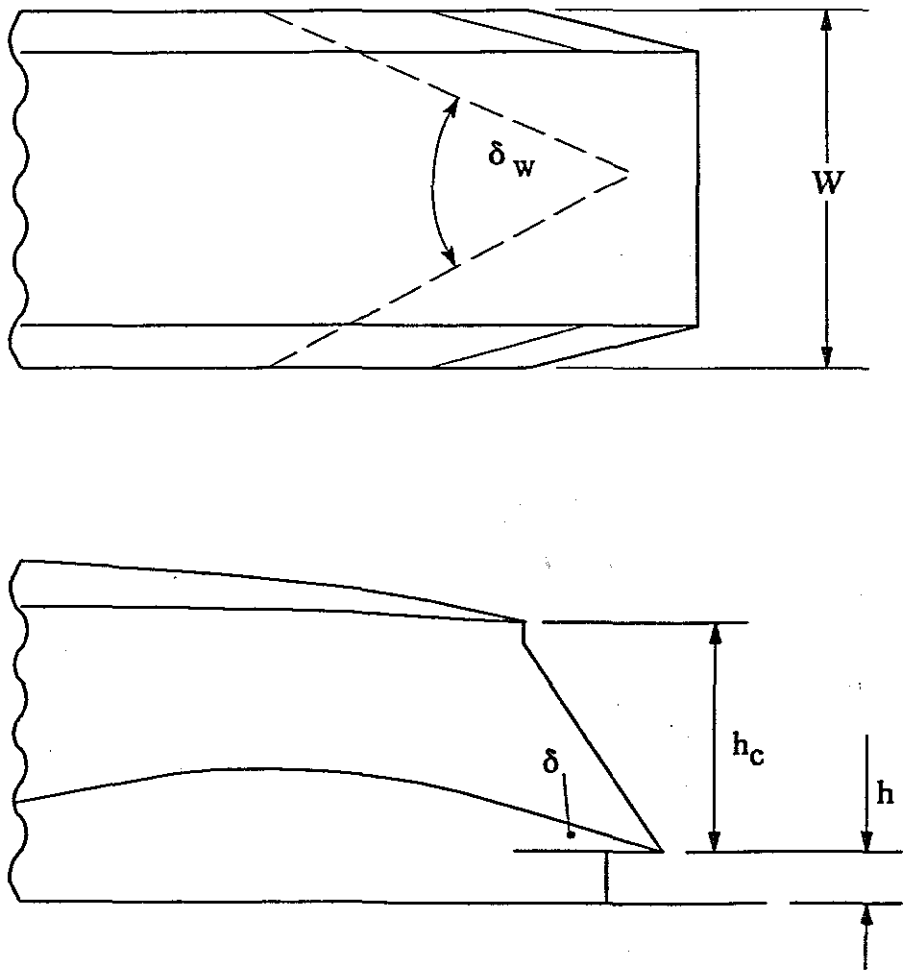

w = Diverter width = 56,4 mm
δ = Ramp deflection angle
δ_W = Diverter wedge angle = 37,5°
h_c = Height of capture area = 52,9 mm
h = Diverter height = 14,4 mm

FIGURE 3.22 : Geometry of Wedge Channel Diverter for Full-scale Porous Model

$$D_f = C_f S_{wet} q_\infty$$
$$= 0{,}0025 \times 9453 \times 10^{-6} \times 283{,}72 \times 10^3$$
$$= 6{,}71 \text{ N}$$

3.3.5.2 Wave Pressure Drag

The wave pressure drag, which is based on the projected frontal area of the diverter, has a much greater value than the skin friction drag. A value for the drag coefficient, C_d = 0,20, for a wedge diverter with a wedge angle of 37,5° operating at M = 2,0 is obtained from Figure 3.11. The Reynolds numbers covered by this curve, Re = 1,6 to 16,4 x 10^6/m are just below the range for flight conditions, where Re = 46 x 10^6/m.

The drag can now be calculated from equation 22:

$$D_p = C_d q_\infty S_f$$

Where:

$$S_f = 14{,}4 \times 56{,}4 \times 10^{-6} \text{ m}^2 \text{ (Ref. Figure 3.22)}$$
$$= 812{,}16 \times 10^{-6} \text{ m}^2$$

and $q_\infty = 283{,}72$ kPa

Substituting the relevant values in the above equation yields the value for:

$$D_p = 0{,}20 \times 283{,}72 \times 10^3 \times 812{,}16 \times 10^{-6}$$
$$= 46{,}09 \text{ N}$$

The total drag encountered by the diverter is determined as follows :

$$D_{div} = 6{,}71 + 46{,}09$$
$$= 52{,}80 \text{ N}$$

The diverter drag for the inlet operating at M = 1,8; 2,2; 2,3 and 2,4 can be calculated in a similar manner and the results are depicted in Table 3.7 and Figure 3.23.

TABLE 3.7: Predicted Diverter Drag at Different Flight Mach Numbers

Mach No.	D_{div}
1,8	42,76 N
2,0	52,80 N
2,2	63,87 N
2,3	69,82 N
2,4	76,02 N

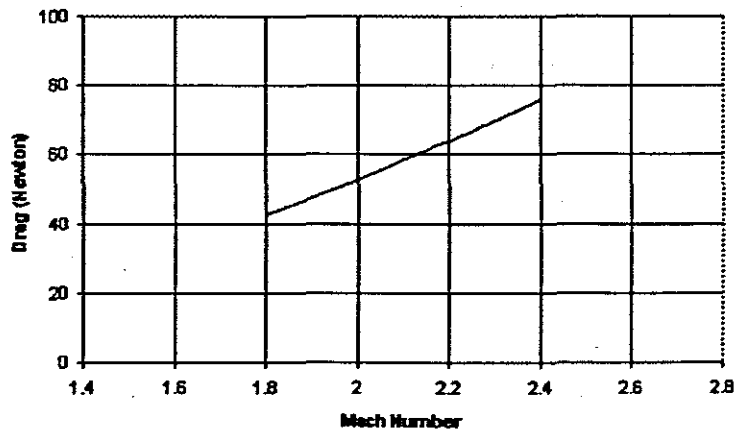

FIGURE 3.23 : Predicted Diverter Drag for Full-scale Porous Model

3.4 DISCUSSION OF CALCULATIONS

The results of the theoretical drag analysis for a specific operating mode, i.e. below the design Mach number where M = 2,0 and M = 1,8, each with a bleed flow rate of 8 %, are depicted in Tables 3.8 and 3.9 respectively. Results for the inlet operating at the design Mach number of M = 2,2 is depicted in Table 3.10. The inlet operating at M = 2,3, just above the design Mach number, the oblique shocks focus on the cowl lip, and the results for this operating mode are depicted in Table 3.11. At a flight Mach number of M = 2,4 the oblique shocks fall inside the cowl lip and no pre-entry drag is encountered. These results are depicted in Table 3.12.

TABLE 3.8: Theoretical Drag Analysis for Inlet Operating Critically and Sub-critically at M = 2,0 with a Bleed Flow Rate of 8 %

m_R	P_{re}	Spill	Cowl critical	Cowl subcritical	Bleed	D_{inl}	C_{dinl}
0,89	38,13 N	0	75,65 N	-	52,89 N	166,67 N	0,17
0,84	-	143,86 N	-	193,45 N	52,89 N	390,20 N	0,40
0,80	-	197,82 N	-	193,45 N	52,89 N	444,16 N	0,45
0,71	-	301,16 N	-	193,45 N	52,89 N	547,50 N	0,56
0,62	-	399,48 N	-	193,45 N	52,89 N	645,82 N	0,66
0,53	-	502,82 N	-	193,45 N	52,89 N	749,16 N	0,77

TABLE 3.9: Theoretical Drag Analysis for Inlet Operating Critically and Subcritically at M = 1,8 with a Bleed Flow Rate of 8 %

m_R	P_{re}	Spill	Cowl critical	Cowl subcritical	Bleed	D_{inl}	C_{dinl}
0,82	57,98 N	0	122,10 N *	-	48,11 N	228,19 N	0,29
0,78	-	102,22 N	-	122,10 N	48,11 N	272,43 N	0,34
0,74	-	129,39 N	-	122,10 N	48,11 N	299,60 N	0,38
0,66	-	190,85 N	-	122,10 N	48,11 N	361,06 N	0,46
0,58	-	248,76 N	-	122,10 N	48,11 N	418,97 N	0,53
0,49	-	310,08 N	-	122,10 N	48,11 N	480,29 N	0,61

* See Note 1 of Table 3.4

TABLE 3.10: Theoretical Drag Analysis for Inlet Operating Critically and Subcritically at M = 2,2 with a Bleed Flow Rate of 8 %

m_R	P_{re}	Spill	Cowl critical	Cowl subcritical	Bleed	D_{inl}	C_{dinl}
0,95	19,72 N	0	80,98 N	-	52,41 N	153,11 N	0,13
0,90	-	143,38 N	-	281,01 N	52,41 N	476,80 N	0,40
0,85	-	227,97 N	-	281,01 N	52,41 N	561,39 N	0,48
0,76	-	384,36 N	-	281,01 N	52,41 N	717,78 N	0,61
0,66	-	547,47 N	-	281,01 N	52,41 N	880,89 N	0,75
0,57	-	703,86 N	-	281,01 N	52,41 N	1037,28 N	0,88

TABLE 3.11: Theoretical Drag Analysis for Inlet Operating Critically and Subcritically at M = 2,3 with a Bleed Flow Rate of 8 %

m_R	P_{re}	Spill	Cowl critical	Cowl subcritical	Bleed	D_{inl}	C_{dinl}
0,99	2,16 N	0	88,28 N	-	53,47 N	143,91 N	0,11
0,94	-	122,94 N	-	330,17 N	53,47 N	506,58 N	0,39
0,89	-	225,87 N	-	330,17 N	53,47 N	609,51 N	0,47
0,79	-	417,46 N	-	330,17 N	53,47 N	801,10 N	0,62
0,69	-	616,19 N	-	330,17 N	53,47 N	999,83 N	0,77
0,59	-	807,41 N	-	330,17 N	53,47 N	1191,05 N	0,92

TABLE 3.12: Theoretical Drag Analysis for Inlet Operating Critically and Subcritically at M = 2,4 with a Bleed Flow Rate of 8 %

m_R	P_{re}	Spill	Cowl critical	Cowl subcritical	Bleed	D_{inl}	C_{dinl}
1,0	0 *	0	87,78 N	-	45,27 N	133,05 N	0,09
0,95	-	114,21 N	-	383,81 N	45,27 N	543,29 N	0,39
0,91	-	213,54 N	-	383,81 N	45,27 N	642,62 N	0,46
0,80	-	451,58 N	-	383,81 N	45,27 N	880,66 N	0,63
0,71	-	681,32 N	-	383,81 N	45,27 N	1110,40 N	0,79
0,60	-	919,36 N	-	383,81 N	45,27 N	1348,44 N	0,96

* See explanation in Table 3.2

Drag is commonly expressed in coefficient form. The inlet and the diverter is seen as two separate components while the total drag coefficient represents the total drag experienced by the inlet and diverter. The different drag coefficients, based on free stream dynamic pressure and projected frontal area, are defined below:

(i) Drag coefficient for diverter:

$$C_{ddiv} = \frac{Ddiv}{q_\infty \, (Diverter\ frontal\ area)}$$

(ii) Drag coefficient for inlet:

$$C_{dinl} = \frac{Dinl}{q_\infty \, (Inlet\ frontal\ area)}$$

(iii) Total drag coefficient for inlet and diverter :

$$C_{dt} = \frac{(Ddiv + Dinl)}{q_\infty \ (Frontal\ area\ of\ diverter + inlet)}$$

A summation of the theoretical values for the different drag coefficients, as defined above are, depicted in Table 3.13 and Figures 3.24, 3.25 and 3.26.

TABLE 3.13: Theoretical Drag Coefficients for Different Operating Modes at Various Flight Mach Numbers where Bleed = 8%

M = 1,8						
m_R	0,82	0,78	0,74	0,66	0,58	0,49
$C_{d\,div}$	0,23	0,23	0,23	0,23	0,23	0,23
$C_{d\,inl}$	0,29	0,34	0,38	0,46	0,53	0,61
$C_{d\,t}$	0,28	0,32	0,35	0,41	0,47	0,54
M = 2,0						
m_R	0,89	0,84	0,80	0,71	0,62	0,53
$C_{d\,div}$	0,23	0,23	0,23	0,23	0,23	0,23
$C_{d\,inl}$	0,17	0,40	0,45	0,56	0,66	0,77
$C_{d\,t}$	0,18	0,37	0,41	0,50	0,58	0,66
M = 2,2						
m_R	0,95*	0,90	0,85	0,76	0,66	0,57
$C_{d\,div}$	0,23	0,23	0,23	0,23	0,23	0,23
$C_{d\,inl}$	0,13	0,40	0,48	0,61	0,75	0,88
$C_{d\,t}$	0,15	0,37	0,43	0,54	0,65	0,75
M = 2,3						
m_R	0,99*	0,94	0,89	0,79	0,69	0,59
$C_{d\,div}$	0,23	0,23	0,23	0,23	0,23	0,23
$C_{d\,inl}$	0,11	0,39	0,47	0,62	0,77	0,92
$C_{d\,t}$	0,13	0,36	0,43	0,55	0,67	0,79

M = 2,4						
m_R	1,0*	0,95	0,91	0,80	0,71	0,60
$C_{d\,div}$	0,23	0,23	0,23	0,23	0,23	0,23
$C_{d\,inl}$	0,09	0,39	0,46	0,63	0,79	0,96
$C_{d\,t}$	0,12	0,36	0,41	0,55	0,68	0,82

NB: Refer to section 3.4 for calculation of coefficients

* This ratio can be bigger than 0,92 for 8% bleed because the bleed flow ratio, A_{B_∞}, is expressed as a percentage of the captured mass flow, A_∞.

For better clarity, the total drag coefficient versus different mass flow ratios, m_R, at various flight Mach numbers are graphically displayed in Figure 3.24. Note that the curves indicate a change in shape where the inlet starts to spill at the various Mach numbers. At M = 1,8 this effect is not noticeable because a significant pre-entry drag is already present.

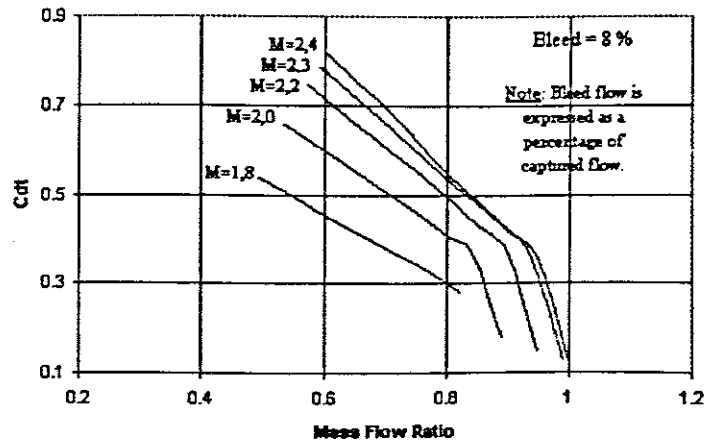

FIGURE 3.24 : Theoretical Total Drag Coefficient at Various Mach Numbers

In Figures 3.25 and 3.26 the characteristics of the inlet are displayed when operating subcritically at a mass flow ratio = 0,8 and critically at maximum mass flow rate respectively. It is clear from these graphs that the slope of each curve is opposite to each other. With reference to Figure 3.25, it is shown that there is an increase in the value of C_{dt} with an increase in the Mach number. This is a result of a lower value for the Mach number behind the normal shock with an increase in free stream Mach number. This lower Mach number behind the normal shock, with the inlet spilling, causes an increase in static pressure which acts on the cowl lip to cause a higher cowl drag.

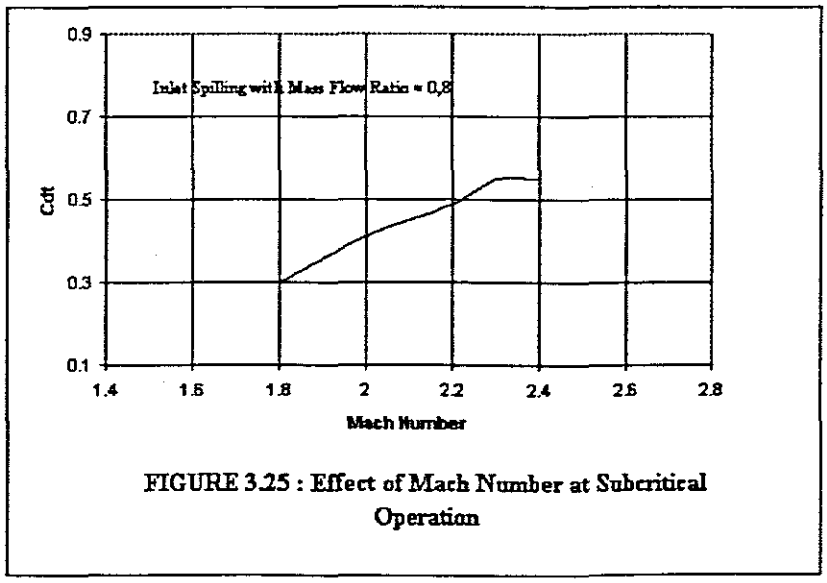

FIGURE 3.25 : Effect of Mach Number at Subcritical Operation

With reference to Figure 3.26 it is clear that there is a decrease in the value of C_{dt} with an increase in the Mach number at full flow conditions, i.e. no spillage. This is as a result of a reduction in pre-entry drag because at higher Mach numbers the oblique shocks are focussed closer to the cowl lip until a situation occurs at M = 2,3 where the oblique shocks are focussed on the cowl lip and the pre-entry drag becomes insignificant.

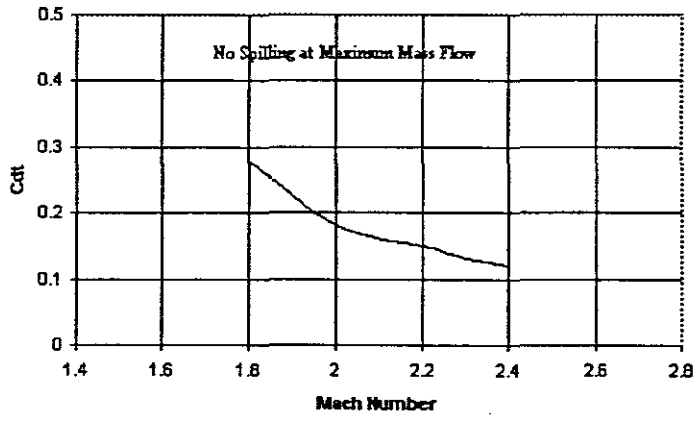

FIGURE 3.26 : Effect of Mach Number at Critical Operation

3.5 SUMMARY

From the values obtained for the drag calculations (Ref. Tables 3.8 to 3.12) it is clear that the cowl lip is a major drag contributing component of a two-dimensional external compression supersonic inlet. This high cowl wave pressure drag is a result of the big turning angle required to turn the incoming flow from the compression surface into the axial direction of the inlet duct.

It is essential to establish the drag as accurately as possible in order to optimise the inlet design with as little as possible drag working unfavourably on the system performance. From a systems point of view the design of the propulsion system cannot be done effectively if the magnitude of the drag penalty is not known. A lack of information can lead to a complete mission failure, especially in an application where constant fuel flow rate is used.

Wind-tunnel tests are recommended to establish the value of the total drag for a specific geometric shape as accurately as possible, to optimize the shape of the inlet and to correlate the validity of the results obtained by means of theoretical calculations.

CHAPTER 4

WIND-TUNNEL TESTS

4.1 INTRODUCTION

A very comprehensive experimental test program was required to verify the predicted drag figures discussed in section 3.4. It was further of crucial importance to set up the test matrix in such a way that it satisfies all the requirements in terms of model geometry, Mach numbers, Reynolds numbers and modes of operation.

The model selected was a full-scale light flight model, with geometric shape, size and surface finish representative of an inlet used in an actual flight mission application.

Aerodynamic drag tests were carried out on this full-scale model installed in the test section of the High Speed Wind-Tunnel (HSWT) of the CSIR. The inlet is provided with boundary layer bleed holes and the geometry of this "full-scale porous model" is fully described in section 4.2.2. The objective of these tests was to provide data, from which the aerodynamic drag coefficient at different flight conditions and various operating modes, could be established for a two-dimensional external compression inlet with fixed geometry.

It is further shown in section 4.4.2 how this inlet configuration is characterised in terms of drag coefficient versus mass flow ratio at different test Mach numbers, i.e. at design point, at shock on the lip position, below and above the design point. The mass flow ratios spanned critical, subcritical and supercritical flow regimes. The measurement of the drag of a supersonic inlet is a complex operation where model geometric layout and method of installation play a very important role. The reason for using an isolated inlet configuration (without fuselage) is to keep the experimental set-up simple and to eliminate as many external effects as possible. The emphasis is on a high level of data integrity and a model with realistic dimensions from which drag forces of measurable magnitude can be obtained. This isolated inlet configuration, with

a blockage of the order of 2,1%, falls within the maximum size specified in Appendix B for model testing in a high speed wind-tunnel.

Shock patterns for different flow regimes were investigated visually by taking Schlieren photographs of the inlet operating at different modes and the results for test runs at various Mach numbers are discussed in section 4.4.3.

In solving this fluid-flow problem the emphasis was placed on the dimensional analysis technique or experimental study since it is mentioned by White (1994:33) that: "A properly planned experiment is very often the best way to study a practical engineering flow problem".

4.2 EXPERIMENTAL EQUIPMENT

4.2.1 Wind-tunnel layout

Wind-tunnel tests were carried out in the High Speed Wind-Tunnel (HSWT) of the Aerotek Division of the CSIR in Pretoria. The layout of this tunnel consists of compressed air tanks, a flow control valve, a settling chamber, a nozzle with sonic throat and adjustable diverging walls to obtain the required test Mach number, test section with cross-sectional dimensions of 450 mm x 450 mm and exit duct to atmosphere.

The inlet model was fitted to a purpose made rig, specially made up for inlet testing. This rig forms part of an inlet cart, shown in Figure 4.1, and when this cart is moved into position, downstream of the test section, it becomes an integral part of the wind-tunnel.

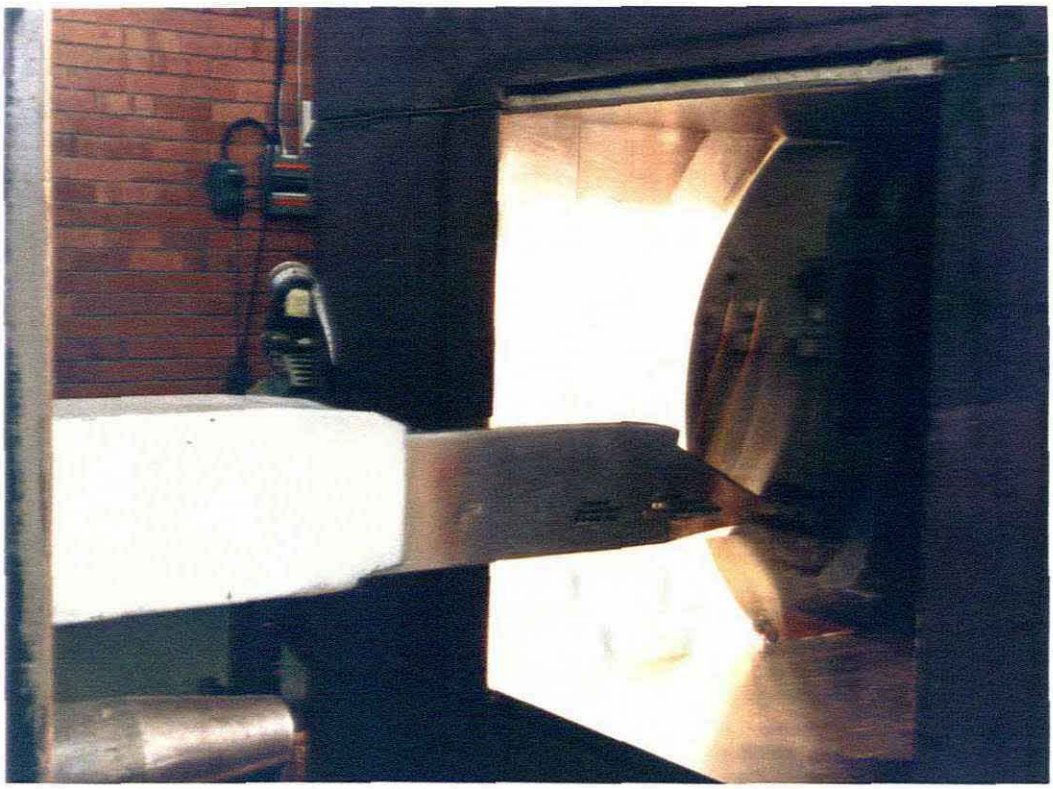

FIGURE 4.1 : Inlet Cart with Inlet Installed in Isolated Configuration

The model, ready for testing, is shown in the tunnel test section, Figure 4.2. Measuring equipment such as temperature and pressure probes are housed in this cart.

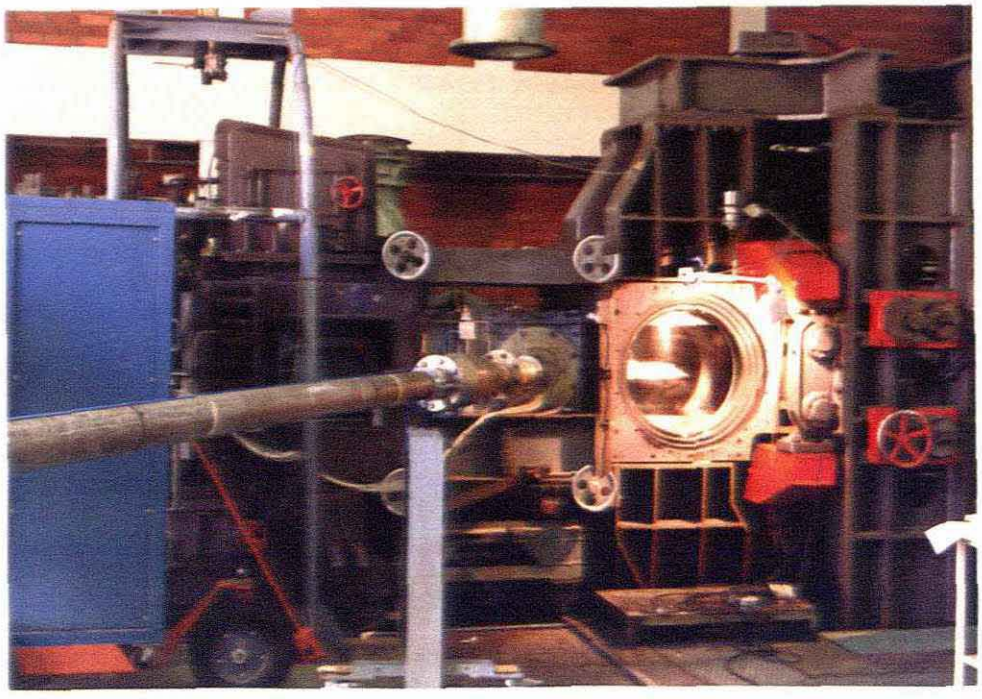

FIGURE 4.2 : Test Section of High Speed Wind-tunnel

The exit duct of the model is connected via a flexible steel bellows (Figure 4.3) to the mass flow control and measuring system on the outside of the test section.

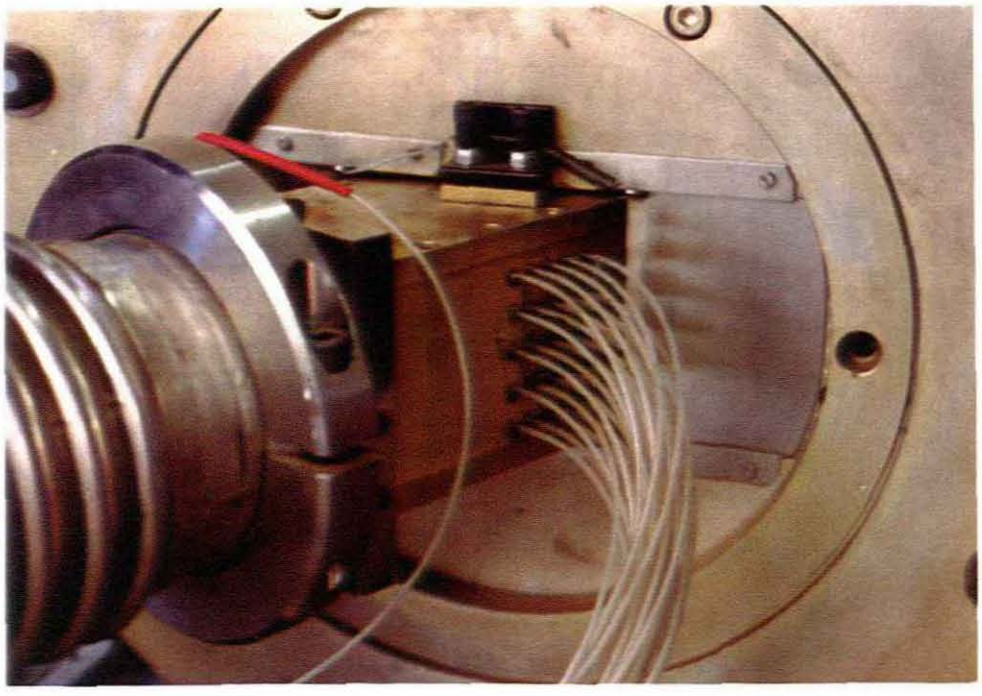

FIGURE 4.3 : Interface Between Model and Measuring Station

The exit of the model diffuser is connected to the bellows on the side of the cart. Moving downstream from the bellows the system comprises a flow straightener, a settling pipe, a flange housing the orifice plate, followed by a further length of settling pipe and finally the mass flow control plug.

The mass flow control plug, as shown in Figure 4.4, is moved forwards and backwards via a worm drive which is in turn connected to a stepper motor. The stepper motor is controlled by a personal computer in the control room to adjust the internal flow of the model for different operating modes, i.e. critical, subcritical and supercritical operation.

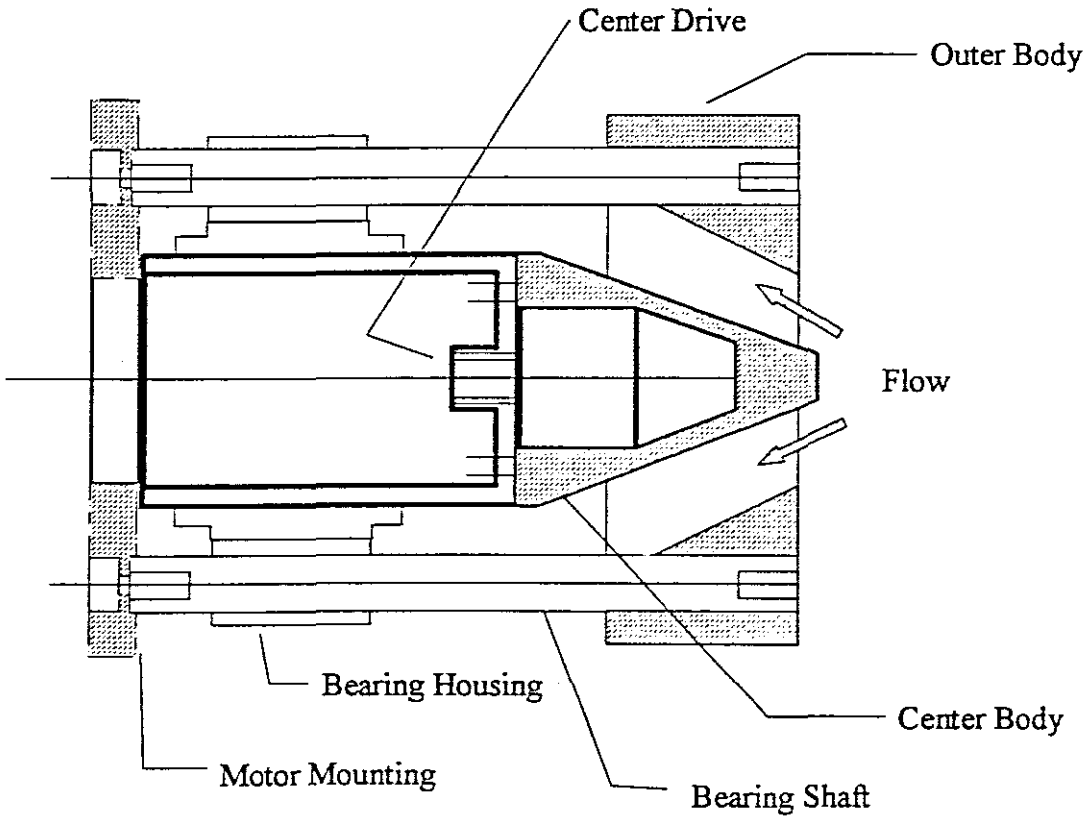

FIGURE 4.4 : Mass Flow Control Plug

Shown in Figure 4.5 is the model-balance integration where the rear end of the inlet model is connected via a strain gauge balance to an adaptor which fits onto the test rig of the inlet cart. The balance is of the flow-through type where captured air is allowed to flow through the center of the balance to the mass flow measuring device. All cables are shielded as protection against electrical interference and are taken via the test rig to data processing equipment on the outside of the tunnel. A special wind shield was designed (white duct in Figure 4.5) which slides over the balance to protect it from wind forces.

Great care was taken to set both pitch and yaw settings at zero degrees because any offset will cause the oblique shock waves to focus at an incorrect point resulting in test data which is of no value.

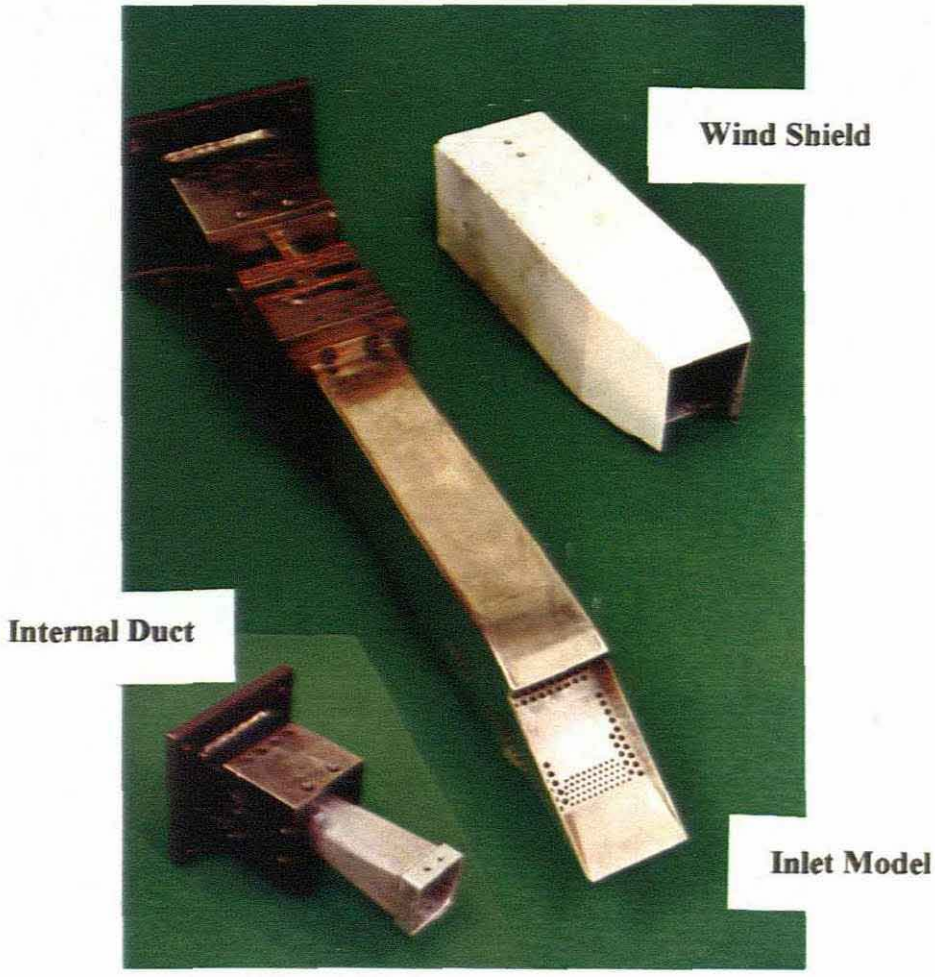

FIGURE 4.5 : Strain Gauge Balance Installation

4.2.2 Inlet Drag Model

The model used during this test program was a full-scale light flight model manufactured from 316 stainless steel. This resulted in a very representative model in terms of geometric tolerances, component dimensions and surface finishes. The model shown in Figure 4.6 is a two-dimensional, external compression inlet with double wedges and side plates. An important feature of this inlet model is the boundary layer bleed holes located on the compression surface of the second wedge and on the curved surface of the throat section as shown in Figure 4.7. It must be noted that the bleed holes on the second wedge were closed off during the test program due to excessive bleed mass flow ratios. This boundary layer bleed flow is dumped to atmosphere through the bleed exit holes in the side plates of the model as shown in Figure 4.6.

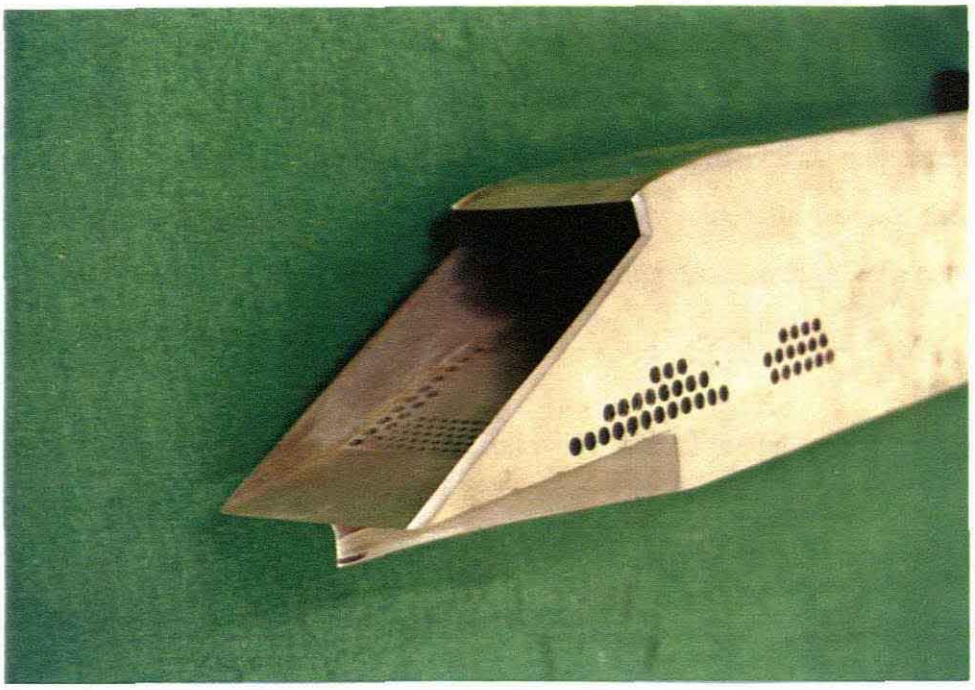

FIGURE 4.6 : Full-scale Porous Model

FIGURE 4.7 : Frontal View of Model Showing Bleed Holes

The model was also fitted with a diverter or splitter plate, starting at the edge of the first compression wedge and ending below the first row of bleed holes on the side of the inlet, as shown in Figure 4.6. The top section of the inlet duct consists of a cowl which turns the incoming flow into the axial direction of the inlet. The effective internal and external angles of the cowl lip are 5° and 19,3° respectively. It is very important to take these values, together with a value of 9° for the angle of the first compression wedge, into consideration when setting up the inlet model.

Experimental data processing required the following critical model dimensions, shown in Table 4.1, as input data:

TABLE 4.1 : Critical Model Dimensions

Capture height	52,9 mm
Capture width	53,3 mm
Throat height	31,7 mm
Total inlet height	61,02 mm
Total inlet width	56,4 mm
Inlet and diverter height Total frontal area for calculation of Cd	75,42 mm 4253,69 x $10^{-6}m^2$
Diverter height	14,4 mm
Diverter width	56,4 mm
Number of exit bleed holes open	32 Note: 16 holes on each side
Size of exit bleed holes	⌀ 3,8 mm

All the detailed dimensions of the model are depicted in Table A-1 of Appendix A and were checked in the metrology laboratory of the Cape Technikon.

The axial load of this six component (three moment and three force units) strain-gauge balance is directly proportional to the drag force. Strain caused by the axial load on the deflection beams was detected by strain-gauges glued onto the surfaces of these beams. Strain-gauges, connected in a Wheatstone bridge configuration, converted strain into electrical signals which were amplified and supplied to a computer in the control room of the tunnel.

The design of the balance was based on a tunnel stagnation pressure of 363 kPa, a typical pressure for testing over this Mach number range. The following values for expected axial and normal forces were determined at different inlet operating modes. The values shown in Tables 4.2 and 4.3 are for the inlet operating with and without bow shock respectively.

Table 4.2 : Axial and Normal force with bow shock

MACH No.	AXIAL FORCE (Newton)	NORMAL FORCE (Newton)
1,8	568	1281
2,0	554	1250
2,2	523	1180
2,3	499	1126
2,4	478	1079

Table 4.3 : Axial force without bow shock

Mach No.	AXIAL FORCE (NEWTON)	
	Min (No Spillage)	Max (40% Spillage)
1,8	170	328
2,0	99	362
2,2	73	367
2,3	59	360
2,4	52	352

Note: No side force component is expected at yaw and pitch angels of zero degrees.

The balance specifications are listed in Table 4.4.

Table 4.4 : Balance Specifications

Balance designation	Square Flow-through Inlet Balance
Dimensions	77 mm x 77 mm
Application	Drag measurement
Number of components	6
Load Range : Normal Force Pitching Moment Side Force Yawing Moment Axial Force Rolling Moment	1 300 N 370 Nm 1 300 N 370 Nm 600 N 50 Nm
Type	Square, Cage and Bar
Fit	Square, Pin and Bolt

The balance was calibrated with a special calibration jig before the test series commenced. The integrity of the data captured during data acquisition greatly depended on the accuracy of the calibration method. The full-scale errors of the balance accuracy is shown in Table 4.5. The calibration of an internal strain-gauge balance and the calculation of a calibration matrix is fully described by Ratner (1995), a member of the wind-tunnel project team of the Aerotek Division.

Table 4.5 : Full-scale Errors of the Balance Accuracy

Component	Percentage Error		
	Maximum	Mean	Standard Deviation
Normal Force	0,14	-0,01	0,09
Pitching Moment	0,16	0,01	0,08
Side Force	0,06	0,00	0,01
Yawing Moment	0,09	0,00	0,02
Axial Force	1,03	0,14	0,38
Rolling Moment	0,00	0,00	0,00

4.3 TESTING PROCEDURE

4.3.1 Test Matrix

Characterising the inlet in terms of drag, required the inlet to be tested over its full operational range, i.e. flight conditions and operating modes. The main objective of the test series was to obtain experimental data that is accurate and representative of real-life conditions so that these can be compared with the predicted theoretical values discussed in Chapter 3.

The test matrix depicted in Table 4.5 made provision for the inlet to be tested over the full operational range :

i) Flight conditions ranging from M = 1,8 to 2,4 where :

- M = 1,8 and M = 2,0 represent test Mach numbers below the design point;
- M = 2,2 represents a test Mach number at the design point;
- M = 2,3 represents a Mach number at the shock on lip (S.O.L.) condition;
- M = 2,4 represents a test Mach number above the design point.
- Pitch Angle, $\propto = 0$
- Yaw Angle, $\beta = 0$

TABLE 4.6 : Test Matrix

Run No.	Mach No.	Re No.	Mass flow ratio m_R	α	β
1	1,8	42 x 10^6/m	Full to Buzz	0	0
2	2,0	46 x 10^6/m	Full to Buzz	0	0
3	2,2	51 x 10^6/m	Full to Buzz	0	0
4	2,3	53 x 10^6/m	Full to Buzz	0	0
5	2,4	56 x 10^6/m	Full to Buzz	0	0

ii) Operating modes, ranging from full flow conditions to buzz (Ref. section 2.4) with critical, subcritical and supercritical modes, were fully investigated.

For a ground to air launch at sea level the flight vehicle will experience Reynolds numbers ranging from Re = 42 x 10^6/m at M_∞ = 1,8 to Re = 56 x 10^6/m at M_∞ = 2,4 (Ref. Tables A.2 to A.6 of Appendix A). The Reynolds numbers that could be supplied by the high speed wind-tunnel fall within his range.

It is however mentioned by White (1994:425) that for body drag at high Mach numbers, the Reynolds number effect for spheres and cylinders becomes unimportant above M ≈ 1,0. The effect of the Reynolds number for airfoils and projectiles is small and it is further stated that at M > 1,0 the Reynolds number is unimportant and the Mach number important for determining drag coefficients.

It is further shown in section 4.4.2 how the theoretical drag coefficients were compared with the experimental values obtained from this test series.

4.3.2 Tunnel Mach Number

The size and shape of the supersonic nozzle was adjusted to obtain the desired Mach number in the test section. For each blow of the tunnel, stagnation and static pressure readings were recorded. The test Mach number was calculated by substituting the relevant values into the following equation (Zucrow & Hoffman 1976:156) for steady one-dimensional flow of a perfect gas:

$$\frac{P_0}{P} = \left[1 + \frac{\gamma - 1}{2} M^2\right]^{\frac{\gamma}{\gamma - 1}}$$

where 0 denotes stagnation conditions.

Pressures were recorded using the Hyscan 2000 pressure measuring system of the High Speed Wind-tunnel (HSWT). Corresponding pressure points in the tunnel were connected via thin bore PVC tubing, to the measuring instrument. The accuracy of the 15 psi modules, on which pressures were measured, is 0,083 kPa.

4.3.3 Mass Flow Regulation and Measurement

The test matrix required the inlet to be tested through its full range of operational modes, i.e. from full flow to "buzz" (Ref. section 2.4). The flow through the inlet was regulated by a mass flow control plug (valve), shown in Figure 4.4. The axial movement of this plug was controlled by a Compumotor controller, in turn controlled by a program from a personal computer in the control room of the tunnel.

During each test run (tunnel blow) the position of the control plug was varied in steps from an open to a closed position. The control parameters that were required for each blow were the start and end positions, the number of steps and the total movement time. These parameters were selected in such a way that for each test run a portion of the data captured, covered the supercritical, critical and subcritical operating modes. The control parameters were established through a trial and error process for each test configuration.

Mass flow through the inlet was based on a method using an orifice plate, situated upstream of the mass flow control plug and downstream of the inlet cart. The orifice plate was designed according to British Standards (BS 1042: Section 1.1: 1981). An accuracy of 1 part in 600, i.e. 0,17 % is specified for the discharge coefficient if all the requirements, as stated in above-mentioned standard, are adhered to. Static pressure measurements across the orifice plate (required for mass flow calculations) were performed using a Scanivalve Hyscan 2000 system. Readings were recorded on the 15 psi modules with an accuracy of 0,083 kPa.

4.3.4 Bleed Flow Measurement

The formation of a boundary layer on the compression surfaces of the inlet and the interaction of shocks with the boundary layer cause detrimental pressure gradients and flow separation. In an attempt to solve this very difficult flow problem a boundary layer bleed system was incorporated in the full-scale model shown in Figure 4.7. The boundary layer air was bled off through the bleed holes in the throat area, to a bleed chamber below the throat region. From this chamber it was dumped through holes in the side of the inlet duct (Figure 4.6) to the tunnel test section.

Since the bleed flow rate has an influence on the total drag of the inlet it is of great importance to measure this flow rate very accurately. The bleed flow rate can be varied by opening or closing the number of holes in the side of the inlet duct. For a given value of the total exit area, A_{ex} (each bleed hole is assumed to react similarly to a square edge orifice with diameter ratio of 0,2) the bleed mass flow is governed by the bleed chamber static pressure, P_{bc}. A rise in this pressure will cause the air density to increase resulting in a higher bleed mass flow rate.

Bleed mass flow measurements were based on choked orifices, each with a known area. Stagnation pressure, P_{0B}, measurements were taken at the exit plane inside the bleed chamber. The value for the pressure ratio P_0/P is required to establish whether the orifice is choked or not. This critical pressure ratio, where the stagnation pressure is sufficient to ensure choking of the orifice is given by Zucrow & Hoffman (1976:157):

$$\frac{P^*}{P_0} = \left(\frac{2}{\gamma + 1}\right)^{\frac{\gamma}{\gamma - 1}}$$

$$\frac{P_S}{P_{0B}} = 0{,}583 \qquad OR \qquad \frac{P_{0B}}{P_S} = 1{,}893$$

where : γ = 1,4 for air (Zucrow & Hoffman 1976:700);

P_S = Static pressure in tunnel test section and

$*$ denotes critical flow properties where the flow is sonic, M = 1,0.

When choking of the orifices or porous plate is established the only other information required for mass flow calculations is the value of the stagnation temperature. In cold-flow tests it is assumed that the stagnation temperature, T_o, at the measuring point is the same as the stagnation temperature of the tunnel settling chamber and it stays constant throughout the duct (Seddon & Goldsmith 1985). The static temperature, T, was determined from the following equation (Zucrow & Hoffman 1976:157) :

$$\frac{T^*}{T_0} = \left(\frac{2}{\gamma + 1}\right)$$

It follows that the density of the air at the orifice exit was determined from:

$$\rho^* = \frac{P}{RT}$$

Where :

P = static pressure at orifice exit

R = 287,06 J/kg K (Zucrow & Hoffman 1976:700).

The velocity of the air at the orifice exit, which is also required in the mass flow calculation, was found from the equation:

$$V^* = M\sqrt{\gamma RT}$$

From the continuity equation the maximum mass flow is (White 1994:525) :

$$\dot{m} = \rho^* A V^*$$

By substituting the relevant values into the above equation the bleed mass flow rates, discussed in section 4.4.4, were determined.

4.4 RESULTS AND DISCUSSION

4.4.1 Data Processing

The capturing of data was performed using the Hyscan 2000 system of the High Speed Wind-tunnel. Once the data was captured it was copied to the personal computer of the test engineer where it was processed.

Records of the data logged represent the chronological sequence of the tests performed on the full-scale porous model. Other important information such as tunnel stagnation pressure, atmospheric pressure, the names of data files, model configuration and blow numbers are listed in Appendix C.

4.4.2 Drag Coefficient

From the onset in the analysis of the raw data, corrections had to be made to compensate for external and internal factors influencing the balance readings. The important question that had to be answered was: what are the sizes and directions of the axial forces affecting the balance readings?

After careful consideration of the test set up and model configuration, it was concluded that the primary factors influencing the axial force readings were:

i) the thrust generated by the internal duct, which passes through the internal section of the balance, and ejected air into the ducting of the inlet rig;

ii) the build up of pressure in the chamber between the balance and the wind shield.

All relevant data were recorded for different control plug positions (Ref. section 4.3.3) and mean values and standard deviations for the axial force measurements were calculated as shown in Table 4.7.

Table 4.7 : Mean values and standard deviations for axial force measurements at various test Mach numbers

M = 1,8			M = 2,0			M = 2,2			M = 2,3			M = 2,4		
F_A (N)	SD	Z %	F_A (N)	SD	Z %	F_A (N)	SD	Z %	F_A (N)	SD	Z %	F_A (N)	SD	Z %
-119	21	93	-139	23	86	-100	15	93	-91	17	93	-59	13	100
-129	10	100	-212	14	100	-101	3	100	-92	5	100	-54	9	93
-134	8	100	-218	5	93	-103	8	93	-101	8	100	-62	7	100
-123	8	100	-201	23	100	-91	5	93	-102	6	100	-61	5	100
-103	16	100	-178	15	100	-90	5	93	-100	5	100	-59	6	100

N Newton

F_A Mean Axial Force Readings

SD Standard Deviation

Z Percentage data points which fall within two standard deviations on either side of mean value.

A statistical analysis of this data shows that for a total of 25 test positions, constituted by five Mach numbers times five different mass flow ratios, in one case only did 14% of the data points fall outside two standard deviations on either side of the mean value. In the other 24 cases did between 93% and 100% of the data points fall within these above-mentioned limits. In these cases a reasonably small distribution of data points about the mean is achieved. It can be said with confidence that the scatter of measured data points lies within acceptable limits. The reduction of this mean axial force data is based on the following analysis and the corrected values were married to the recorded mass flow ratios as shown in Table C3.

With reference to the geometric layout of the inlet model, it is clear that the installation of an internal duct (Ref. Figure 4.5) caused the internal geometry of the inlet model to deviate from that used in an actual inlet, as installed on an air-breathing engine. This internal duct can be described as a converging section, passing in an axial direction through the inside of the balance, connecting the subsonic diffuser with the ducting of the inlet rig.

The correction to the axial force measurements is based on Newton's second law of motion (Zucrow & Hoffman 1976:87) for fluid flowing through a control volume. The internal duct defined as the control volume is depicted in Figure C.1 of Appendix C. The momentum equation defines that the sum of the external forces acting on the control volume is equal to the change in momentum through the control volume.

With reference to the control volume in Figure C.1 :

$$F_T + P_1A_1 - P_2A_2 = \dot{m}_c\,(V_2 - V_1)$$

Where :

A	Cross-sectional area
F_T	Stream thrust, N
P	Static pressure, kPa
V	Velocity, m/s
$\dot{m}_c$	Captured mass flow, kg/s
1	denotes entrance plane conditions
2	denotes exit plane conditions.

Stream thrust calculations were conducted for different mass flow ratios, m_R, and stagnation pressure recovery ratios, P_R. From wind-tunnel test data (Stokenström 1991) of an inlet model with the same geometric shape, corrected values for the stagnation pressure recovery were derived so as to obtain the representative values for the stagnation pressure, P_0, at the entrance plane of the control volume (Ref Table C.3).

The wind-tunnel supplied a specific stagnation pressure to the model at each test Mach number. This pressure caused the model to get "started" and ensured testing at the correct Reynolds number. The model was operated at a specific mass flow rate at each setting of the mass flow control valve. From the continuity equation for stagnation conditions (Zucrow & Hoffman 1976:144)

$$\dot{m} = AMP_0 \left(\frac{\gamma}{RT_0} \right)^{\frac{1}{2}} \left(1 + \frac{\gamma - 1}{2} M^2 \right)^{-(\gamma + 1)/2(\gamma - 1)}$$

the velocity at the exit plane, station 2 in Figure C.1, was calculated for different values of $\dot{m}_c$ and P_0. The velocity at the entrance plane, station 1, was based on the velocity behind the normal shock in the subsonic diffuser, and on a change in area ratio.

Substituting the relevant values for stagnation conditions into the equations for steady one-dimensional flow, yielded the corresponding values for static conditions at the entrance and exit planes of the control volume. From this information for static pressure and velocity the stream thrust for different captured mass flow rates was calculated for each Mach number. The results are listed in Table C.3.

The thrust component opposed the drag component and was subtracted from the measured axial force, F_A, resulting in a corrected drag force. The effect of the chamber pressure on the axial force was another correction that had to be considered. This pressure was measured in the cavity or chamber between the balance and the wind shield. When applied on an effective projected area an unbalanced force, $F_{chamber}$, was created which pushed the inlet model downstream, adding to the drag component. It must be noted that a negative sign denotes a force acting in an upstream direction. The net drag is therefore defined as follows :

$$D_{net} = (F_A - F_T) - F_{chamber}$$

From the results given in Table C.3 the following graphs were generated :

Figure 4.9 depicts the relationship between the theoretical and experimental drag coefficients at a free stream Mach number of 1,8.

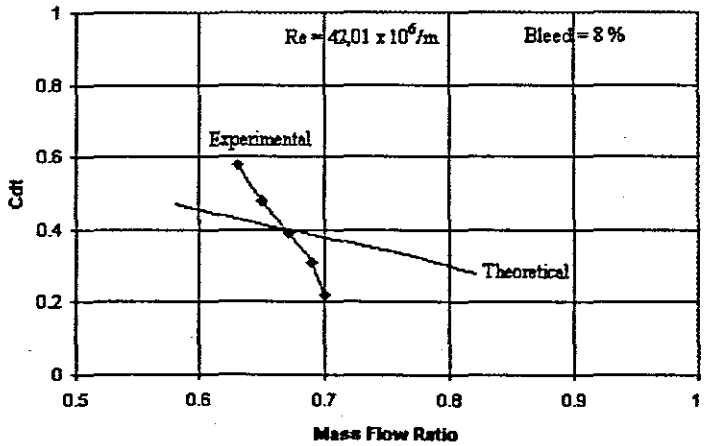

FIGURE 4.9 : Comparison between Theoretical and Experimental Values at M=1,8

Figure 4.10 depicts the relationship between the theoretical and experimental drag coefficients at a free stream Mach number of 2,0.

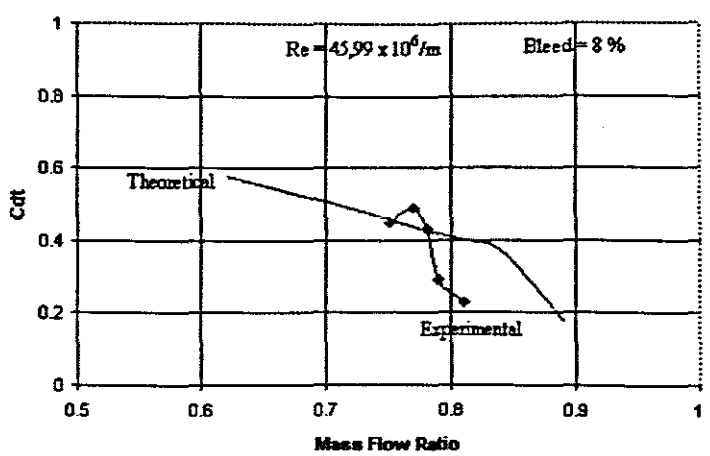

FIGURE 4.10 : Comparison between Theoretical and Experimental Values at M=2,0

Figure 4.11 depicts the relationship between the theoretical and experimental drag coefficients at a free stream Mach number of 2,2.

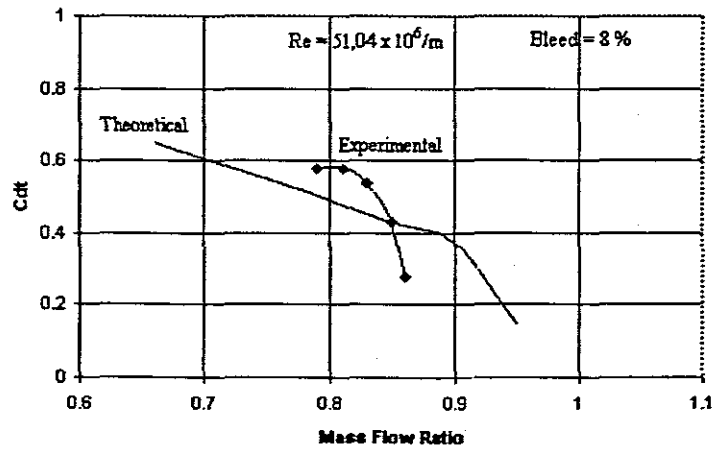

FIGURE4.11 : Comparison between Theoretical and Experimental Values at M=2,2

Figure 4.12 depicts the relationship between the theoretical and experimental drag coefficients at a free stream Mach number of 2,3.

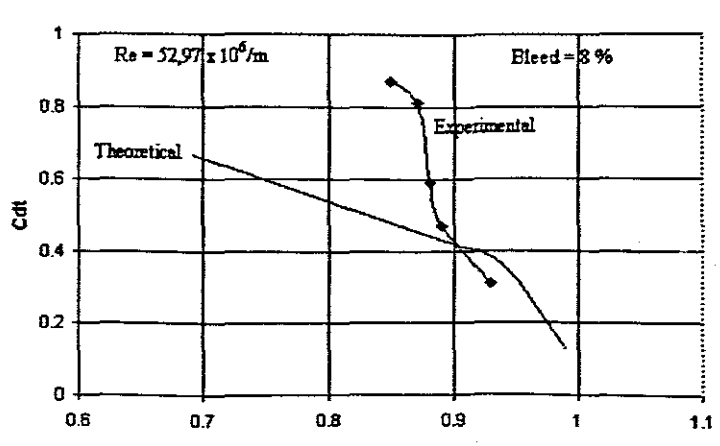

FIGURE 4.12: Comparison between Theoretical and Experimental Values at M=2,3

Figure 4.13 depicts the relationship between the theoretical and experimental drag coefficients at a free stream Mach number of 2,4.

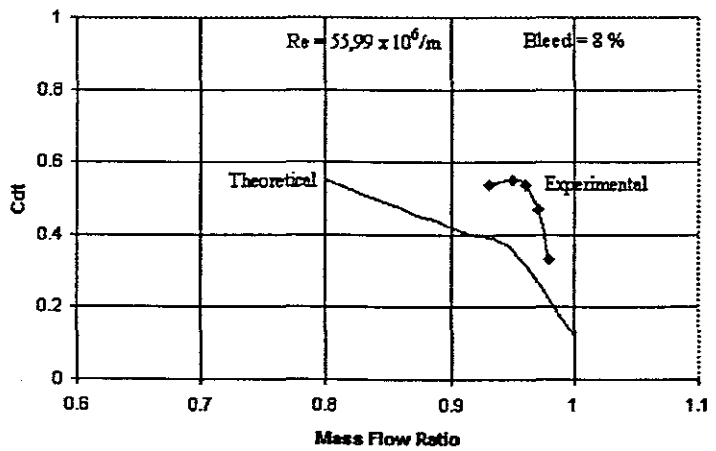

FIGURE 4.13 : Comparison between Theoretical and Experimental Values at M=2,4

It must be noted that tests were carried out at the correct Reynolds numbers and operational modes. In each graph the mass flow ratio, m_R, and total drag coefficient, C_{dt}, are represented by the x and y axis respectively.

The curves in each figure show the same trend, namely an increase in the value of C_{dt} with a decrease in mass flow ratio, m_R. The rising section of each curve indicates an increase in drag with the inlet operating subcritically, spilling excess air around the cowl lip. All tests were terminated when a minimum captured mass flow rate was reached. At this point the inlet started to "buzz" (inlet became unstarted with normal shock pushed out in front of the inlet and severe pressure oscillations occurred) and testing was curtailed so as to protect the model and balance from damage. No usable data were captured for the "buzz" condition.

With reference to Figures 4.9, 4.10, 4.11, 4.12 and 4.13 reasonably good agreement between the theoretical and experimental total drag coefficient values is achieved at low subcritical modes of operation. Two very important observations are made when these curves are studied. The operational range mass flow ratio, is much smaller than expected due to boundary

layer effects. It is clear from the test data and the visual material that the subcritical margin of operation was greatly reduced due to a lack of boundary layer bleed on the surface of the compression ramp. (Note bleed holes were closed off to achieve a realistic bleed rate of 8%, as used during theoretical calculations). A second observation is that the slopes of the experimental curves are much steeper than that of the theoretical curves because the margin of subcritical operation is much smaller and spill has a more drastic effect on the drag as expected. This steeper rise in drag with the inlet spilling can be attributed to serious flow disturbances when the normal shock and oblique shocks interacted. The interaction of the root of the normal shock with the boundary layer on the compression ramp, also contributed to a higher drag penalty than expected.

An analysis of the data in Figures 4.9 to 4.13 for maximum flow conditions shows that there is a variation in the drag coefficient with a change in Mach number. The following data is of significance :

- at M = 1,8 $C_{dt} = 0,22$
- at M = 2,0 $C_{dt} = 0,23$
- at M = 2,2 $C_{dt} = 0,28$
- at M = 2,3 $C_{dt} = 0,31$
- at M = 2,4 $C_{dt} = 0,33$.

This data indicates that there is an increase of 50% in the value of C_{dt} with an increase in Mach number. This needs for further investigation because the higher average drag figures measured at M = 2,3 and M = 2,4, where the oblique shocks were focussed on or inside the cowl lip at M = 2,3 and M = 2,4 respectively, were presumably caused by significant flow distortions in the air entering the inlet. These distortions are caused by the interaction of the oblique shocks with the boundary layer on the inside of the cowl lip resulting in flow separation with an eventual drag penalty.

4.4.3 Flow Visualisation

Shock patterns were recorded for all test runs using Schlieren equipment. Video recordings, as shown in Figures 4.14 to 4.19, were made for test Mach numbers ranging from M = 1,8 to 2,4, over the full operating range as specified in the test matrix (Table 4.5).

With reference to the following figures, the following observations can be made:

- Figure 4.14: shows that at critical and supercritical operation the oblique shocks from the compression wedges were focussed at some distance in front of the cowl lip at M = 1,8. An oblique shock, generated by the inclined leading edge of the lip, is clearly shown with an expansion fan at the top corner of the lip rounding off the picture. At the subcritical mode of operation the inlet was spilling excess air while the normal shock was situated in front of the lip. At this Mach number the inlet has very good subcritical operational characteristics.

- Figure 4.15 shows the external flow field with shock patterns for the inlet operating at M = 2,0. The oblique shocks were focussed closer to the cowl lip at the Mach number below the design point with a good margin for stable subcritical operation.

- Figure 4.16 depicts the inlet during operation at the design Mach number, M = 2,2, where the oblique shocks were focussed just in front of the cowl lip. The inlet was reasonably stable during subcritical operation and the vortex generated by the intersection of the oblique shocks just missed the inlet opening.

- Figure 4.17 shows the inlet operating with the oblique shocks focussed on the cowl lip at M = 2,3. This is not a desirable situation, since the intersection (focus) of the oblique shocks caused flow separation where it interfered with the boundary layer of the cowl lip. The inlet became unstable during subcritical operation as is shown in Figure 4.17 (b).

- Figure 4.18 depicts the inlet operating at M = 2,4 with the oblique shocks focussed inside the cowl lip. This situation should be avoided since the vortex generated by the intersection of the two oblique shocks was ingested into the inlet and caused the internal flow to become unstable. The inlet has a very limited margin of subcritical operation at this Mach number and "buzz" was initiated soon after the normal shock started to appear in front of the inlet opening.

"Buzz" is initiated when the normal shock is pushed out of the inlet causing the shock pattern to break up and the flow to become separated, resulting in large pressure oscillations. These pressure gradients in the external flow field can be seen in Figure 4.19.

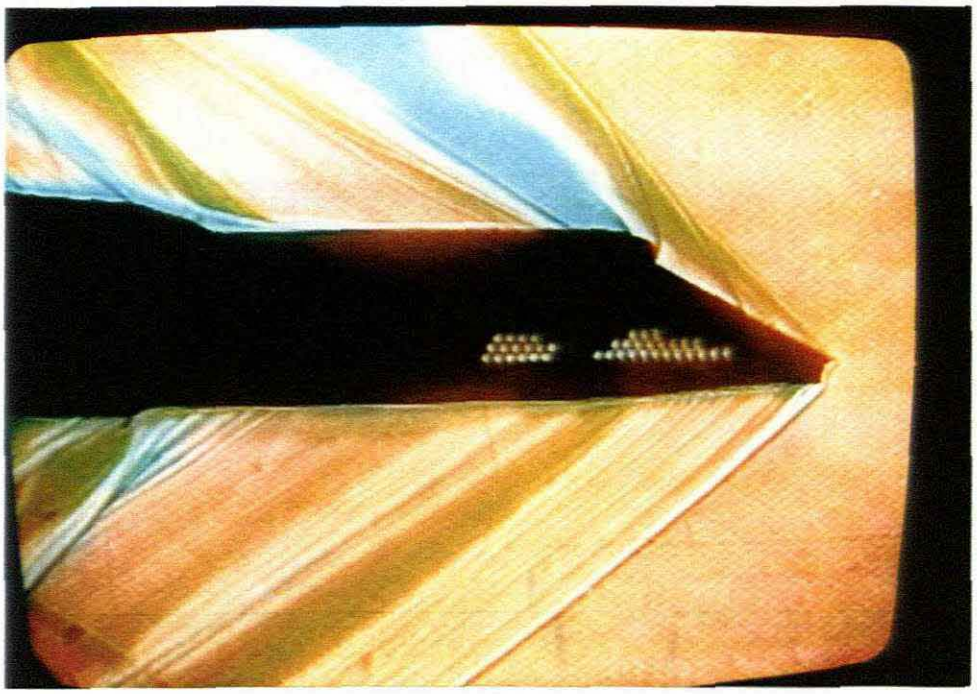

(a) Critical and Supercritical Flow

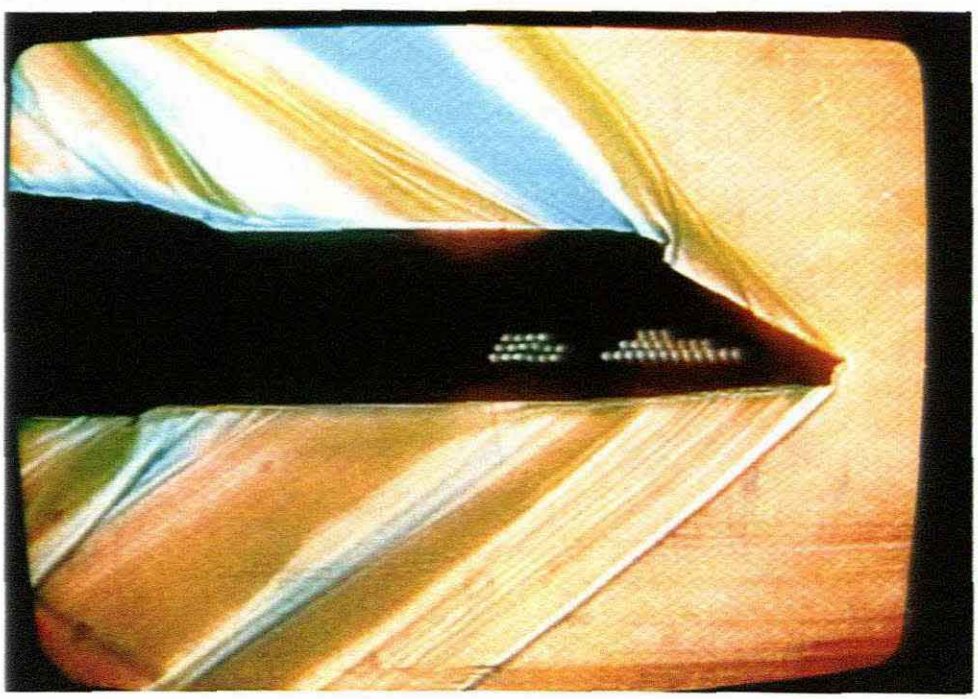

(b) Subcritical Flow

FIGURE 4.14 : External Flow Field Showing Shock Patterns for M_∞ = 1,8
(Below the Design Mach No.)

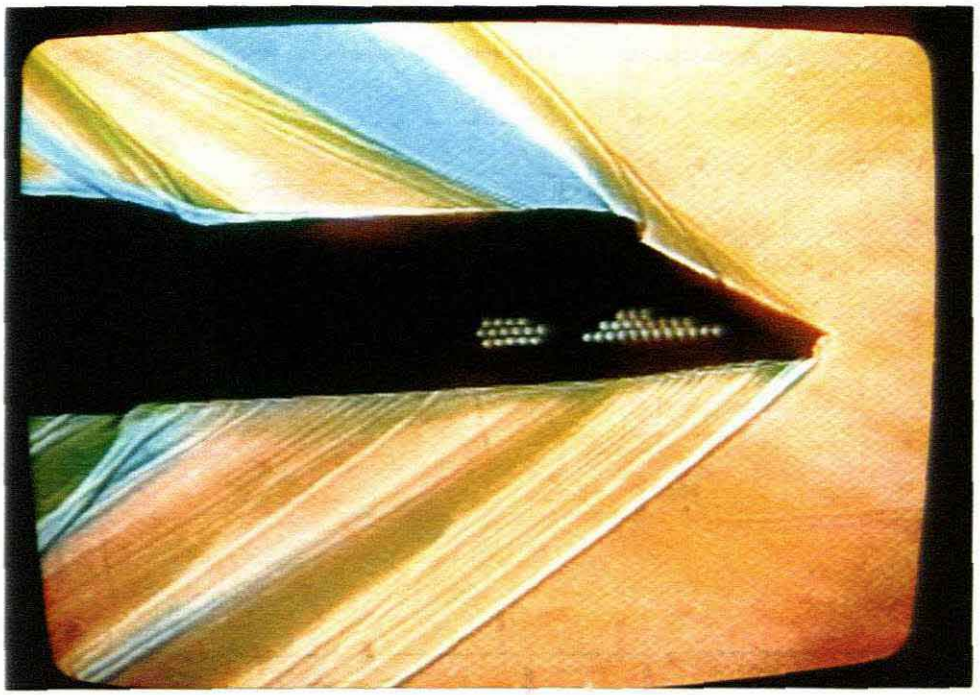

(a) Critical and Supercritical Flow

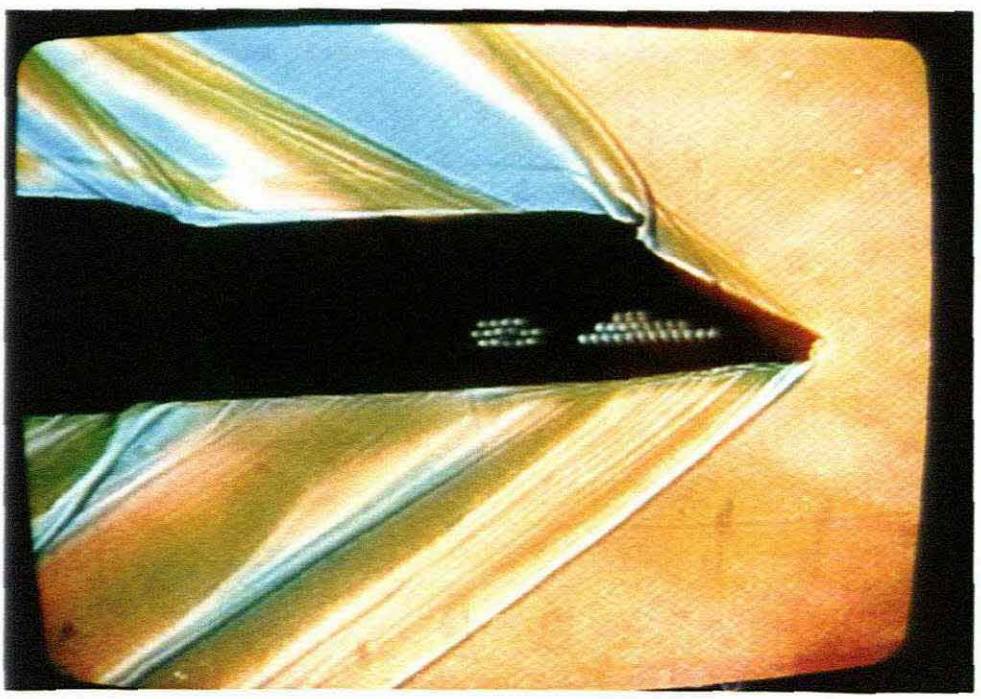

(b) Subcritical Flow

FIGURE 4.15 : External Flow Field Showing Shock Patterns for $M_\infty = 2,0$ (Below the Design Mach No.)

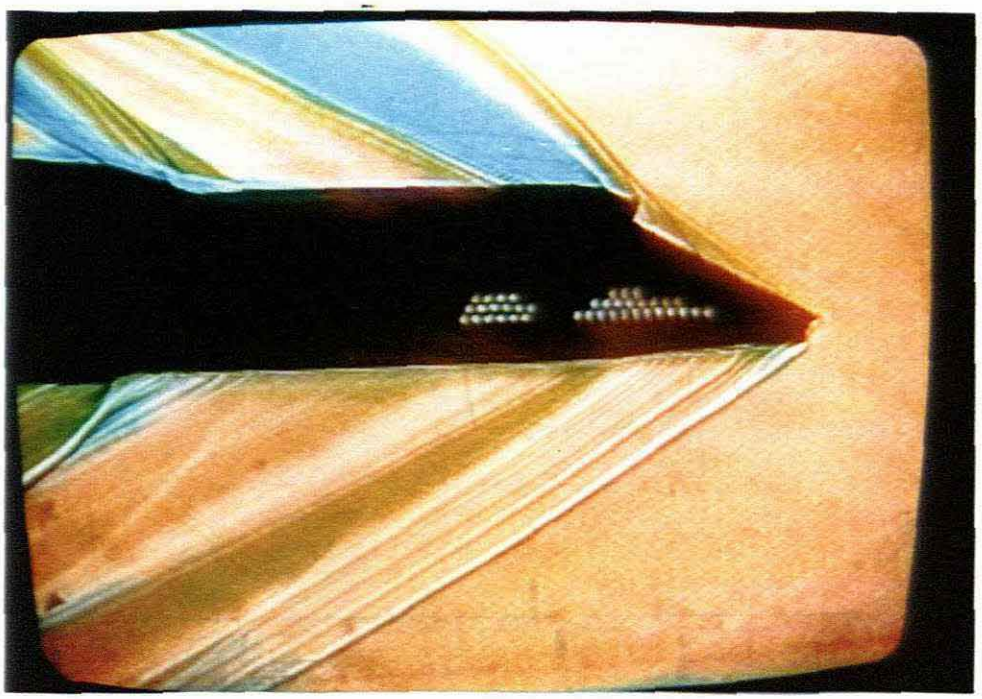

(a) Critical and Supercritical Flow

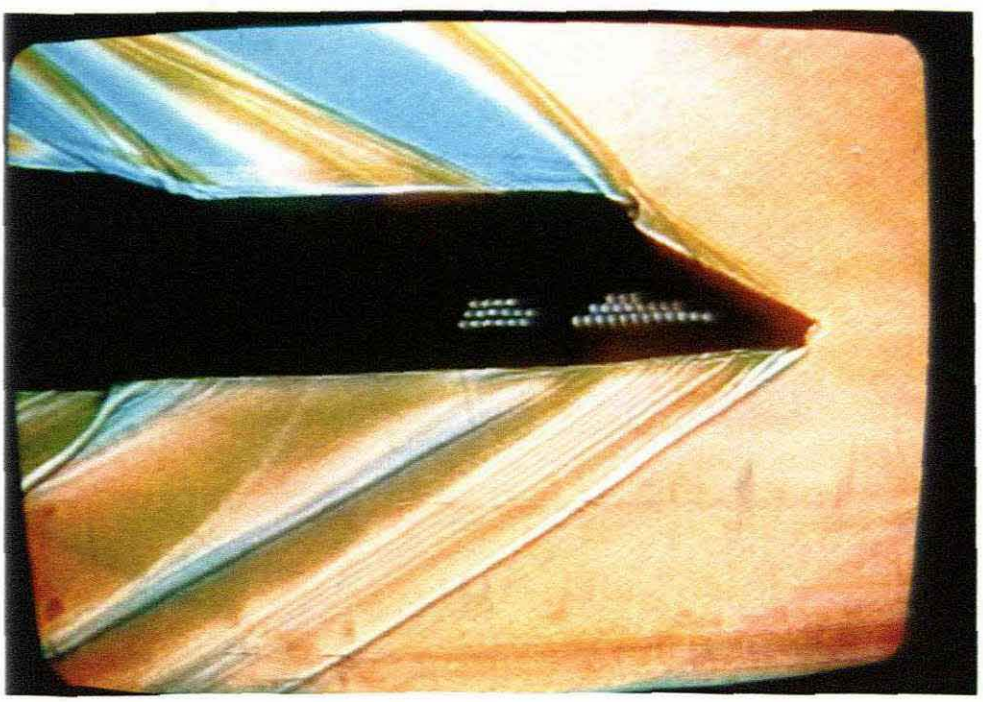

(b) Subcritical Flow

FIGURE 4.16 : External Flow Field Showing Shock Patterns for $M_\infty = 2.2$
(At the Design Mach No.)

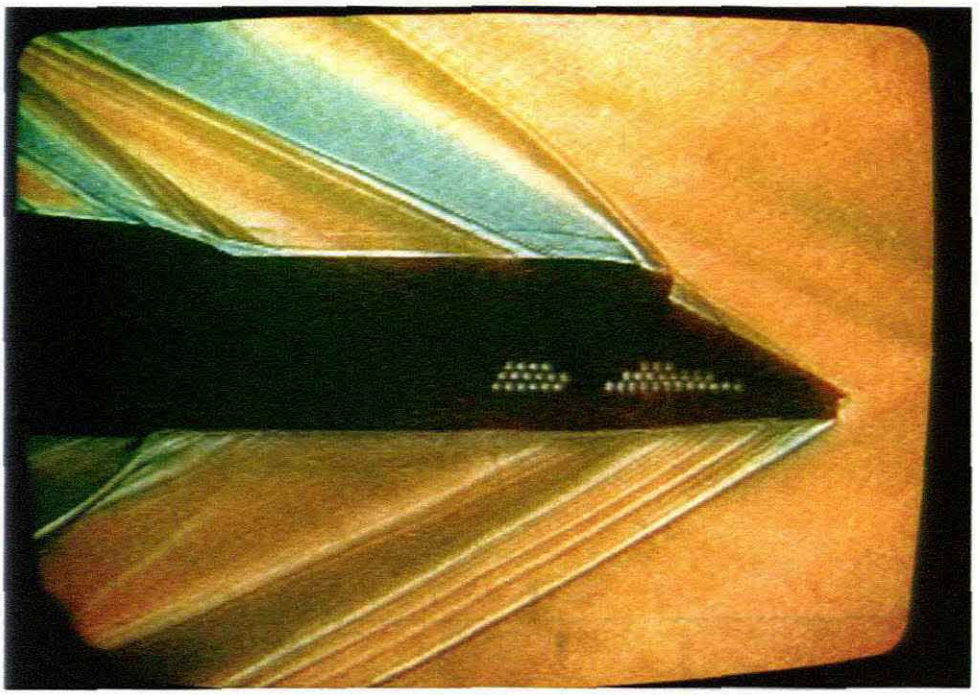

(a) Critical and Supercritical Flow

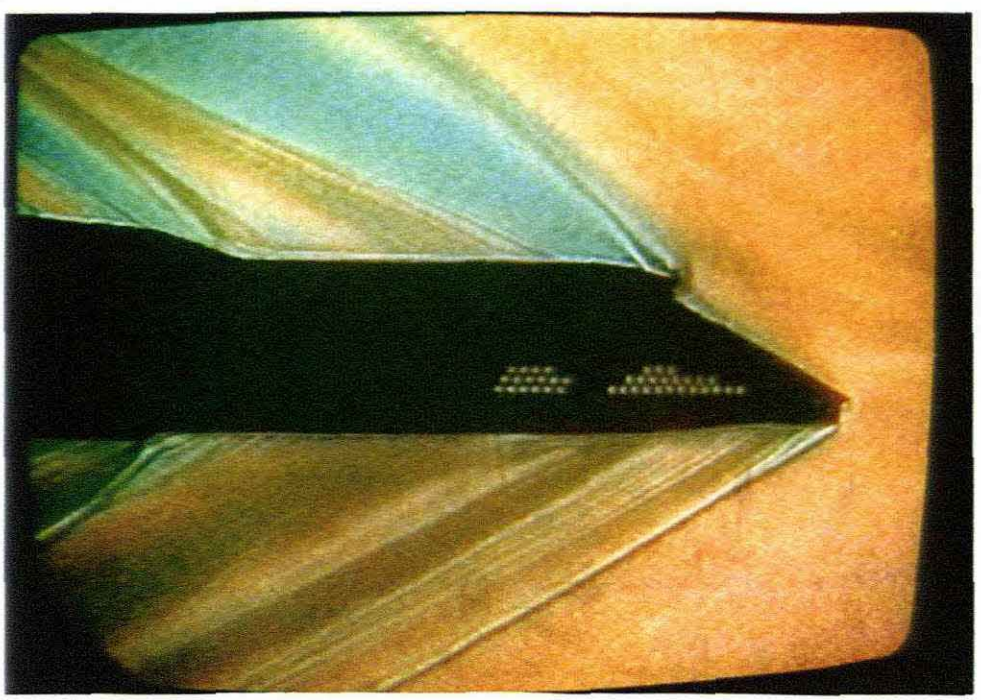

(b) Subcritical Flow

FIGURE 4.17 : External Flow Field Showing Shock Patterns for $M_\infty = 2,3$
(At the Shock on Lip Mach No.)

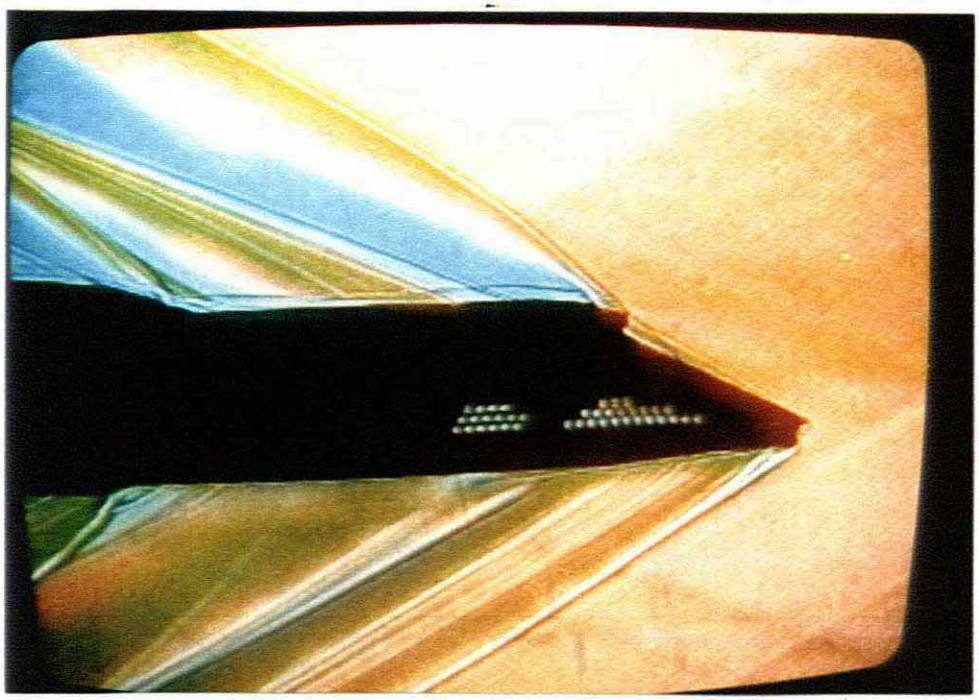

(a) Critical and Supercritical Flow

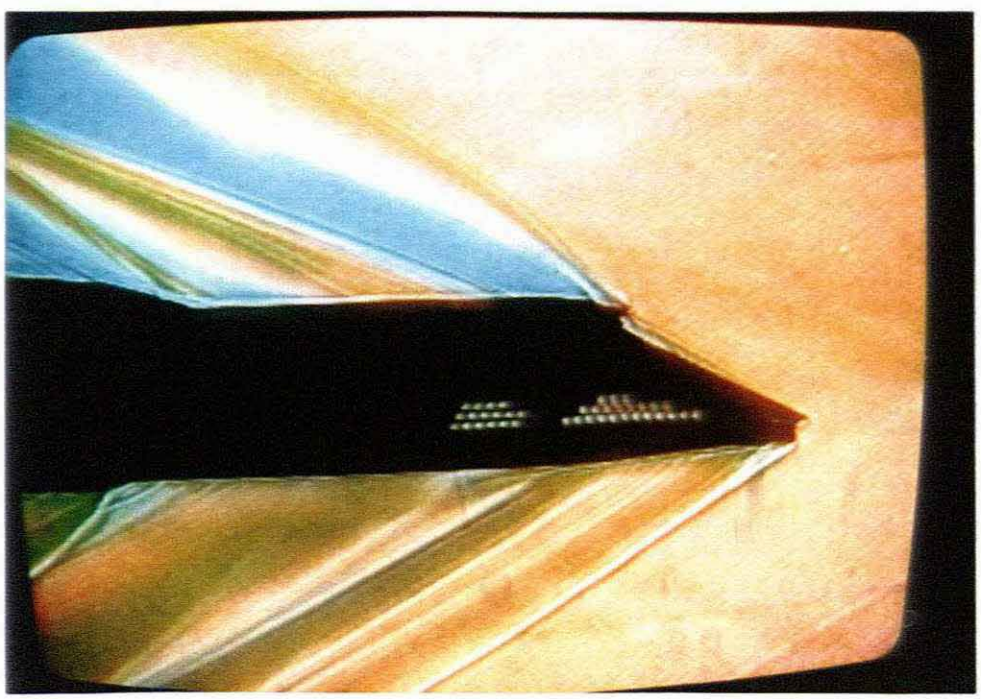

(b) Subcritical Flow

FIGURE 4.18 : External Flow Field Showing Shock Patterns for $M_\infty = 2,4$ (Above the Design Mach No.)

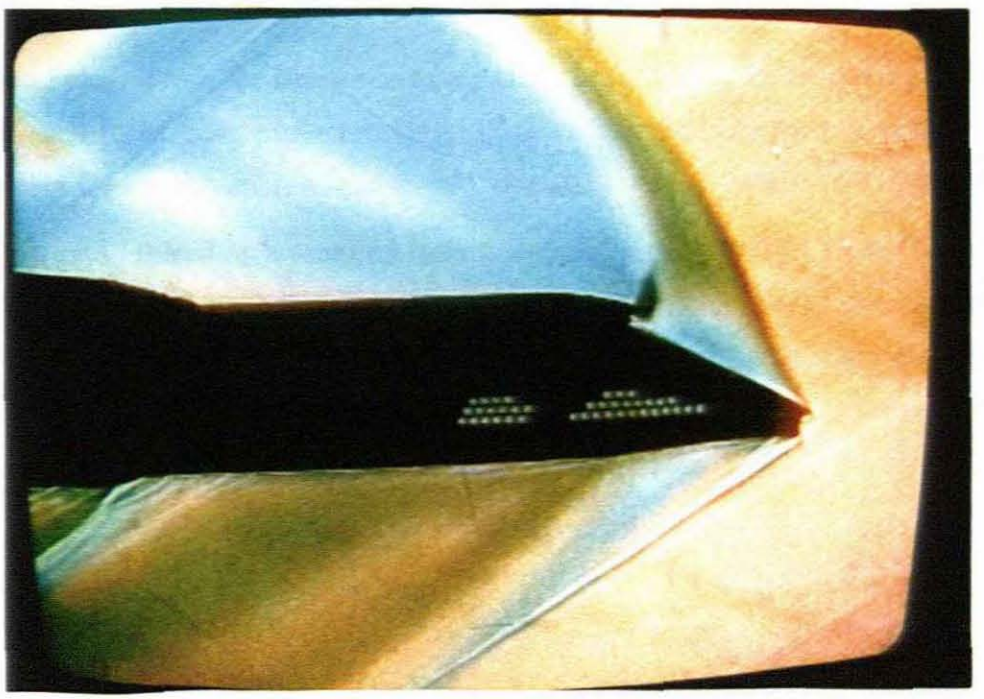

FIGURE 4.19 : External Flow Field Showing "Buzz" Condition

4.4.4 Bleed Flow

For theoretical drag predictions, as discussed in section 3.3.4 for bleed drag, a typical bleed flow ratio of 8 % was assumed. The full-scale porous model made provision for the low energy boundary layer air to be bled off at the throat section. The bleed air was accumulated in a plenum chamber below the throat section and dumped overboard through holes in the side plates to the test section of the tunnel. Stagnation pressures were recorded during testing at M = 2,0.

Bleed flow measurement is fully described in section 4.3.4. From the test results, for critical mode of operation, it was established that a value for the pressure ratio of $P_{OB} / P_S = \frac{86{,}60\ kPa}{41{,}94\ kPa} = 2{,}06$ was adequate to ensure choking of the flow through the bleed holes. From the isentropic relations for critical flow the air density and velocity through each bleed hole were calculated. Substituting the relevant information into the relationship for conservation-of-mass, $\dot{m}_c = \rho VA$, yielded a value of 0,074 kg/s for the bleed flow rate. Based on a captured mass flow ratio, $m_R = 0{,}78$ (Ref Table C.3) a value of 0,894 kg/s was established for the captured mass flow. The bleed flow ratio, as described in section 3.3.4, is expressed as a percentage of the mass flow entering the inlet. Based on these flow rates a bleed flow ratio of 8,3 % was established which correlates very well with the assumed value of 8 %, as used in theoretical drag calculations.

4.5 SUMMARY

Despite very difficult logistical problems the test program was successfully concluded with the help of the wind-tunnel personnel of the Aerotek Division of the CSIR. Great care was taken to ensure proper set up of the model, accurate calibration of equipment and application of scientific methods for capturing of data.

The main objective of the experimental phase was achieved where the necessary data was recorded from which drag coefficients, mass flow ratios and bleed flow rates could be determined. A bonus was the recording Schlieren material which could be used to visually study and thus analyse the external flow fields over the full operational range of the inlet.

CHAPTER 5

CONCLUSION AND RECOMMENDATIONS

A complex fluid-dynamic problem was solved satisfactorily by applying theoretical equations to a practical situation where a realistic two-dimensional external compression inlet was tested over its full operational range during an intensive wind-tunnel test program. Reasonably good correlation was achieved between experimental data and theoretical values at low subcritical mode of operation and the following conclusions can be made .

- a smaller mass flow range, typically 0,63 to 0,98, achieved during the test program indicates that the inlet can only be operated over a much smaller subcritical mode than that which was expected;

- the mass flow ratio or mode of operation has a significant effect on drag; eg. at M = 1,8; 2,0; 2,2; 2,3 and 2,4 the drag increases by 164%; 96%; 107%; 180% and 64% respectively with an associated reduction in mass flow rate;

- variation in Mach number, from below to above the design point (M = 1,8 to 2,4), caused a 50% increase in drag at maximum flow conditions;

- the steep slope of the curve for the experimental drag coefficient indicates that at subcritical mode of operation the increase in drag with a decrease in captured mass flow rate is much more severe than expected. This indicates a major drag penalty associated with spill.

It is finally concluded that by comparing the theoretical values with the experimental data, the primary objective has been achieved by providing realistic drag coefficient values, for the following mass flow ranges, over which theoretical equations can be used to calculate the drag of a two-dimensional external compression inlet :

- $m_R = 0,69$ to $0,65$ at $M = 1,8$;
- $m_R = 0,78$ to $0,75$ at $M = 2,0$;
- $m_R = 0,85$ to $0,79$ at $M = 2,2$;
- $m_R = 0,93$ to $0,88$ at $M = 2,3$;
- $m_R = 0,98$ to $0,97$ at $M = 2,4$.

The experimental procedure showed shortcomings in fine tuning the captured mass flow rate during subcritical mode of operation. It is recommended that for future tests the mass flow control device must be able to move forward in very small steps to ensure capturing of data over the full subcritical mode of operation.

This study opened up the field for further research where specific attention should be given to the influence that main components, such as the cowl lip, has on the aerodynamic drag characteristics of this type of inlet. It is finally recommended that further research should be carried out on an installed inlet and that drag coefficient values should be obtained for different angles of pitch and yaw.

REFERENCES

Anon. 1980. **Intakes for Pure Jet Engines.** Short Course Handouts, Cranfield Institute of Technology, UK.

Anon. 1981. **British Standard. Methods of Measurement of Fluid flows in closed conduits**. BS 1042: Section 1.1: 1981. British Standards Institution, London.

Backeberg, P.M. 1989. **Experimental Determination of Maximum Allowable Blockage for an Intake Model in the DAST High Speed Wind Tunnel**. Report DAST 89/37. CSIR, Pretoria.

Bendot, J.G., Heins Jr, A.E. & Piercy, T.G. 1984. **Ramjet Air Induction System Design for Tactical Missile Application**. AGARD Lecture Series No. 136, Ramjet and Ramrocket Propulsion Systems for Missiles.

Connors, J.F. & Lovell, J.C. 1957. **Investigation of Translating - Double-Cone Axisymmetric Inlets with Cowl Projected Areas 40 and 70 Percent of Maximum at Mach Numbers from 3,0 to 7,0**. NACA RM E57 CO6.

Gregoriou, G. 1985. **Introduction to Inlet Aerodynamics**. (Unpublished).

Hall, R.B. 1977. **Additive Drag of Two-dimensional Inlets**. Naval Weapons Centre China Lake, California.

Hattingh, H.V. 1977. Gasdinamika A. Klasnotas. Eerste Uitgawe. University of Stellenbosch.

Hawkins, J.E., Kirkland, F.P. & Turner, R.L. 1976. **Inlet Spillage Drag Tests and Numerical Flow-Field Analysis at Subsonic and Transonic Speeds of a ⅛-scale,**

Two-Dimensional, External-Compression, Variable-Geometry, Supersonic Inlet Configuration. National Aeronautics and Space Administration Washington, DC, USA.

Hoerner, S.F. 1965. **Fluid - Dynamic Drag**. New York City, USA.

Krieger, R.J. & Vukelich, S.R. 1986. **Tactical Missile Drag**. Progress in Astronautics and Aeronautics. Volume 1. American Institute of Aeronautics and Astronautics, New York.

Laruelle, G. 1987. **Air intakes for Supersonic Missiles: Design Criteria and Development**. ONERA, BP 7.2 F-92322, Chatillon Cedex, France.

Laruelle, G. 1988. **Missile Intakes**. Lecture Series 1988-04. Intake Aerodynamics, Von Karman Institute, Belgium.

Lee, C.C. & Boedicker. 1985. **Subsonic Diffusor Design and Performance for Advanced Fighter Aircraft**. AIAA-85-3073.

Leyland, D.C. 1988. **Intake Drag**. Lecture Series 1988-04. Intake Aerodynamics, Von Karman Institute, Belgium.

Leynaert, J. 1988. **Transport Aircraft Intake Design**. Lecture Series 1988-04. Intake Aerodynamics, Von Karman Institute, Belgium.

Oswatitsch, K. 1947. **The Efficiency of Shock Diffusers**. NACA TM 1140.

Pearce, Jr. R.B. 1959. **Supersonic Ramjet Diffuser Design**. Missile Division, North America Aviation, Downey, California.

Pope, A. & Goin, K.L. 1965. **High-speed Wind Tunnel Testing**. John Wiley and Sons, Inc. New York.

Ratner,G.C. 1995. *Calibration of an Internal Strain Gauge Balance.* Technical Report No.2. CSIR, Pretoria.

Ratner, G.C. 1995. 6 Compnent Strain Gauge Balance Calibration Matrix Calculation. Technical Report No. 5. CSIR, Pretoria.

Seddon, J. & Goldsmith, E.L. 1985. **Intake Aerodynamics**. AIAA Educational Series, Air Force Institute of Technology, Ohio, USA.

Seddon, J. 1988. **Introduction to Intake Aerodynamics**. Lecture Series: Intake Aerodynamics, Von Karman Institute, Belgium.

Stockenström, A. 1990. Supersonic Inlet: Phase Three Test Report. Somchem Report No. 03982-000000-725017.

Stockenström, A. 1991. Phase Four Supersonic Inlet Test. Somchem Report No. 03982-000000-725030.

Surber, L.E. 1975. **Effect of Forebody Shape and Shielding Techinique on 2-D Supersonic Inlet Performance**. AIAA-75-1183.

Surber, L.E. & Numbers, K.E. 1988. **Tactical Fighter Inlets**. Lecture Series 1988-04. Intake Aerodynamics, Von Karman Institute, Belgium.

Tindell, R.H. 1987. **Highly Compact Inlet Diffusor Technology**. AIAA-87-1747.

White, F.M. 1994. **Fluid Mechanics**. McGraw-Hill Inc., New York.

Zucrow, M.J. & Hoffman, J.D. 1976. **Gas Dynamics Volume 1**. John Wiley and Sons., New York.

APPENDIX
A

MASS FLOW CALCULATIONS AT DIFFERENT MACH NUMBERS

In calculating the aerodynamic drag of an inlet it is important to consider the different conditions under which the inlet is operating, eg. height above sea level and mass flow captured.

For the theoretical determination of the drag coefficient, as fully described in section 3.3 of Chapter 3, it is important to analyse the mass flow captured by the inlet at different flight Mach numbers.

In a very general application, a ground launch at sea level is considered, based on "Properties of the U.S. Standard Atmosphere" (Zucrow & Hoffman 1976:708) where :

Static pressure, $P = 101{,}33$ kPa;

Static temperature, $T = 288{,}15$ K;

and the thermodynamic constants for air are (Zucrow & Hoffman 1976:700):

Specific heat ratio, $\gamma = 1{,}4$;

Gas constant, $R = 287{,}06$ J/kg.K.

Referring to Table A.1 all the relevant information, of the full-scale porous model, can be found for conducting the following calculations based on the governing equations for steady one-dimensional flow of a perfect gas (Zucrow & Hoffman 1976:154-156):

$$\frac{P_0}{P} = \left(1 + \frac{\gamma - 1}{2} M^2\right)^{\frac{\gamma}{\gamma - 1}} \qquad (A.1)$$

$$\frac{T_0}{T} = \left(1 + \frac{\gamma - 1}{2} M^2\right) \qquad (A.2)$$

$$\rho = \frac{P}{RT} \qquad (A.3)$$

$$a = \sqrt{\gamma R T} \qquad (A.4)$$

$$V = M.a \qquad (A.5)$$

$$\dot{m} = \rho V A \qquad (A.6)$$

Where:

P_o	=	Stagnation pressure
P	=	Static pressure
T_o	=	Stagnation temperature
T	=	Static temperature
ρ	=	Density
$\dot{m}$	=	Mass flow
a	=	Speed of sound
V	=	Velocity
M	=	Mach number.

From the above information the data as shown in Table A.2 can be calculated.

For the purpose of exercise a Mach number of 2,0, which is just below the design Mach number of 2,2, is selected because it is a very common Mach number for vehicles in flight.

Mass flow values are calculated for (i) full flow at free stream conditions and (ii) flow captured

at throat section behind second oblique shock.

i) Full mass flow

Substituting the relevant information into:

eqn. A.1	yields a value of	P_o = 792,85 kPa;
eqn. A.2	yields a value of	T_o = 518,67 K;
eqn. A.3	yields a value of	ρ = 1,225 kg/m^3;
eqn. A.4	yields a value of	a = 340,30 m/s;
eqn. A.5	yields a value of	V = 680,60 m/s.

At free stream conditions the mass flow is based on the dimensions of the capture area of the inlet opening, i.e. height = 52,9 mm and width = 53,3 mm.

Substituting the relevant information into eqn. A.6 yields a value of $\dot{m}_\infty = 2{,}351\ kg/s$ for the full mass flow.

ii) Captured mass flow

The actual mass flow captured by the inlet is based on conditions behind the second oblique shock where the streamtube enters the throat section. The conditions behind the oblique shocks can be calculated from shock wave theory.

For a given free stream Mach number of 2,0 and a deflection angle, $\delta_1 = 9°$ for the first compression wedge, the shock wave angle $\epsilon_1 = 38{,}26\ °$ can be found from Table C.12 (Zucrow & Hoffman 1976:744).

From eqn 7.99 (Zucrow & Hoffman 1976:368) :

$$M' = M \sin \epsilon \qquad (A.7)$$

Where $M^{`}$ is the component of the Mach number normal to an oblique shock wave.

Substituting the relevant information into the above equation yields a value of $M^{`} = 1,24$. From Table C.11 (Zucrow & Hoffman 1976:737) the normal component of the Mach number after the shock and static pressure ratio over the shock can be read off as $M^{`}_1 = 0,8183$ and $P_2/P_1 = 1,6272$ respectively.

The Mach number after the first oblique shock can now be calculated from eqn. 7.100 (Zucrow & Hoffman 1976:368) where :

$$M = \frac{M^{`}}{Sin\ (\epsilon - \delta)} \qquad (A.8)$$

Substituting the relevant information into the above equation yields a value for $M_1 = 1,67$.

From the static pressure ratio of $P_1/P_\infty = 1,6272$ the value for $P_1 = 101,33 \times 1,6272 = 164,88$ kPa can be found.

From the governing equations for one dimensional flow the stagnation pressure behind the first oblique shock yields a value of $P_{o1} = 777,92$ kPa.

Since for a perfect gas, the stagnation pressure remains constant across shock waves (Zucrow & Hoffman 1976:336), the static temperature behind the first oblique shock wave can be calculated. Substituting values of $T_{o1} = 518,67$ K and $M_1 = 1,674$ into eqn. A.2 yields a value of $T_1 = 332,95$K.

From equations A.3, A.4 and A.5 the values for $\rho = 1,725$ kg/m^3; $a = 365,80$ m/s and $V = 610,88$ are calculated respectively.

In a similar manner the conditions behind the second oblique shock can be calculated. The results of the flow analysis for different flow areas, i.e. free stream, after first oblique shock, after second oblique shock and after normal shock are depicted in Table A.2.

The actual mass flow captured by the inlet is a function of conditions behind the second oblique shock and the throat area, A_T. Substituting the values of ρ_2 = 2,281 kg/m^3, V_2 = 539,007 m/s and A_T = (31,7 x 53,3) 10^{-6} m^2 into eqn. A.6 yields a value of $\dot{m}_c$ = 2,08 *kg/s* .

Results of flow analyses done at Mach numbers of 1,8, 2,2, 2,3 and 2,4 are depicted in Tables A.3, A.4, A.5 and A.6 respectively.

TABLE A.1: Critical Dimensions of Full-Scale Porous Model

Number of wedges	2
Wedge Angles δ_1 δ_2	9,0° 8,0°
Height of throat Width of throat	31,7 mm 53,3 mm
Height of capture area: Width of capture area:	52,9 mm 53,3 mm
Lip effective external angles η_o η_1	19,3° 5,6°
Lip expansion angle δ	13,7°
Wetted surface of lip:	
(i) Internal: width length	53,3 mm 46,7 mm
(ii) External: Width Length, ℓ_1 ℓ_2	56,4 mm 14,9 mm 32,8 mm
Bleed duct exit area for choked flow at M_∞ = 2,4 Aex	268 x 10^{-6} m^2
Diverter width Diverter height Diverter wedge angle	56,4 mm 14,4 mm 37,5 °
Inlet Frontal dimensions:	
(i) Total Height	61,02 mm
(ii) External Width	56,40 mm

TABLE A.2: One Dimensional Flow Analysis at Mach Number = 2,0 for Atmospheric Conditions at Sea Level

FREE STREAM CONDITIONS	
Static pressure	P_∞ = 101,33 kPa
Stagnation pressure	$P_{o\infty}$ = 792,85 kPa
Dynamic pressure	q_∞ = 283,72 kPa
Reynolds number	R_e = 46 x 10^6/m
Static temperature	T_∞ = 288,15 K
Stagnation temperature	$T_{o\infty}$ = 518,67 K
Density	ρ = 1,225 kg/m^3
Speed of sound	a = 340,30 m/s
Velocity	V = 680,60 m/s
Full mass flow	$\dot{m}_\infty$ = 2,351 kg/s
CONDITIONS AFTER FIRST OBLIQUE SHOCK	
Wedge angle	δ_1 = 9°
Shock wave angle	ϵ_1 = 38,26°
Mach number	M_1 = 1,67
Static pressure	P_1 = 164,88 kPa
Stagnation pressure	P_{o1} = 777,93 kPa
Static temperature	T_1 = 332,95 K
Stagnation temperature	T_{o1} = 518,67 K
Density	ρ = 1,725 kg/m^3
Speed of sound	a = 365,80 m/s
Velocity	V = 610,88 m/s
CONDITIONS AFTER SECOND OBLIQUE SHOCK	
Wedge angle	δ_2 = 8°
Shock wave angle	ϵ_2 = 45,5°
Mach number	M_2 = 1,39
Static pressure	P_2 = 244,91 kPa
Stagnation pressure	P_{o2} = 768,49 kPa
Static temperature	T_2 = 374,11 K
Stagnation temperature	T_{o2} = 518,67 K
Density	ρ = 2,281 kg/m^3
Speed of sound	a = 387,78 m/s
Velocity	V = 539,01 m/s
Mass flow captured	$\dot{m}_c$ = 2,08 kg/s
CONDITIONS AFTER NORMAL SHOCK	
Mach number	M_3 = 0,74
Static pressure	P_3 = 511,23 kPa
Stagnation pressure	P_{o3} = 735,51 kPa
Static temperature	T_3 = 467,47 K
Stagnation temperature	T_{o3} = 518,67 K
Density	ρ = 3,81 kg/m^3
Speed of sound	a = 433,44 m/s
Velocity	V = 320,74 m/s
Mass flow ratio	m_R = 0,89

TABLE A.3: One Dimensional Flow Analysis at Mach Number = 1,8 for Atmospheric Conditions at Sea Level

FREE STREAM CONDITIONS	
Static pressure	P_∞ = 101,33 kPa
Stagnation pressure	$P_{o\infty}$ = 582,22 kPa
Dynamic pressure	q_∞ = 229,82 kPa
Reynolds number	R_e = 42 x 10^6/m
Static temperature	T_∞ = 288,15 K
Stagnation temperature	$T_{o\infty}$ = 474,87 K
Density	ρ = 1,225 kg/m^3
Speed of sound	a = 340,30 m/s
Velocity	V = 612,54 m/s
Full mass flow	$\dot{m}_\infty = 2,12\ kg/s$
CONDITIONS AFTER FIRST OBLIQUE SHOCK	
Wedge angle	δ_1 = 9°
Shock wave angle	ϵ_1 = 42,87°
Mach number	M_1 = 1,49
Static pressure	P_1 = 159,07 kPa
Stagnation pressure	P_{o1} = 575,56 kPa
Static temperature	T_1 = 328,85 K
Stagnation temperature	T_{o1} = 474,87 K
Density	ρ = 1,685 kg/m^3
Speed of sound	a = 363,54 m/s
Velocity	V = 541,67 m/s
CONDITIONS AFTER SECOND OBLIQUE SHOCK	
Wedge angle	δ_2 = 8°
Shock wave angle	ϵ_2 = 53,11°
Mach number	M_2 = 1,20
Static pressure	P_2 = 236,28 kPa
Stagnation pressure	P_{o2} = 572,97 kPa
Static temperature	T_2 = 368,69 K
Stagnation temperature	T_{o2} = 474,87 K
Density	ρ = 2,233 kg/m^3
Speed of sound	a = 384,93 m/s
Velocity	V = 461,91 m/s
Mass flow captured	$\dot{m}_c = 1,74\ kg/s$
CONDITIONS AFTER NORMAL SHOCK	
Mach number	M_3 = 0,84
Static pressure	P_3 = 357,56 kPa
Stagnation pressure	P_{o3} = 567,56 kPa
Static temperature	T_3 = 416,14 K
Stagnation temperature	T_{o3} = 474,87 K
Density	ρ = 2,993 kg/m^3
Speed of sound	a = 408,95 m/s
Velocity	V = 343,52 m/s
Mass flow ratio	m_R = 0,82

TABLE A.4: One Dimensional Flow Analysis at Mach Number = 2,2 for Atmospheric Conditions at Sea Level

FREE STREAM CONDITIONS	
Static pressure	P_∞ = 101,33 kPa
Stagnation pressure	$P_{o\infty}$ = 1083,49 kPa
Dynamic pressure	q_∞ = 343,31 kPa
Reynolds number	R_e = 51 x 10^6/m
Static temperature	T_∞ = 288,15 K
Stagnation temperature	$T_{o\infty}$ = 567,08 K
Density	ρ = 1,225 kg/m^3
Speed of sound	a = 340,30 m/s
Velocity	V = 748,66 m/s
Full mass flow	$\dot{m}_\infty$ = 2,59 kg/s
CONDITIONS AFTER FIRST OBLIQUE SHOCK	
Wedge angle	δ_1 = 9°
Shock wave angle	ϵ_1 = 34,81°
Mach number	M_1 = 1,85
Static pressure	P_1 = 170,79 kPa
Stagnation pressure	P_{o1} = 1059,54 kPa
Static temperature	T_1 = 336,65 K
Stagnation temperature	T_{o1} = 567,08 K
Density	ρ = 1,767 kg/m^3
Speed of sound	a = 367,82 m/s
Velocity	V = 680,47 m/s
CONDITIONS AFTER SECOND OBLIQUE SHOCK	
Wedge angle	δ_2 = 8°
Shock wave angle	ϵ_2 = 40,42°
Mach number	M_2 = 1,57
Static pressure	P_2 = 258,46 kPa
Stagnation pressure	P_{o2} = 1050,95 kPa
Static temperature	T_2 = 379,83 K
Stagnation temperature	T_{o2} = 567,08 K
Density	ρ = 2,370 kg/m^3
Speed of sound	a = 390,70 m/s
Velocity	V = 613,40 m/s
Mass flow captured	$\dot{m}_c$ = 2,46 kg/s
CONDITIONS AFTER NORMAL SHOCK	
Mach number	M_3 = 0,68
Static pressure	P_3 = 700,17 kPa
Stagnation pressure	P_{o3} = 954,22 kPa
Static temperature	T_3 = 519,08 K
Stagnation temperature	T_{o3} = 567,08 K
Density	ρ = 4,699 kg/m^3
Speed of sound	a = 456,74 m/s
Velocity	V = 310,58 m/s
Mass flow ratio	m_R = 0,95

TABLE A.5: One Dimensional Flow Analysis at Mach Number = 2,3 for Atmospheric Conditions at Sea Level

FREE STREAM CONDITIONS	
Static pressure	P_∞ = 101,33 kPa
Stagnation pressure	$P_{o\infty}$ = 1267,06 kPa
Dynamic pressure	q_∞ = 375,22 kPa
Reynolds number	R_e = 53 x 10^6/m
Static temperature	T_∞ = 288,15 K
Stagnation temperature	$T_{o\infty}$ = 593,01 K
Density	ρ = 1,225 kg/m^3
Speed of sound	a = 340,30 m/s
Velocity	V = 782,69 m/s
Full mass flow	$\dot{m}_\infty$ = 2,70 kg/s
CONDITIONS AFTER FIRST OBLIQUE SHOCK	
Wedge angle	δ_1 = 9°
Shock wave angle	ϵ_1 = 33,38°
Mach number	M_1 = 1,94
Static pressure	P_1 = 173,78 kPa
Stagnation pressure	P_{o1} = 1238,78 kPa
Static temperature	T_1 = 338,34 K
Stagnation temperature	T_{o1} = 593,01 K
Density	ρ = 1,789 kg/m^3
Speed of sound	a = 368,75 m/s
Velocity	V = 715,38 m/s
CONDITIONS AFTER SECOND OBLIQUE SHOCK	
Wedge angle	δ_2 = 8°
Shock wave angle	ϵ_2 = 38,41°
Mach number	M_2 = 1,65
Static pressure	P_2 = 267,86 kPa
Stagnation pressure	P_{o2} = 1226,49 kPa
Static temperature	T_2 = 383,95 K
Stagnation temperature	T_{o2} = 593,01 K
Density	ρ = 2,430 kg/m^3
Speed of sound	a = 392,81 m/s
Velocity	V = 648,14 m/s
Mass flow captured	$\dot{m}_c$ = 2,66 kg/s
CONDITIONS AFTER NORMAL SHOCK	
Mach number	M_3 = 0,65
Static pressure	P_3 = 806,15 kPa
Stagnation pressure	P_{o3} = 1070,83 kPa
Static temperature	T_3 = 546,80 K
Stagnation temperature	T_{o3} = 593,01 K
Density	ρ = 5,136 kg/m^3
Speed of sound	a = 468,78 m/s
Velocity	V = 304,71 m/s
Mass flow ratio	m_R = 0,99

TABLE A.6: One Dimensional Flow Analysis at Mach Number = 2,4 for Atmospheric Conditions at Sea Level

FREE STREAM CONDITIONS	
Static pressure	P_∞ = 101,33 kPa
Stagnation pressure	$P_{o\infty}$ = 1481,45 kPa
Dynamic pressure	q_∞ = 408,56 kPa
Reynolds number	R_e = 56 x 10^6/m
Static temperature	T_∞ = 288,15 K
Stagnation temperature	$T_{o\infty}$ = 620,10 K
Density	ρ = 1,225 kg/m^3
Speed of sound	a = 340,30 m/s
Velocity	V = 816,72 m/s
Full mass flow	$\dot{m}_\infty$ = 2,82 kg/s
CONDITIONS AFTER FIRST OBLIQUE SHOCK	
Wedge angle	δ_1 = 9°
Shock wave angle	ϵ_1 = 32,09°
Mach number	M_1 = 2,03
Static pressure	P_1 = 176,80 kPa
Stagnation pressure	P_{o1} = 1449,51 kPa
Static temperature	T_1 = 339,93 K
Stagnation temperature	T_{o1} = 620,10 K
Density	ρ = 1,812 kg/m^3
Speed of sound	a = 369,61 m/s
Velocity	V = 750,31 m/s
CONDITIONS AFTER SECOND OBLIQUE SHOCK	
Wedge angle	δ_2 = 8°
Shock wave angle	ϵ_2 = 36,65°
Mach number	M_2 = 1,76
Static pressure	P_2 = 267,55 kPa
Stagnation pressure	P_{o2} = 1446,31 kPa
Static temperature	T_2 = 382,89 K
Stagnation temperature	T_{o2} = 620,10 K
Density	ρ = 2,434 kg/m^3
Speed of sound	a = 392,27 m/s
Velocity	V = 690,40 m/s
Mass flow captured	$\dot{m}_c$ = 2,84 kg/s (1)
CONDITIONS AFTER NORMAL SHOCK	
Mach number	M_3 = 0,63
Static pressure	P_3 = 922,31 kPa
Stagnation pressure	P_{o3} = 1205,00 kPa
Static temperature	T_3 = 574,50 K
Stagnation temperature	T_{o3} = 620,10 K
Density	ρ = 5,593 kg/m^3
Speed of sound	a = 480,50 m/s
Velocity	V = 302,72 m/s
Mass flow ratio	m_R = 1,0

APPENDIX
B

MAXIMUM MODEL SIZE

The maximum model size had to be calculated to ensure proper starting of the tunnel at test Mach numbers of M = 2,0 to M = 2,4.

As can be seen from Figure 1:27 (Pope & Goin 1965:38) the biggest problem occurs at the lower Mach numbers where a smaller area ratio is required than at a higher Mach numbers. Therefore for a test Mach number of M = 2,0 the size of the model can be calculated from the following dimensionless ratios, read-off from Figure 1:27 (Pope & Goin 1965:38) :

i) $\frac{dm}{\sqrt{A}} = 0{,}47$ *for a theoretical case*

ii) $\frac{dm}{\sqrt{A}} = 0{,}355$ *for an actual case.*

Where :

dm = Maximum model diameter

A = Physical test section cross-sectional area less the product of boundary layer displacement thickness and test section perimeter.

Taking the dimensions of full-scale porous model, the frontal area including diverter can be calculated as follows :

$$A = (61{,}02 + 14{,}4)\ 56{,}4 \times 10^{-6}\ m^2$$
$$= 4253{,}69 \times 10^{-6}\ m^2$$

Where :

Model dimensions = 61,02 mm x 56,4 mm x 564 mm long; and

Diverter dimensions = 14,4 mm x 56,4 mm x 564 mm long.

An equivalent diameter can be calculated as follows :

$$A = \frac{\pi\ dm^2}{4}$$

$$dm = \sqrt{\frac{4\ x\ 4253{,}69\ x\ 10^{-6}}{\pi}}$$

$$= 73{,}593\ x\ 10^{-3}\ m$$

The size of the tunnel can now be calculated for a certain start based on :

i) a theoretical case;

ii) an actual case.

i) For *a theoretical case :*

$$\frac{dm}{\sqrt{A}} = 0{,}47$$

$$A = \left(\frac{dm}{0{,}47}\right)^2$$

$$= \left(\frac{73{,}593\ x\ 10^{-3}}{0{,}47}\right)^2\ m^2$$

$$A = 24517{,}563\ x\ 10^{-6}\ m^2.$$

Assuming that the tunnel has a square test section the following dimensions are obtained :

156,580 mm x 156,580 mm.

ii) *For an actual case :*

$$\frac{dm}{\sqrt{A}} = 0{,}355$$

$$= \left(\frac{73{,}593 \times 10^{-3}}{0{,}355} \right)^2 m^2$$

$$= 42975{,}042 \times 10^{-6}\ m^2.$$

Assuming that the tunnel has a square test section the following dimensions are obtained :

207,304 mm x 207,304 mm.

The High Speed Wind-tunnel (HSWT) of the CSIR in Pretoria where these tests were conducted has a test section with dimensions of 450 mm x 450 mm, which is far greater than the required dimensions mentioned above.

It was further proved by Backeberg (1989) that this tunnel was successfully started at M = 1,8 and M = 3,0 with a model, having dimensions of 127 mm x 127 mm x 1320 mm long, installed in the test section.

It is therefore clear that the test model under consideration, "Full-scale Porous", has dimensions which did not pose any blockage problems to the starting of this tunnel.

References

Backeberg, P.M. 1989. **Experimental Determination of Maximum Allowable Blockage for an Intake Model in the DAST High Speed Wind-tunnel**. Report DAST 89/37. CSIR, Pretoria.

Pope, A. & Goin, K.L. 1965. **High Speed Wind-tunnel Testing**. John Wiley and Sons, Inc. New York.

APPENDIX
C

AERODYNAMIC DRAG DATA FOR WIND-TUNNEL TESTS

TABLE C.1 : Nomenclature

1. Total Drag Force	D_t (N)
2. Dynamic Pressure	q_∞ (kPa)
3. Mach No.	M_∞
4. Full Mass Flow	$\dot{m}_\infty$
5. Captured Mass Flow	$\dot{m}_c$
6. Stagnation Temperature	T_0 (K)
7. Stagnation Pressure Bleed Chamber	P_{OB} (kPa)
8. Bleed Mass Flow Rate	m_B (%)
9. Reynolds Number	Re
10. Ambient Temperature	T_{amb} (K)
11. Atmospheric Pressure	P_{atm} (kPa)
12. Test Section Static Pressure	P_S (kPa)
13. Mass Flow Ratio	$m_R = \dot{m}_c / \dot{m}_\infty$
14. Total Drag Coefficient	$C_{dt} = \dfrac{D_t}{q_\infty \times 4253{,}69 \times 10^{-6}}$

Data were captured using the data recording system of the Aerotek Division of the CSIR in Pretoria. Tests were carried out according to the logging system mentioned in Table C.2.

TABLE C.2 Log-sheet for Recording Test Data

Blow No.	Mach No.	Stag. Press. (psi)	Atmos. Press. (mmHg)	File name	Inlet Configuration	Pitch ∝	Yaw β	Date
5241	2,2	25,0	648,1	MAT-001	Porous Throat	0	0	6/11/96
5242	2,0	42,5	647,7	MAT-002	"	"	"	"
5243	2,0	"	647,3	MAT-003	"	"	"	"
5244	2,0	"	652,1	MAT-004	"	"	"	11/11/96
5245	2,0	"	652,1	MAT-005	"	"	"	"
5250	2,0	"	648,3	MAT-006	"	"	"	19/11/96
5251	2,0	"	649,7	MAT-007	"	"	"	"
5252	2,0	"	649,5	MAT-008	"	"	"	"
5253	2,0	"	649,5	MAT-009	"	"	"	20/11/96
5254	2,0	"	648,9	MAT-010	"	"	"	"
5255	1,8	33,8	648,5	MAT-011	"	"	"	"
5256	2,2	54,4	648,3	MAT-012	"	"	"	"
5257	2,4	68,5	647,9	MAT-013	"	"	"	"
5258	2,3	60,4	647,9	MAT-014	"	"	"	"
5259	2,3	60,4	649,9	MAT-015	"	"	"	"
5260	2,3	60,4	649,2	MAT-016	"	"	"	21/11/96
5261	2,0	42,5	649,2	MAT-017	"	"	"	"

The recorded test results were analysed and reduced to the data points given for each test Mach number in the table below.

TABLE C.3: Corrected Test Data for various Mach Numbers

Test Mach Number = 1,8					
Axial Force Measured	**Stream Thrust**	**Net Drag**	**Drag Coeff.**	m_R	P_{Rcor}
N	**N**	**N**			**%**
-119	-321	115	0,22	0,70	71
-129	-384	168	0,31	0,69	79
-134	-430	209	0,39	0,67	85
-123	-466	256	0,48	0,65	91
-103	-501	311	0,58	0,63	97

Re = 42,01 x 10^6/m

Tunnel stagnation pressure = 320,34 kPa (abs)

Test section dynamic pressure = 126,50 kPa

Axial force due to chamber pressure = 87 N

P_{Rcor} Stagnation pressure recovery corrected for subsonic diffusor before abrupt expansion into duct of inlet rig (Stockenström 1991).

Net Drag = (Axial force measured - Stream thrust) - (Force due to chamber pressure)

Negative sign denotes forces acting in upstream direction.

Test Mach Number = 2,0					
Axial Force Measured	**Stream Thrust**	**Net Drag**	**Drag Coeff.**	m_R	P_{Rcor}
N	**N**	**N**			**%**
-139	-369	134	0,23	0.81	67
-212	-477	169	0,29	0.79	80
-218	-563	249	0,43	0,78	91
-201	-583	286	0,49	0,77	94
-178	-537	263	0,45	0,75	87
Re = 45,99 x 10^6/m					
Tunnel stagnation pressure = 380,33 kPa (abs)					
Test section dynamic pressure = 136,00 kPa					
Axial force due to chamber pressure = 96 N					
Bleed rate = 8 %					

Test Mach Number = 2,2					
Axial Force Measured	**Stream Thrust**	**Net Drag**	**Drag Coeff.**	m_R	P_{Rcor}
N	**N**	**N**			**%**
-100	-358	176	0,28	0,86	57
-101	-453	270	0,43	0,85	66
-103	-520	335	0,54	0,83	72
-91	-532	359	0,58	0,81	73
-90	-536	364	0,58	0,79	73
Re = 51,04 x 10^6/m					
Tunnel stagnation pressure = 462,37 kPa (abs)					
Test section dynamic pressure = 146,50 kPa					
Axial force due to chamber pressure = 82 N					

Test Mach Number = 2,3					
Axial Force Measured	**Stream Thrust**	**Net Drag**	**Drag Coeff.**	m_R	P_{Rcor}
N	**N**	**N**			**%**
-91	-365	196	0,31	0,93	55
-92	-465	295	0,47	0,89	63
-101	-556	377	0,59	0,88	70
-102	-693	513	0,81	0,87	83
-100	-731	553	0,87	0,85	87
Re = 52,97 x 10^6/m					
Tunnel stagnation pressure = 503,74 kPa (abs)					
Test section dynamic pressure = 149,00 kPa					
Axial force due to chamber pressure = 78 N					

Test Mach Number = 2,4					
Axial Force Measured	**Stream Thrust**	**Net Drag**	**Drag Coeff.**	m_R	P_{Rcor}
N	**N**	**N**			**%**
-59	-350	214	0,33	0,98	50
-54	-442	311	0,47	0,97	56
-62	-495	356	0,54	0,96	60
-61	-500	362	0,55	0,95	61
-59	-488	352	0,54	0,93	60
Re = 55,99 x 10^6/m					
Tunnel stagnation pressure = 559,59 kPa (abs)					
Test section dynamic pressure = 154,30 kPa					
Axial force due to chamber pressure = 77 N					

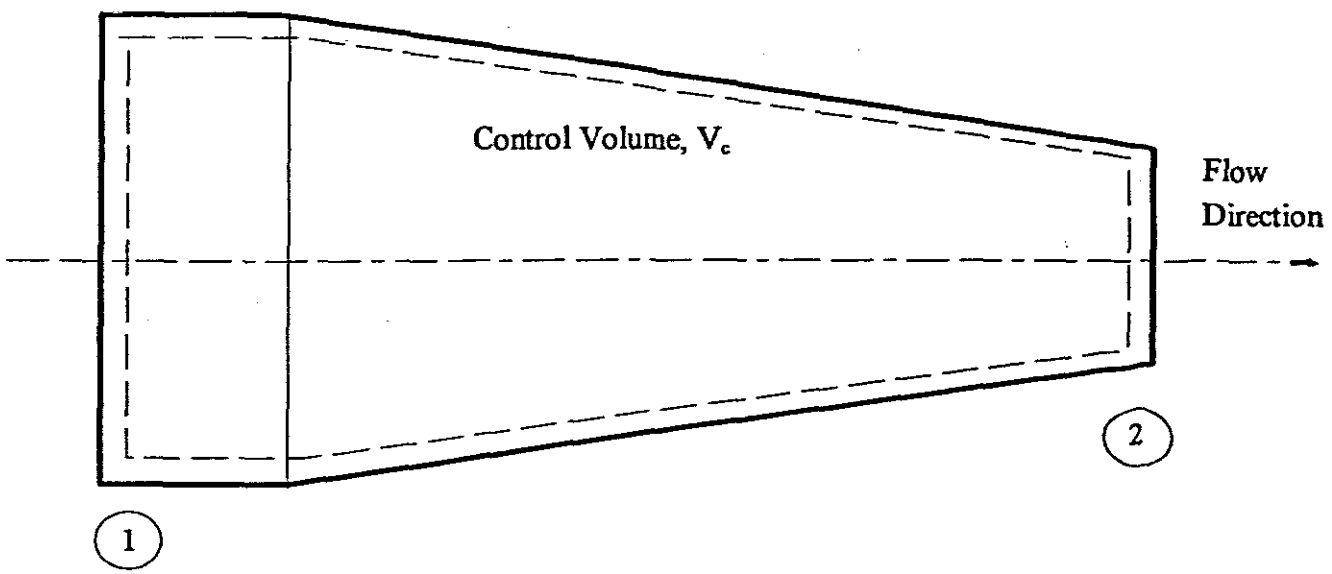

Internal Duct, running through balance, and connecting subsonic diffuser to inlet rig

Figure C.1 : Control Volume for Stream Thrust Calculations

Reference

Stockenström, A. 1991. **Phase Four Supersonic Inlet Test**. Somchem Report No. 03982-000000-725030.